UNIVERSITÉ DE STRASBOURG

Doctoral Thesis

Exploration and detection of ultra-traces of explosives by chip calorimetry

Author:
David DOBLAS JIMÉNEZ

Supervisors:
Dr. D. SPITZER
Dr. D.A. IVANOV

A thesis submitted in partial fulfilment of the requirements for the degree of Doctor of Philosophy

in the

École Doctorale de Physique
et Chimie-Physique

June 10^{th}, 2015

UNIVERSITÉ DE STRASBOURG

UNIVERSITÉ DE STRASBOURG

ÉCOLE DOCTORALE pcp Physique et Chimie-Physique

École Doctorale de Physique et Chimie-Physique

THÈSE présentée par:

David DOBLAS JIMÉNEZ

soutenue le: 10 Juin 2015

pour obtenir le grade de: Docteur de l'université de Strasbourg

Discipline / Spécialité: Chimie-Physique

Exploration and detection of ultra-traces of explosives by chip calorimetry

THÈSE dirigée par:

M. SPITZER, Denis	Docteur, ISL
M. IVANOV, Dimitri	Docteur, IS2M

RAPPORTEURS:

M. POPESCU, Crisan	Professeur, DWI – RWTH
M. SCHICK, Christoph	Professeur, Universität Rostock

JURY:

M. LALLAM, Abdelaziz	Docteur, UHA
M. DILHAN, Denis	Ingenieur, CNES Toulouse

Declaration of Authorship

I, David Doblas Jiménez, declare that this thesis titled, *Exploration and detection of ultra-traces of explosives by chip calorimetry* and the work presented in it are my own. I confirm that:

- This work was done wholly or mainly while in candidature for a research degree at this University.
- Where any part of this thesis has previously been submitted for a degree or any other qualification at this University or any other institution, this has been clearly stated.
- Where I have consulted the published work of others, this is always clearly attributed.
- Where I have quoted from the work of others, the source is always given. With the exception of such quotations, this thesis is entirely my own work.
- I have acknowledged all main sources of help.
- Where the thesis is based on work done by myself jointly with others, I have made clear exactly what was done by others and what I have contributed myself.

Signed: _____

Date: _____

Acknowledgements

Most cordially I want to thank my supervisors Dr. Dimitri A. Ivanov and Dr. Denis Spitzer for their encouragement, guidance and support throughout my whole PhD project. I am very grateful to them for sharing their scientific knowledge, for their patience with my questions and for giving me freedom in my research. It was really a great chance and always a pleasure for me to work with them. Thank you both of you for being good friends and mentors.

I am especially grateful to my group colleagues at IS2M, Jaime J. Hernández, Martin Rosenthal and Yaroslav Odarchenko, which were extraordinarily helpful for me during my PhD. Also to my office mates Wajdi Heni and Laura P. Chía.

Special thanks to my group colleagues at ISL, in particular, Laurent Schlur (thanks for translating the final resumé into French), Karine Bonnot, Marc Comet, Vincent Pichot, Fabien Schnell, Dominique Hassler, Michael Schäfer and Pierre Gibot. I will also thank the other Post-docs and PhD students especially, Nelly, Benedikt, Arnaud, Axel, Florent and Quentin.

Also to my colleagues at the Lomonosov Moscow State University, A. P. Melnikov, K. L. Gerasimov, A. A. Rychkov, A. I. Rodygin and A. Piryazev for the exhausting times shared at the ESRF during the experiments.

In addition I want to thank Dr. D. Chernyshov from the powder diffraction beam line BM01A for his help with the fitting of the experimental data as well as Dr. C. Riekel, Dr. M. Burghammer and Dr. E. Di Cola from the micro/nano-focus beam line ID13 at the ESRF for providing measuring time and scientific support.

Apart from the mentioned before, I would like to thank my family and especially to María for her permanent support throughout all these years both emotionally and in the daily life. You are all part of this thesis.

I would also like to thank the members of the jury for reading this manuscript. Finally I would like to acknowledge financial support from the Airbus Group in the form of a CNRS contract.

Extended Abstract

Being able to sense the minuscule amounts of energetic materials is very important in the context of continuing fight against terrorism. Apart from the classical methods of detection, which are specific to the chemical structure, it is also tempting to use the high enthalpy of the decomposition process for their detection by means of thermal analysis although this kind of analysis is not trivial. For doing this, classical techniques such as Differential Scanning Calorimetry requires using sealed crucibles with the difficulty of working under uncontrollable pressure during the measurements and managing relatively important quantities of such materials (typically larger than 100 micrograms). However, the sensitivity of the conventional techniques would be still insufficient to sense energetic materials particles in the nanogram range. By contrast, the recently developed technique of chip calorimetry is perfectly suited for characterizing small amounts of samples [1, 2] and is therefore fully adequate with the purposes of detection.

The first notion of chip calorimetry was introduced by L.H. Allen et al. in the beginning of 90´s [1]. He was also the first one to perform thermal analysis on thin supported films and to later extend this technique to other sample geometries such as micron-sized particles and individual polymer single crystals. Taking advantage of the development of the semiconductors industry, MEMS-based calorimetric sensors capable of performing quantitative thermoanalytical measurements on extremely small samples, such as nanograms or picograms. The heating and cooling rates employed are much higher than in the classical DSC: in this case, they are comprised between 10^2 and 10^6 K/s [2–4]. As a result, the measurements performed with nanocalorimetry are extremely fast (i.e., on the order of a few milliseconds).

In one of the laboratories (IS2M) in which I am doing my PhD, the research group directed by Dimitri Ivanov with the help of russian engineers built an electronic interface for a nanocalorimeter. Using this device one can

safely measure nanogram-sized samples at extremely high heating rates (up to 10^6 K/s). Although L.H. Allen and coworkers fabricated the nanocalorimetric sensors themselves, a promising perspective consists in the use of commercial semiconductor-based sensors initially developed for the gas thermal conductivity measurements. The Nanocalorimeter uses commercial gas sensors based on thin-film SixNy membranes with dimensions ranging from 30×30 to 250×250 μm^2 that contain integrated resistive heating elements and thermocouple hot junctions located some 50-100 µm away from the heater strips [5]. The nanocalorimeter sensors can either be mounted on a conventional transistor housing TO-5 base or on a planar ceramic connector, which can be used, as an example, for in situ combination of calormetric measurements with X-ray diffraction in transmission [6] among other techniques.

The other laboratory involved in my PhD (NS3E–ISL) offers an integrated approach starting from the synthesis of new energetic materials including their evaluation and application to specific security and defense requirements. The first nanocalorimetry results [7] showed that this accessory made it possible to obtain the "thermal signatures" of the common EM based on their characteristic thermal transitions such as melting, evaporation or decomposition. In this case, the required sensitivity to isolated nanogram-size particles of EM was achieved in the DC experiments using fast heating ramps (10^3 K/s). This demonstrates that this technique could be sensitive enough to detect explosives at the trace level in a real environment (e.g., terminal halls, train stations, etc.) with very fast data acquisition and analysis. The scientific objectives fulfilled during my PhD have been the following:

1. Calorimetric study of four different families of explosives and its mixtures. First studies [7] have shown that it is possible to obtain, with a single particle of micrometer size, a calorimetric curve specific to the explosive (thermal signature). Working at ultra-fast heating rates gives us the possibility of studying the decomposition process at ambient pressure. Currently, there is no other technique that would be able to provide, in a short period of time with a single microparticle weighing

a few nanograms, a specific curve of the explosive. In particular, the experiments allow to separate the melting and decomposition/evaporation events and to address both processes separately.

2. Development and setting of the nanocalorimetry technique. In this part of my PhD we will evaluate the heating rates that the nanocalorimeter is able to reach according to different types of sensors. For this purpose, we will try to develop different thermal programs taking advantage of the two working modes of the nanocalorimeter, which are the following:

   - linear heating ramps (the so-called DC calorimetry) that corresponds to classical calorimetry experiments except for the extremely high heating rates,
   - modulated regimes (AC calorimetry) where the two measured signals (amplitude and phase) will be processed in real time by spectral analysis technique (FFT algorithms).

   On the other hand, we will carry out a thorough study of the thermal gradients, which are built up across the active area of the chips during fast heating ramps.

[1] L. Allen, G. Ramanath, S. Lai, Z. Ma, S. Lee, D. Allman, K. Fuchs, *Applied physics letters* **1994**, *64*, 417–419.

[2] M. Merzlyakov, *Thermochimica acta* **2006**, *442*, 52–60.

[3] A. Lopeandia, J. Rodriguez-Viejo, *Thermochimica Acta* **2007**, *461*, 82–87.

[4] A. Minakov, A. Van Herwaarden, W. Wien, A. Wurm, C. Schick, *Thermochimica Acta* **2007**, *461*, 96–106.

[5] Xensor Integration, Online; accesed 04-15-2015.

[6] M. Rosenthal, D. Doblas, J. Hernandez, Y. Odarchenko, M. Burghammer, E. Di Cola, D. Spitzer, A. Antipov, L. Aldoshin, D. Ivanov, *Journal of synchrotron radiation* **2013**, *21*, 223–228.

[7] N. Piazzon, M. Rosenthal, A. Bondar, D. Spitzer, D. Ivanov, *Journal of Physics and Chemistry of Solids* **2010**, *71*, 114–118.

Résumé Étendu

Il est très important dans la lutte contre le terrorisme d'être capable de détecter de très faibles quantités de Matériaux Energétiques (ME). En plus des méthodes de détection des ME qui sont spécifiques à leur structure chimique, il est également envisageable d'utiliser l'importante variation d'enthalpie résultant du procédé de décomposition des ME pour les détecter au moyen d'une analyse thermique. Ce type d'analyse est loin d'être trivial. Pour cela, les techniques classiques, telles que la calorimétrie différentielle à balayage (en anglais Differential Scanning Calorimetry, ou «DSC»), nécessitent l'emploi de creusets spécialement conçu pour les hautes pressions. Une des difficultés vient du fait que l'augmentation de la pression est incontrôlable durant la mesure, de plus la DSC nécessite l'emploi d'une quantité importante de poudre (typiquement plus de 100 microgrammes). Cependant, la sensibilité d'une DSC classique est encore trop insuffisante pour détecter des particules de ME ayant une masse de quelques nanogrammes. Au contraire, la technique de calorimétrie sur membrane développée récemment est parfaitement adaptée à la caractérisation de faibles quantités de poudres [1, 2] et est donc totalement utilisable pour la détection.

Les premières notions de calorimétrie sur membrane ont été introduites par L. H. Allen et al. au début des années 90 [1]. Il était également le premier à réaliser des analyses thermiques sur des couches minces. Par la suite, il a étendu la technique à des échantillons aux géométries variées, telles que des particules microniques et des monocristaux de polymère. Grace au développement de l'industrie des semi-conducteurs, les capteurs calorimétriques utilisant des microsystèmes électromecaniques sont actuellement en mesure d'effectuer des mesures thermo-analytiques sur des échantillons extrêmement petits ayant une masse de l'ordre du nanogramme voire du picogramme. Les vitesses de chauffage et de refroidissement sont beaucoup plus élevées que dans une DSC classique. Ces vitesses sont comprises entre 10^2

et 10^6 K/s [2–4]. Par conséquent, les mesures effectuées par nanocalorimétrie sont extrêmement rapides (i.e. de l'ordre de quelques millisecondes).

Dans un des laboratoires (IS2M) dans lequel j'ai fait mon doctorat, le groupe de recherche dirigé par Dimitri Ivanov a construit avec l'aide d'ingénieurs russes une interface électronique de nanocalorimètre. L'utilisation de cet appareil permet d'effectuer des mesures sur des échantillons de taille nanométrique à des vitesses de chauffe élevées (jusqu'à 10^6 K/s). Bien que L. H. Allen et ses collaborateurs fabriquaient eux-mêmes les capteurs nanocalorimétriques, l'utilisation de capteurs commerciaux basés sur la technologie des semiconducteurs, représente une perspective prometteuse. Ces capteurs étaient initialement développés pour des mesures de conductivité thermique de gaz. Le nanocalorimètre utilise ces capteurs de gaz commerciaux constitués d'une membrane (film mince) de SixNy ayant des dimensions pouvant varier de 30×30 à 250×250 µm^2. Ces membranes comprennent des éléments chauffant résistifs ainsi que des thermocouples à soudure chaude situés à 50-100 µm des éléments chauffant [5]. Le capteur nanocalorimétrique peut soit être monté sur une base support conventionnelle de transistor TO-5 soit sur un connecteur céramique plat, qui peut être utilisé par exemple lors du couplage de mesures calorimétriques avec des mesures de diffraction des rayons X en transmission [6].

L'autre laboratoire dans lequel j'ai travaillé (NS3E) synthétise de nouveau matériaux énergétiques et évalue leur performance et leur utilisation potentielle pour des applications de type sécurité et défense.

Les premiers résultats de nanocalorimétrie [7] ont montrés que cette technique permet d'obtenir une signature thermique des ME classiques. En effet, leurs caractéristiques thermiques telles que la fusion, l'évaporation ou la décomposition sont visibles. Dans ce cas, la sensibilité requise pour obtenir des résultats sur des particules ayant une masse de l'ordre du nanogramme a été obtenue lors du chauffage linéaire et en utilisant une vitesse de chauffe rapide (10^3 K/s). Cela démontre que cette technique est assez sensible pour détecter des traces d'explosifs dans un environnement réel (aéroport, station de train,

etc.) avec une vitesse d'acquisition et de traitement des données très rapide.

Les objectifs scientifiques atteints durant ma thèse sont les suivant:

1. L'étude calorimétrique de quatre familles différentes d'explosifs et de leurs mélanges. Les premiers résultats [7] ont montrés qu'il est possible d'obtenir, avec une seule particule de taille micrométrique, une courbe de calorimétrie spécifique de l'explosif (signature thermique). Le fait de travailler avec des vitesses de chauffe élevées nous donne la possibilité d'étudier le procédé de décomposition à pression ambiante. Actuellement, aucune autre méthode est capable de fournir, dans un temps très court avec une seule particule micrométrique pesant quelques nanogrammes, une courbe spécifique de l'explosif. De plus, l'expérience permet de séparer les phénomènes de fusion et de décomposition/évaporation et d'examiner ces deux phénomènes séparément.

2. Le développement et la détermination de la technique de nanocalorimétrie. Dans cette partie de ma thèse nous avons évalué les vitesses de chauffe que le nanocalorimètre est capable d'atteindre en fonction des différents types de capteurs. Dans ce but, nous avons essayé de développer différents programmes thermiques tirant avantages des deux modes de fonctionnement du nanocalorimètre:

   - rampe de chauffe linéaire (également appelée calorimétrie DC), qui correspond à des expériences classiques de calorimétrie (DSC) sauf que les vitesses de chauffe appliquées sont très élevées.
   - régime modulé (calorimétrie AC) pour lequel les deux signaux mesurés (amplitude et phase) sont traités en temps réel par une technique d'analyse spectrale (algorithme FFT).

   De plus, nous avons effectué une étude minutieuse des gradients thermiques, qui sont présents dans la surface active du capteur durant un chauffage rapide.

[1] L. Allen, G. Ramanath, S. Lai, Z. Ma, S. Lee, D. Allman, K. Fuchs, *Applied physics letters* **1994**, *64*, 417–419.

[2] M. Merzlyakov, *Thermochimica acta* **2006**, *442*, 52–60.

[3] A. Lopeandia, J. Rodriguez-Viejo, *Thermochimica Acta* **2007**, *461*, 82–87.

[4] A. Minakov, A. Van Herwaarden, W. Wien, A. Wurm, C. Schick, *Thermochimica Acta* **2007**, *461*, 96–106.

[5] Xensor Integration, Online; accesed 04-15-2015.

[6] M. Rosenthal, D. Doblas, J. Hernandez, Y. Odarchenko, M. Burghammer, E. Di Cola, D. Spitzer, A. Antipov, L. Aldoshin, D. Ivanov, *Journal of synchrotron radiation* **2013**, *21*, 223–228.

[7] N. Piazzon, M. Rosenthal, A. Bondar, D. Spitzer, D. Ivanov, *Journal of Physics and Chemistry of Solids* **2010**, *71*, 114–118.

Contents

List of Abbreviations

AC	Alternating Current
CL-20	2, 4, 6, 8, 10, 12-hexanitro-2, 4, 6, 8, 10, 12-hexaaza-tetracyclo-[5, 5, $0^{3.11}$, $0^{5.9}$]-dodecane
DC	Direct Current
DESI	Desorption ElectroSpray Ionization
DSC	Differential Scanning Calorimetry
HMX	1, 3, 5, 7-tetranitro-1, 3, 5, 7-tetraaza-cyclooctane
IMS	Ion Mobility Spectrometry
LIBS	Laser Induced Breakdown Spectroscopy
LOD	Limit Of Detection
MDSC	Modulated Differential Scanning Calorimetry
MEMS	Micro-Electro-Mechanical Systems
MIP	Molecularly Imprinted Polymer
NMR	Nuclear Magnetic Resonance
PETN	3-nitrooxy-2, 2-bis(nitrooxymethyl)propylnitrate
PnSC	Parallel nano-Scanning Calorimeter

POM	Polarized Optical Microscopy
RDX	$1,3,5$-trinitroperhydro-$1,3,5$-triazine
RS	Raman Spectroscopy
SERS	Surface Enhanced Raman Spectrocopy
TDSC	Thin-film Differential Scanning Calorimetry
THzS	TeraHertz Spectroscopy
TNT	2-methyl-1,3,5-trinitrobenzene
WAXS	Wide-Angle X-ray Scattering

Chapter 1

Introduction

In this chapter a brief description of the work pursued in this thesis will be given. An introduction to thermal analysis and its methods is presented as well as the state of the art of the Nanocalorimetry as a novel technique that can be combined with others, i.e. X-ray scattering, to have a bigger picture of both structure and the behaviour of the samples.

The second part of the chapter is dedicated to energetic materials and the problematic of their detection. A general review of the current methods used to detect these materials will be exposed.

1.1 The aim of this work

In order to determine whether it is possible to use Nanocalorimetry as a tool for detecting and characterizing explosives in the form of single micron-sized particles in this work we were focused on three basic objectives:

- **Nanocalorimetric study of different families of explosives and co-crystals**. Previous studies have shown that it is possible to obtain with a single micron-sized particle, a nanocalorimetric signature specific to the explosive (thermal signature) [1, 2]. Currently, there is no other technique that would be able to provide, in a short period of time and with a single micro-particle of a few nanograms, the specific thermal signature of a given explosive. In particular, the experiments allow to separate melting and decomposition and to address both processes separately and quantitatively. Co-crystals were studied to have a better understanding of some aspects of the thermal behavior of pristine compounds.

- **Optimization and better understanding of the Nanocalorimetry technique**. For this purpose, we attempted to develop different approaches taking advantage of the two working modes of the nanocalorimeter:

  - DC calorimetry that corresponds to conventional calorimetry experiments except that extremely high heating/cooling rates are used.
  - Modulated regimes (AC calorimetry) where signals are processed in real time by spectral analysis technique (Fast Fourier Transform algorithms).

- **Combination of Nanocalorimetry with X-ray diffraction**. Using a set-up provided by the nanocalorimeter interface, which was compatibilized with the environment of the ID13 beamline of the European Synchrotron Radiation Facility (ESRF), a better understanding of decomposition and crystallization processes will be achieved.

1.2 General background in calorimetry

The use of calorimetric experiments to study the thermal behavior of materials has a long history. First calorimeters were developed more than 200 years ago (e.g. the first ice-calorimeter of Lavoisier-Laplace [3]). Nowadays, calorimetry can be considered as one of the main techniques on thermal analysis, meaning "by measuring the heat absorbed or released by the sample, it is possible to study the relationship between a sample's property and its temperature while this is heated or cooled in a controlled manner" [4] (cf. Figure 1.1). That is the definition of calorimetry given by the International Confederation of Thermal Analysis and Calorimetry (ICTAC) [5].

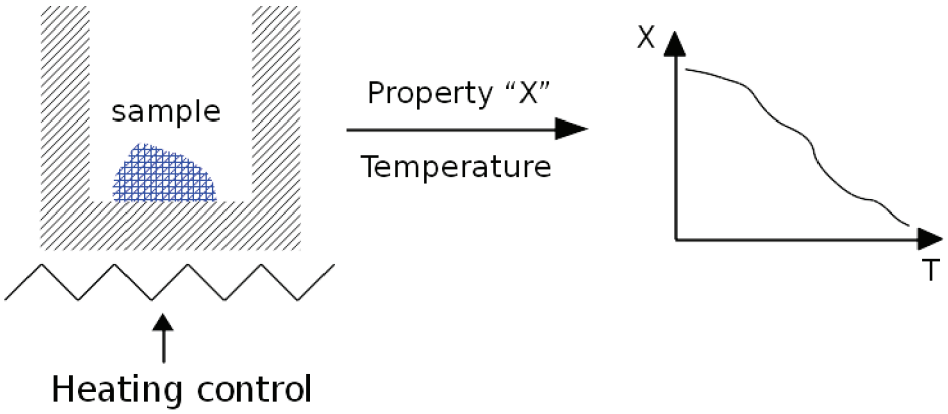

Figure 1.1 – General principle of thermal analysis [6].

Nowadays, calorimetry has become a routine technique of physical characterization of materials. Most of physical and chemical modifications of matter are associated with thermal effects whereby heat is absorbed, the so-called *endothermic phenomena* (e.g. melting), or released (e.g. decomposition) in *exothermic phenomena*. Such effects are measured with experiments performed using Differential Scanning Calorimetry (DSC), one of the most established method in thermal analysis that measures the heat flow rate (heat-flux DSC) or the electrical power (power compensating DSC) difference between a sample and a reference material as a function of temperature. For such experiments, DSC is a suitable technique that allows to characterize kinetic and thermodynamic properties of thermal transitions like decomposition

or phase transition processes of the first and second order.

Typically DSC measurements are carried out on bulk samples with masses ranging from grams to milligrams. When it is required to measure samples in the nanogram range, the calorimetric measurements are problematic, since the amount of energy absorbed or released by a given transition is too small to be measured with accuracy using conventional calorimeters [7].

In the last years, new calorimeters capable to measure very small amount of samples have been developed because of the needs to measure new phenomena related to the nanoscale behavior of matter [8]. Generally in calorimetry the fundamental measuring issue is related to the calorimetric cell-sample heat capacity ratio, since the calorimetric signal is proportional to the total heat capacity (i.e. the sum of the sample heat capacity and the cell, or addenda, heat capacity), but the useful signal is only proportional to the sample heat capacity. Therefore, it is necessary to reduce the heat capacity of the empty calorimetric cell to enhance the useful signal. This concept has been guiding the advances in the design of new calorimeters, but it is not the only requirement. The difficulty to reduce the thermal link between the sample and environment for adiabatic measurements of the heat capacity is another problem that should be considered [7].

Types of calorimeters

Modern calorimeters are characterized by improved sensitivity, signal-to-noise ratio, baseline stability and other parameters allowing to perform really precise measurements of temperature and heat flow on a wide variety of sample masses. to several grams. There are several classifications of calorimeters due to the great variety of devices developed since the first one. Indeed, there are more than 100 different types and it is rather difficult to establish a comprehensive list including all of them.

A very basic classification is based on the heat exchange between the system (sample and empty cell) and its surrounding [4]. This parameter allows to define two broad families of instruments:

- *Adiabatic calorimeters*, where the heat exchange between the system

and its surrounding is avoided.

- *Diathermal calorimeters*, the heat exchange is favoured.

The two types of instruments defined above can be further subdivided into four groups:

- *Passive adiabatic calorimeters* use an appropriate thermal insulation to decrease to the minimum the heat exchange between the system and its surrounding.
- *Active adiabatic calorimeters* in which the method to reduce the heat exchange is to decrease the temperature difference between the sample and its surrounding thanks to electronics. The surrounding temperature is the one which is controlled.
- *Passive diathermal calorimeters*, where a good thermal conduction assures a good heat exchange between the system and its surrounding.
- *Active diathermal calorimeters*. In this type of calorimeters the heat exchange is simulated, meaning that the heat transfer between the system and its surrounding is replaced by a physical phenomenon which takes place in close contact with the sample generating or removing heat.

As Hemminger and Höhne stated [9], there is such a number of different calorimeters that it is difficult for some of them to be classified in a particular category. They proposed to use simultaneously following three characteristics to classify any calorimeter.

- Based on the construction principle:
  - Single calorimeters
  - Twin or differential calorimeters
- Based on the measuring principle:
  - Compensation calorimeters

        * Compensation by a phase transition
        * Compensation by electric effects
        * Compensation by the chemical heat of reaction
    - Temperature differences calorimeters
        * Time-dependent temperature differences
        * Local temperature differences, simultaneous determination in two different positions:
            · Flow calorimeters
            · Heat-flux calorimeters

- Based on the mode of operation:
    - Isothermal calorimeters: the system and its surrounding remains at the same temperature. This mode can be passive or active, as it is described above.
    - Isoperibolic calorimeters: In this case, the environment of the calorimetric cell remains at constant temperature whilst the sample temperature changes.
    - Adiabatic calorimeters: the temperature of the surroundings is controlled to be equal to the temperature of the system, thus the heat exchange is negligible.
    - Adiabatic scanning calorimeters: a linear heating rate is applied to the system.
    - Isoperibolic scanning calorimeters: a linear heating rate is applied only to the system, as for adiabatic.
    - Scanning of the surroundings: a linear heating rate is applied to the surroundings.

1.3 Differential Scanning Calorimetry

A definition of Differential Scanning Calorimetry is the measurement of the heat flow rate between a sample and a reference while they follow a controlled

temperature program [4]. A DSC is the device that measures these changes. The acronym DSC is shared between the device and the technique itself. It also allows the determination of heat capacities in both solid and liquid phases, phase transition temperatures and the corresponding enthalpy and entropy changes. On the other hand it is well known from dynamic measurements, like dielectric spectroscopy or dynamic mechanical analysis, that the signal-to-noise ratio can be significantly improved if only the response of the sample at the specific frequency of the perturbation is analysed. The data treatment is then often based on Fourier analysis of periodic signals.

Nowadays, two basic types of calorimeters are the most used:

- Heat Flux DSCs
- Power Compensating DSCs

A heat-flux DSC (cf. Figure 1.2) comprises a stage with two sample positions both connected to the furnace via a thermal resistor of known thermal properties, e.g. the heat capacity and thermal conductivity measuring the difference in temperature between the sample and the reference. The heat-flow rate difference (HF) between the sample and the reference is given by:

$$HF = \frac{\Delta T}{R_r} + \Delta T_0 \left(\frac{1}{R_s} - \frac{1}{R_r} \right) + (C_r - C_s)\frac{dT_s}{dt} - C_r \frac{d\Delta T}{dt} \tag{1.3.1}$$

where

- ΔT is the temperature difference between the sample and the reference,
- ΔT_0 is the temperature difference between the sample and a reference close to the furnace,
- T_s is the sample temperature,
- R_s, R_r are the sample and reference temperature, respectively,
- C_s, C_r are the sample and reference heat capacities, respectively

These parameters are determined during the calibration procedure although, for most of the heat-flow DSCs in the market, only the first term of the Equation 1.3.1 is considered.

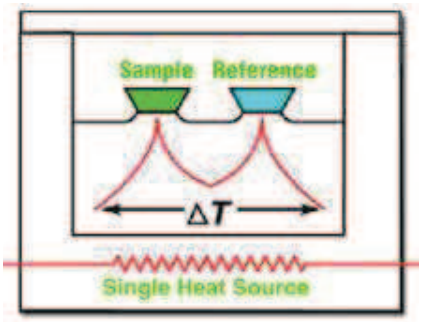

Figure 1.2 – Heat-flow DSC scheme [10].

The heat exchange between crucibles and furnace occurs via the purge gas by the three heat transfer mechanisms, i.e. conduction, convection and radiation. This heat exchange varies when the sample changes its properties or when the thermal contact is modified by consecutive measurements. This problem limits the accuracy of these type of devices for heat capacity measurements to about 5% [11, 12].

On the other hand, in a power compensating DSC (cf. Figure 1.3) sample and reference are placed in two separate furnaces, each of them with individual heating elements and temperature sensors. The device compensates the heating power supplied to each furnace by measuring the temperature difference between them and trying to keep this difference at a minimum, although there is always a residual temperature difference (offset). When there is a temperature difference between the sample and the reference due to a thermal event, and therefore, there is a change in the heat capacity (C_p), the heating power required ($\Delta\phi$) to keep the temperature difference as small as possible is given by:

$$\Delta\phi \cong \Delta C_p \cdot \beta \tag{1.3.2}$$

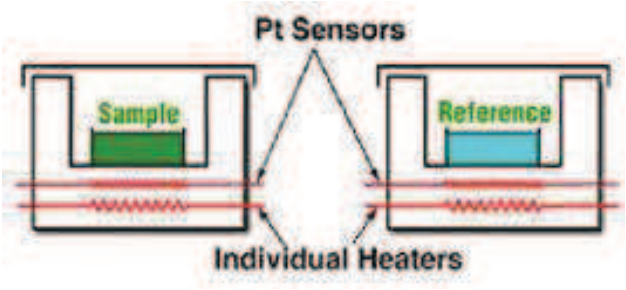

Figure 1.3 – Power compensating DSC scheme [10].

Thermodynamic considerations

The main equation in calorimetry is the following:

$$\frac{dH}{dt} = C_p \frac{dT}{dt} + f(T,t) \tag{1.3.3}$$

where:

- $\frac{dH}{dt}$ is the total heat flow measured by the DSC,
- C_p is the extensive heat capacity,
- $\frac{dT}{dt}$ is the heating rate,
- $f(T,t)$ is a kinetic term, which is function of the time and temperature.

For a given sample, the heat flow due to its heat capacity is linearly proportional to the heating rate, meaning that at zero heating rate, this heat flow should be also zero. So any heat flow detected at this hypothetical rate must be due to kinetic processes in the sample.

But it is not possible to make any calorimetric experiment with zero heating/cooling rate. That is a reason why modulation calorimetry was developed. The purpose of Modulated DSC is to separate these two parts from the total heat, i.e., the part corresponding to the heating rate and the

part corresponding to the kinetic processes. It was developed to overcome the natural limitations of conventional DSC. When really subtle transitions, such as weak glass transition temperatures in highly crystalline polymers are measured in a conventional DSC, one can find a lack of sensitivity, i.e., ability to detect transitions that occurs during the analysis. So in order to increase the sensitivity, according to Equation 1.3.3, it is necessary to increase the sample size, the heating rate or both.

But these increments in both sample size and heating rate decrease the resolution because a larger temperature gradient appears. MDSC applies two signals simultaneously:

- a slow linear heating rate to improve resolution,
- a modulated signal to improve sensitivity

Another limitation of conventional DSC is to measure the heat capacity under isothermal conditions. Since MDSC has two independent signals, one of them can establish isothermal conditions, i.e., zero rate while the modulated signal "modulates" superimposed to the linear one. This approach allows to measure the sample's heat capacity and to analyse changes in the sample properties as a function of time at isothermal conditions.

Modulated Calorimetry

O. M. Corbino developed this theory in 1910 considering a wire sample heated by an AC current passing through it [13]. He got an expression for the temperature oscillations in the sample which is valid for other methods of modulation of the heating power. If a sine wave modulates the power heating the sample, the temperature of the sample starts to oscillate around a mean value T_0. The amplitude of these temperature oscillations depends on the heat capacity of the sample.

For a sample in a temperature-modulated regime, the heat balance equation (heat input = heat accumulated in the sample + heat losses) for a short interval Δt can be expressed as

$$(p_0 + p\sin\omega t)\Delta t = mc\Delta T + Q(T)\Delta t \tag{1.3.4}$$

where

- $p_0 + p\sin\omega t$ is the modulation heating power,
- m, c and T are the mass, specific heat and temperature of the sample,
- $Q(T)$ is the power of heat losses from the sample
- ΔT is the change of temperature during the interval Δt

By making these three assumptions $T = T_0 + \Theta$, $\Theta << T_0$ and $Q(T) = Q(T_0) + Q'\Theta$, one can obtains

$$p_0 + p\sin\omega t = mc\Theta + Q(T_0) + Q'\Theta \tag{1.3.5}$$

where

- $Q' = \dfrac{dQ}{dT}$ is the heat transfer coefficient
- $\Theta' = \dfrac{d\Theta}{dt}$

The previous equation has the following solution if one considers the steady-state

$$Q(T_0) = p_0, \tag{1.3.6}$$

$$\Theta = \Theta_0 \sin(\omega t - \phi), \tag{1.3.7}$$

$$\Theta_0 = (p/mc\omega)\sin\phi = (p\cos\phi)/Q' = p/(m^2c^2\omega^2 + Q'^2)^{1/2}, \tag{1.3.8}$$

$$\tan\phi = mc\omega/Q, \tag{1.3.9}$$

where ϕ is a phase shift between the temperature oscillations and the power oscillations dissipated in the sample. It is considered adiabatic regime when $\tan\phi >> 1 (\sin\phi \cong 1)$. When the phase shift ϕ is close to 90°, the corrections for heat losses are negligible. This means that the oscillations of the heat losses due to the temperature oscillations are much smaller than the

oscillations of the heating power. Under these conditions, the heat capacity of the sample is given by

$$mc = p/\omega\Theta_0 \tag{1.3.10}$$

which is the basic equation of modulation calorimetry. If the conditions are non-adiabatic, the previous equation transforms into

$$mc = (p/\omega\Theta_0)\sin\phi \tag{1.3.11}$$

from where one could determine the heat capacity once known the phase shift between the oscillations of the power dissipated in the sample and the temperature oscillations.

1.4 Fast Scanning Calorimetry

Fast Scanning Calorimetry takes advantage of the well-established MEMS-based technology using sensors with a very low thermal inertia. It is possible to reach quasi-adiabatic conditions [14] since the extremely high heating rates gives no time for dissipation of the heat which is consumed by increasing the temperature of the active area:

$$P(t) = C_p(T) \cdot \beta \tag{1.4.1}$$

where C_p (T) is the sum of the heat capacity of the empty cell (or addenda) and the heat capacity of the sample.

Due to the constantly growing interest in the nano-scale behavior of matter, fast scanning calorimetry has become a major tool in terms of characterization. The heat flow absorbed or released by samples in the nano-gram range is extremely small (in the order of nW) and, therefore, it can not be measured with a conventional DSC. A solution to overcome this is to use lighter calorimetric sensors, which can increase the heating rate inversely proportional

to the sample mass [15–17]. There are more reasons for the interest in fast scanning calorimetry [18] as the study of non-equilibrium states for a better understanding of the real process conditions and the combination of the technique for an in-depth characterization of the sample [19–22]. Therefore it is clear that this technique provides the way to achieve purely amorphous state of materials ranging from metals [23] to polymers [24] or semiconductors [25] and to study their thermodynamic properties for a better understanding of the properties of these new states [26].

A small overview of the brief history of the technique will be given in the next paragraphs. Allen and coworkers were the first ones who developed the technique in the middle 90s [27], although F. Hellman at the University of California was the first one in reporting. Allen's nanocalorimeter was based on the thin-film technology developed at Cornell University. By using a Ni thin-film stripe (cf. Figure 1.4), they could heat and measure the temperature at the same time achieving a sensitivity of J/m^2 [28] in their TDSC.

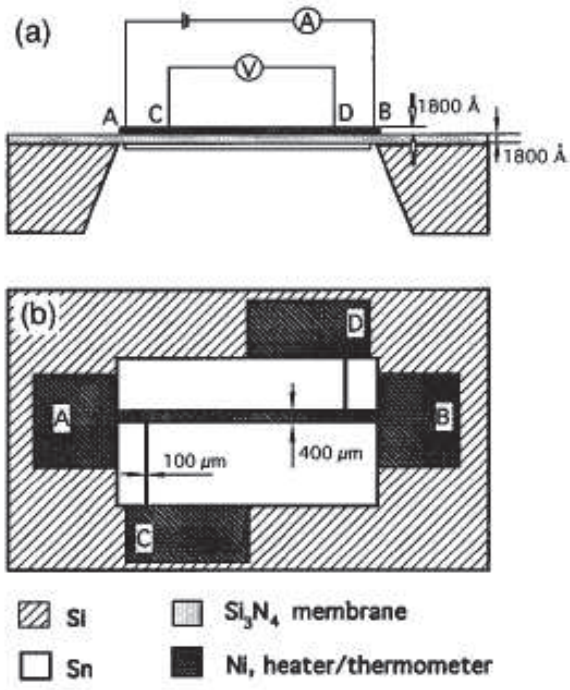

Figure 1.4 – Cross-sectional and planar cut of the microcalorimeter designed by Allen et al.

Some years later, Allen et al. taking advantage of the emerging field of MEMS, designed a new differential scanning chip calorimeter (cf. Figure 1.5). With this new apparatus, not only the sample's specific heat could be measured, but also the heat released or absorbed in physical or chemical processes [29].

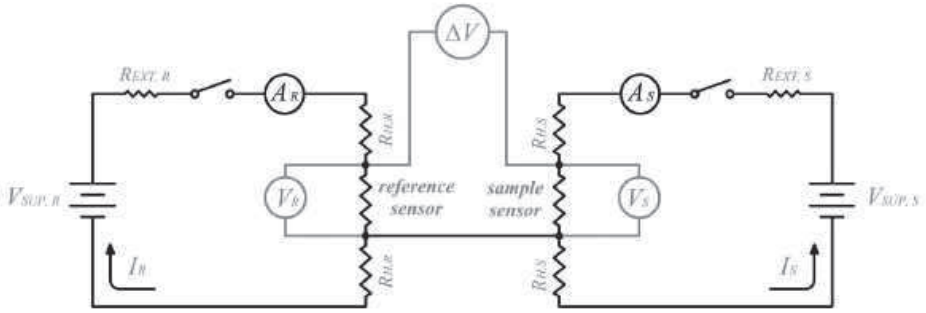

Figure 1.5 – Schematics of the differential scanning calorimeter designed by Allen et al.

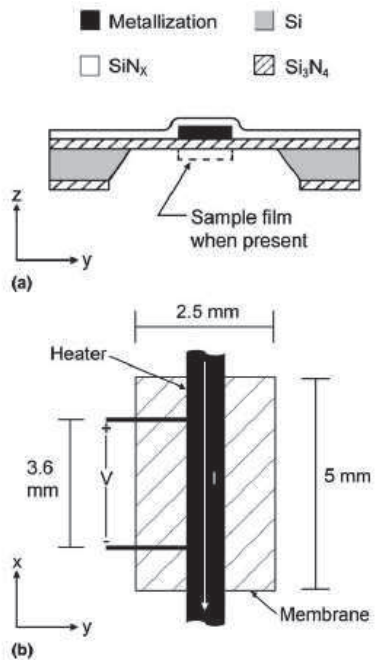

(a) Schematic layout of one of the cells.

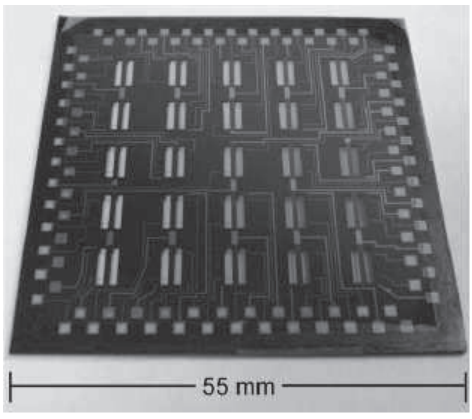

(b) Photograph of the 5x5 array of thermal sensors used by the PnSC.

Figure 1.6 – Schematics and picture of the Vlassak's PnSC.

Another nano-differential scanning calorimeter was developed using Allen's work as a base. This new design made by Prof. Vlassak (cf. Figure 1.6), the parallel nano-scanning calorimeter with its 5×5 array of thermal sensors allows to simultaneously measure 25 samples [30]. Its design allows a combination of in-situ Nanocalorimetry and X-ray diffraction, as it will be described in the next subsection.

It is also important to mention the development of Lopeandía and coworkers at Universitat Autònoma de Barcelona who designed a membrane-based nanocalorimeter similar to the one of Allen (cf. Figure 1.7). They also fabricate their own sensors [31].

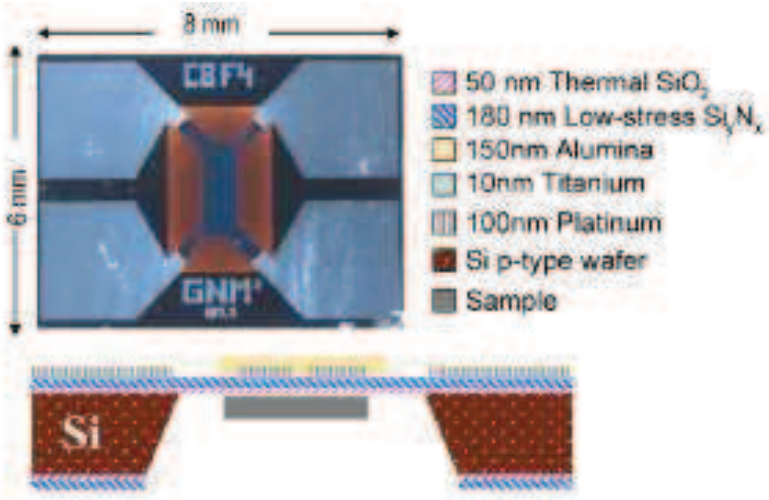

Figure 1.7 – Schematics of the nanocalorimeter designed by Lopeandía et al.

In Prof. Schick´s group, a fast scanning power compensated differential scanning nanocalorimeter was constructed (cf. Figure 1.8). It uses commercial gas sensors from Xensor Integration [32]. The extreme sensitivity of these sensors due to their very small addenda heat capacity (nano- and even pico-joules per Kelvin) [27, 33] permit to the Schick's nanocalorimeter to reach scanning rates up to 10^6 K/s [26]. The use of these sensors allow to diminish the problem that all calorimeters have to deal with. It is the achievement of controlled, constant rates on heating and especially during cooling, although great efforts have been done to minimize them, i.e. via power compensation

systems [34] or by adopting different gas atmospheres, such as helium or argon [18, 26, 35–37].

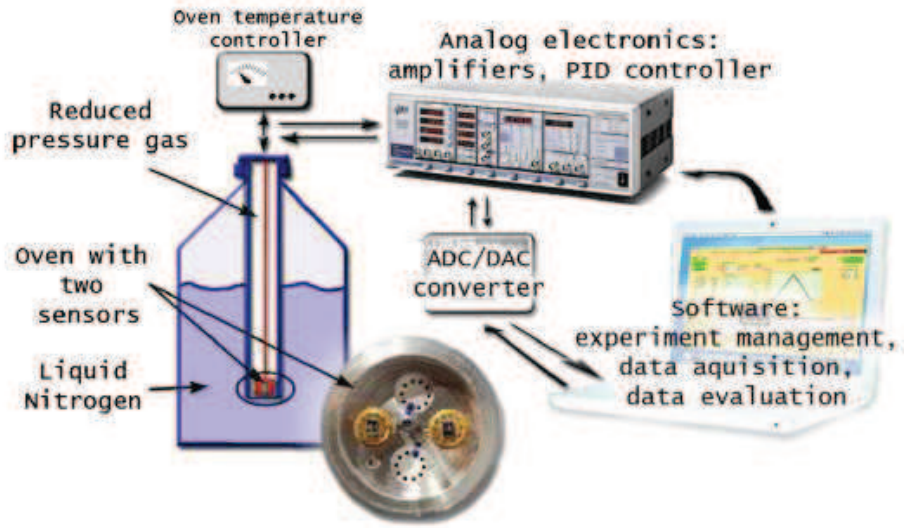

Figure 1.8 – Setup of the fast scanning calorimeter designed by Schick et al.

Figure 1.9 – Picture of the Flash DSC 1 by Mettler-Toledo.

It is worth to mention that since the last years, commercial nanocalorimetric instruments are available [38]. This devices, commercialized by Mettler-Toledo (cf. Figure 1.9), can not compete with the state-of-art nanocalorimeters described above in terms of high scanning rates, but they do in terms of stability and reliability.

Using the strategy of Schick's nanocalorimeter employing commercial gas sensors, Ivanov et al. developed with the help of russian engineers an electronic interface for a nanocalorimeter (cf. Figure 1.10), which allows to perform quantitative DC and AC calorimetric measurements over a broad range of heating/cooling rates (up to 10^5 K/s) and temperature modulation frequencies (up to 1 kHz).

Figure 1.10 – Picture of the electronic interface developed by Ivanov et al.

The flexibility, in terms of compatibility with different setups, allows to this electronic interface in-situ combination of nanocalorimetric measurements with nano X-ray diffraction in transmission [20, 22].

Moreover, inspired by the work of Zuck et al. who wrote a paper on explosive detection by means of thermal analysis [39], the approach of using Nanocalorimetry as a detection tool conducted Ivanov to use it as a proof of principle [1, 2].

It is important to mention also other research groups who use micro- or Nanocalorimetry to detect energetic materials.

Thus, Liu et al. [40] developed a system capable of providing rapid, portable, and inexpensive detection of energetic materials using calorimetric techniques (cf. Figure 1.11).

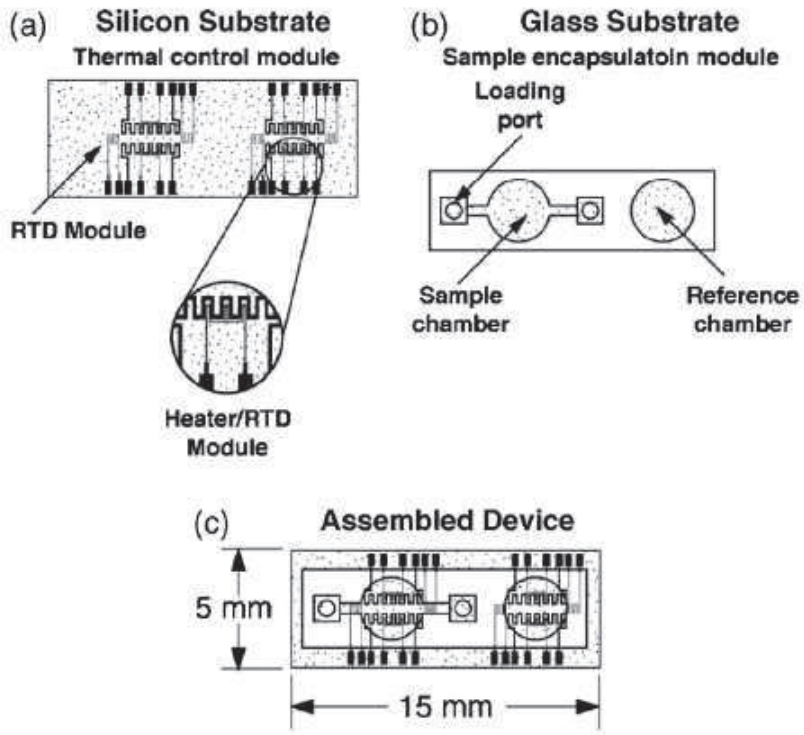

Figure 1.11 – Schematics of the microcalorimeter developed by Liu et al.

Carreto-Vazquez et al. inspired by the some papers published [1, 39, 40] and by the patent of Bannister et al. [41] developed another MEMS-based miniaturized calorimeter for screening energetic materials. In their design (cf. Figure 1.12), the use of the thick membrane on the device make it less sensitive than others MEMS-based calorimeters, despite it can be more robust for an use in real environments. But there is no real examples of calorimetric curves using energetic materials in this paper.

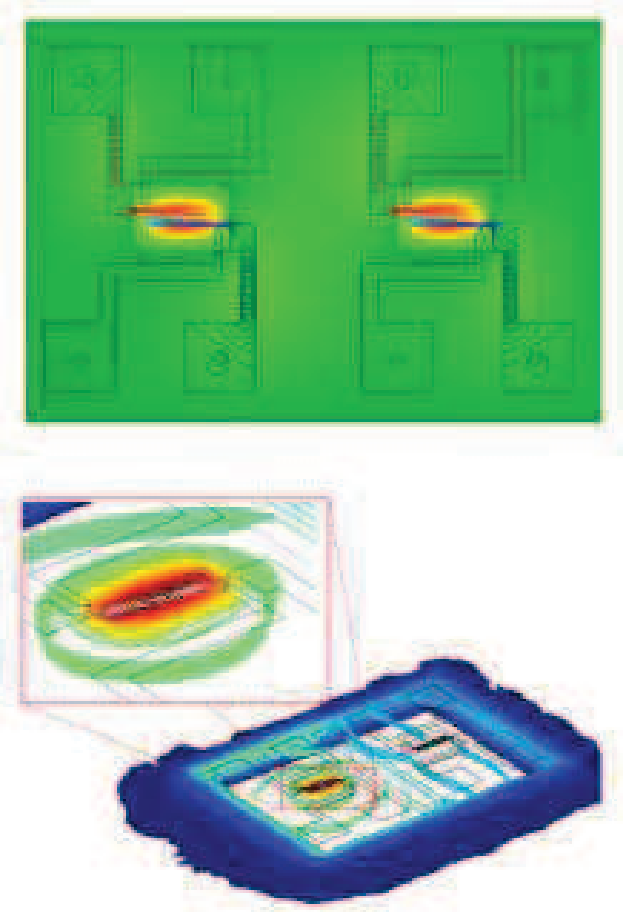

Figure 1.12 – 2D and 3D schematics of the prototype designed by Carreto-Vazquez et al.

1.4.1 Combination of Nanocalorimetry with other techniques of physical-chemical characterization

In the last years, several papers have been published on the combination of Nanocalorimetry with different techniques, especially X-rays. The combination of different experimental techniques in a single experiment is often beneficial for the in-depth knowledge of the sample. For example, as far as the structural analysis by X-ray scattering is concerned, simultaneous thermal

analysis provides important supplementary information about the type of the thermal transition and the sample state (e.g., glassy versus rubbery state, phase transitions of the first and second order). Nowadays, coupling X-ray scattering with conventional DSC has become a routine technique due to an increasing need to address nanostructured materials using nano-focus X-ray beams. However, combining conventional DSC instruments with these setups remains highly problematic due to the technical constraints of such beamlines. That is the main reason why this topic has acquired such a relevance in these last years. Examples of this combination have been by published by several authors:

- Prof. Vlassak and coworkers used its Parallel nano-Scanning Calorimeter (PnSC) (cf. Figure 1.13), in combination with synchrotron X-ray diffraction. They have studied basically thin-films, for example melting and solidification of elemental metals, martensite-austenite phase transformation behavior of shape memory alloys and metallic glasses [19, 21, 30, 42, 43].

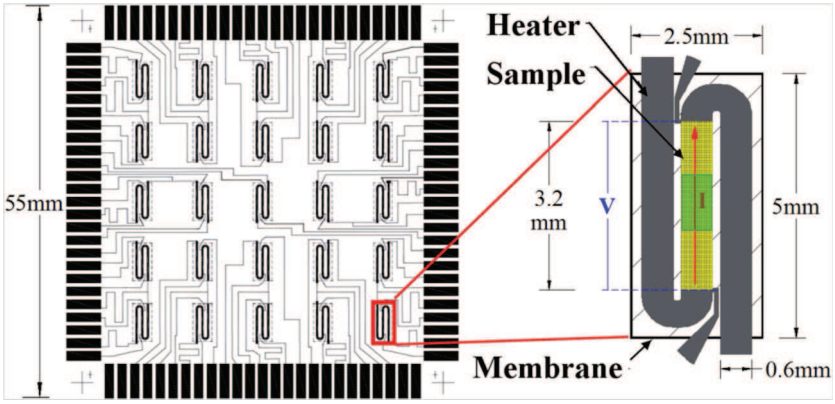

Figure 1.13 – Schematic of the PnSC device and calorimetry sensor developed by Prof. Vlassack [19].

- Rosenthal and Doblas et al. combined for the first time in-situ nanocalorimetry and nanobeam diffraction (cf. Figure 1.14) studying the thermal behavior of a single nanogram-sized Indium particle. Using the nanocalorimetric sensor as a bolometer, high resolution thermal

imaging of the single Indium particle was performed opening a new field of application to such MEMS-based calorimetric systems for studying thermal effects in materials in combination with high resolution X-ray nano beam diffraction [20].

- Riekel et al. used the same set-up to study transformations of noble metal nanoparticles with ligand shells [22]. In this case, SAXS measurements were performed.

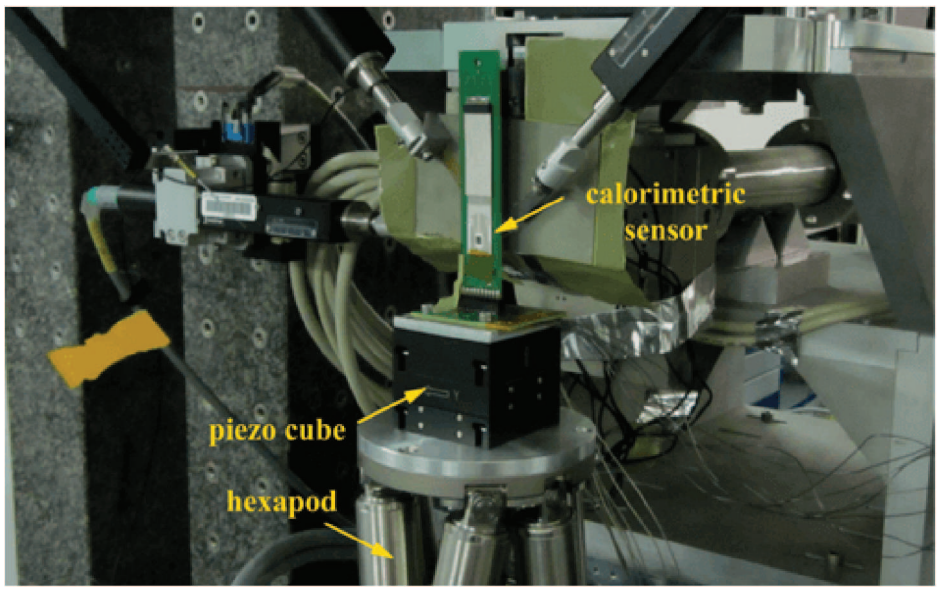

Figure 1.14 – View of the set-up for in-situ Nanocalorimetry and nanobeam XRD [20].

But not only the combination with X-rays has been done. Grapes and coworkers have managed to characterize dynamic processes by using in-situ techniques which allow to observe in real time the state of the system. They combined dynamic transmission electron microscope (DTEM) with Nanocalorimetry (cf. Figure 1.15) to study phase transformations on thin-films memory shape alloys [44, 45].

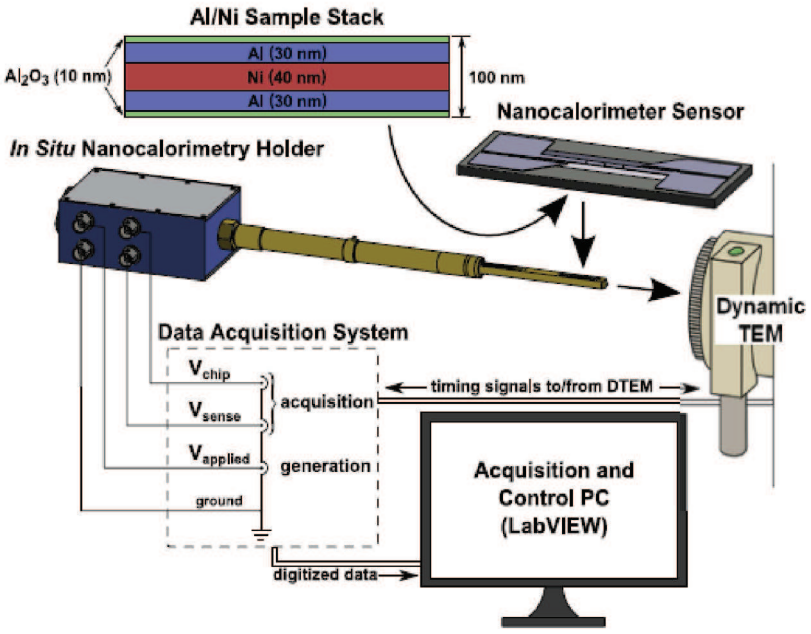

Figure 1.15 – Schematics of the system for in-situ Nanocalorimetry and dynamic TEM [45].

Although it is not an in-situ combination due to device constraints, it is worth to recognize the work done by van Drongelen et al. where they manage to combine the sensors from a Mettler-Toledo Flash DSC 1 device with microfocus WAXS from a synchrotron source [46].

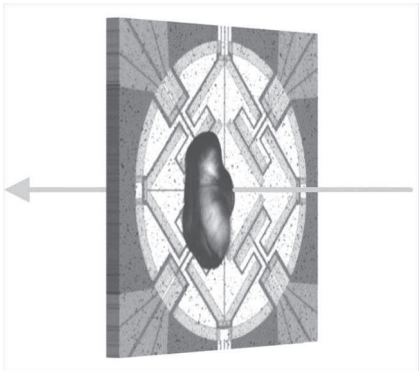

Figure 1.16 – iPP sample placed on a Flash DSC 1 sensor for measurement at the BM26 line of the ESRF [46].

Donald and coworkers used a Nanocalorimetry approach to investigate interactions between ions, electrons and water by using an ion Nanocalorimetry in a mass spectrometer [47].

1.5 Energetics materials

Energetic materials have two faces for the mankind. On the one hand, they are very useful materials for applications such as mining to extract metals, coal and many other raw materials. They have been used on huge excavations and soil movements, e.g. the Panama Canal and Hoover Dam among others. Without them, the modern society that we all know, could never have developed in the way that it does today. On the other hand, they have been terrifying people since the use of the "Greek fire" used by the Byzantine Empire, almost 2000 years ago. Their military uses and their destructive capabilities have caused uncountable casualties along the history. But the benefits of controlling their power and its development have never stopped. Our actual knowledge on explosives has been raised by trial and error since hundreds of years [48]. Even nowadays, we do not completely understand some details of their behavior. That is why the research effort for these materials is an on-going field.

When one talks about energetic materials, it is typically about the substances that are capable of releasing significant amounts of energy in form of pressure and heat during a very short time due to intramolecular redox mechanisms. The result of such a process is a highly exothermic reaction. For an efficient reaction, a balance between the fuel and the oxidizer is required. This balance is known as the oxygen balance. In the most efficient military explosives used nowadays, both fuel and oxidizer are present in the same molecule.

Depending on the velocity of the propagation of this exothermic reaction (slower or higher than the speed of sound or simply oxidation) different regimes

are defined. Combustion is the slowest mechanism of decomposition for energetic materials. The process is characterized by complete oxidation of the initial products, leading to combustion residues. This type of reaction requires large amounts of oxygen. Usually majority of energetic materials have a negative oxygen balance so the required oxygen must be provided by the environment. Another characteristic that permits the combustion process is that the material should be spread over a large area to facilitate the oxygen transfer and the heat dissipation. If these two latter requirements are impeded, the combustion process can turn over into a deflagration or a detonation process.

Deflagration occurs when the reaction front has a propagation velocity slower than the speed of sound. The front propagates in the same direction as the heat flow (cf. Figure 1.17). The heat released by this front acts like a trigger heating up the rest of the non-reacted material. Products like C, CO or others with a low oxygen content are typical for deflagration reactions due to the negative oxygen balance of the explosive [49].

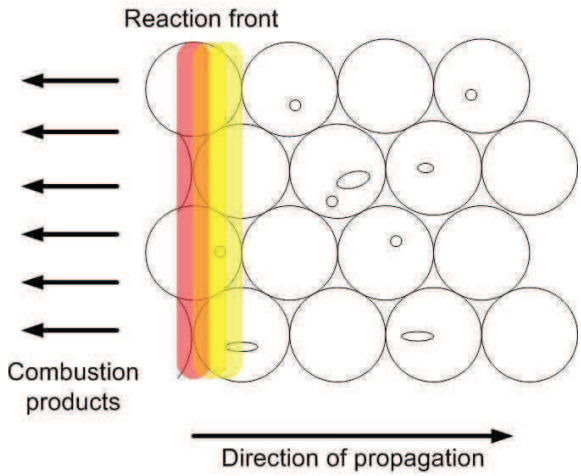

Figure 1.17 – Deflagration scheme of a explosive reaction.

In a detonation process, the shock-wave crossing the explosive produces a dynamic compression zone [50] that can auto-support its speed, which is faster than the speed of sound. This effect provokes strong and localized heatings in specific areas which lead to a new detonation in a similar way as

for chain reactions (cf. Figure 1.18).

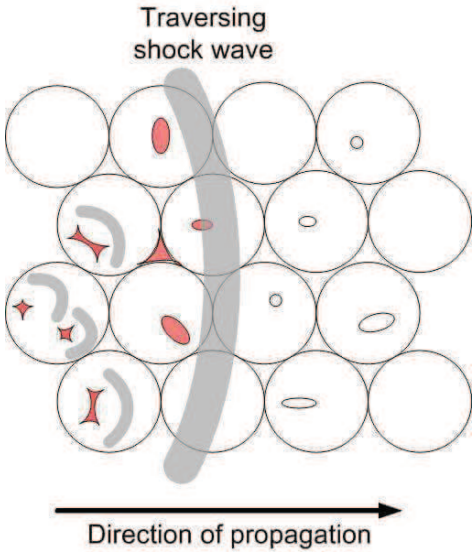

Figure 1.18 – Detonation scheme of a explosive reaction.

Classification of energetic materials

The most important feature of energetic materials is their stability and their reactive performance, which determines the fields of their practical use. They can be classified following different approaches, such as:

- by the decomposition behavior
  - Propellants — Rocket fuel, black powder,
  - Explosives.
    - Primary — $Pb(N_3)_2$, ONC-Hg-CNO
    - Secondary — TNT, RDX
- by the principal chemical group
  - Nitramines — RDX, HMX, CL-20,
  - Nitro aromatics — TNT, NT,

- Nitrate esters — PETN, NG,
- Peroxides — TATP.

Propellants

Propellants are materials that contain both fuel and oxygen source in the same molecule, although this is also valid for some explosives. Their principal characteristic is that they can only burn but do not explode. The burning process is produced rather violently but with a low rate of combustion, usually accompanied with flames, sparks and a strong sound but not with detonation, which must be avoided for these materials.

That is the main reason why they are used in applications where a pushing effect is required, like rocket fuel or gunpowder [50, 51].

Primary explosives

Primary explosives are materials that can rapidly pass from burning to detonation. They are very sensitive and can detonate easily by the action of a moderate external stimulus like heat, shock, etc. They are able to induce the detonation to less sensitive materials, like secondary explosives, due to their highly brisant and triggering velocity. For these reasons, they are used as detonators and primers for secondary explosives [50, 51].

There is a threshold value to classify the explosives into primary or secondary. This threshold is the impact and friction sensitivity of pentaerythritol tetranitrate (PETN), 3 Nm and 60 N, respectively, meaning that all explosives having a sensitivity higher than PETN are considered as primary explosives. Obviously, if they are less sensitive, they are considered as secondary explosives [51].

Secondary explosives

Within this section are included all explosives initiated by the detonation of a primary explosive. They cannot be easily detonated by heat or shock [51]. They are much less sensitive to external stimuli than primary explosive but, on the other hand, they are much more powerful. In certain cases, the secondary

explosive is so stable that the primary explosive must be coupled with an additional booster-charge, otherwise no reaction will occur.

Generally, it is said that the initiation of an explosive is triggered by heat [52]. But, also other types of energy as mechanical or electrical, i.e.:

- impact,
- friction,
- electrostatic discharge,

can trigger the initiation reaction due to their conversion into thermal energy in the "hot spots", localized regions where the release of energy is greater than the dissipation of energy by heat losses [53]. This process is similar to a sequence cascade as it is pictured in Figure 1.19.

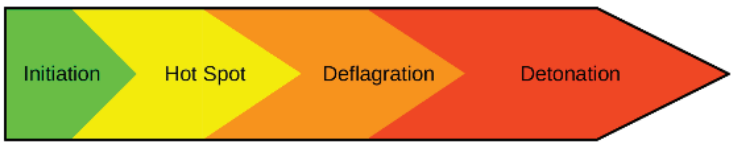

Figure 1.19 – Evolution of the detonation process [54].

Once the explosive has been initiated, the reaction can evolve following the different processes [48, 52] like:

- adiabatic compression of defects, such a cavities, voids, impurities,
- viscous and plastic deformation,
- frictional heating,
- inter-crystalline shearing,
- spark discharge.

To achieve a deflagration or a detonation, previous processes should last a few milliseconds and they have to raise the temperature in a micron-sized region to more than 700 K [53], forming the hot spots.

The heat releasing and the heat dissipation processes are dependent of all the steps mentioned in the scheme above. So if the heat releasing is the dominating process, the reaction can turn into a detonation, otherwise if it is the heat dissipation the main mechanism, the decomposition of the explosive may be blocked by itself [54].

Co-crystals: a new trend in the synthesis of energetic materials

In the last years, co-crystallization [55] has become a hot topic in many fields ranging from pharmaceuticals [56], non-linear optics [57], ferroelectrics [58], organic electronics [59] to military applications. For the latter field, energetic materials performance and sensitivity go in parallel, so in order to meet the requirements of insensitive high energy explosives for modern weapon applications [60], co-crystallization is a very promising approach that is worth to develop as it is clearly stated by the number of papers published in the last years [61–68].

Thus, this technique offers an improvement upon existing materials because it is proved that co-crystals are thermodynamically more stable than their pristine compounds [69]. Different studies have shown that using this approach tuning key properties including density, melting point, sensitivity, and detonation performance is feasible.

At ISL, French-German Research Institute of Saint-Louis, the Spray Flash Evaporation (SFE) process [54, 70, 71] was initially designed to elaborate nanoexplosives [72]. Using this process Spitzer et al. have produced different types of mixtures such as entirely crystalline composites, semi-crystalline mixtures and sub-micron and nano-sized co-crystals depending on the type of molecular interaction between the initial compounds.

1.6 Detection of explosives: main challenges

In the last years, the growing risk of terrorist attacks has become an issue of capital importance for national security agencies all over the world, especially in public places with a high density of persons (i.e. airports, train stations, etc.). An early detection of some targets can give an indication that something risky has been found and can lead to the security staff to take the necessary steps to assure everyone's life. That is the reason why detection can be considered as one of the unsolved technological milestones of the XXI century [73].

Some other areas can also take advantage of proper detection systems as forensic analysis, global de-mining projects and environmental care [74]. It is well-known that even traces as low as 0.002 ppm of some energetic materials as TNT [75] can cause serious diseases, even deaths [76]. These are the main reasons why a high accuracy, fast and affordable explosive detection method is needed. But, unfortunately there is no golden stone for the moment.

The reason why explosives are extremely difficult to identify using most of the current detection techniques is due to their extremely low vapor pressures at room temperature (cf. Figure 1.20) [77]. Although explosives manufacturers add high volatile substances during the fabrication process, the so-called "taggants", as 2,3-dimethyl-2,3-dinitrobutane, o-nitrotoluene, to facilitate the detection [78], the terrorist's inventiveness has to be taken into account because normally they use to hide explosive among many different materials, the so-called "interferents". The effective vapor pressure can be reduced three orders of magnitude by wrapping or packaging them, in plastics for example [79].

During the last 10 years, a great advance in real time detection of explosives have been done, but it is not even enough. The issue is still a challenge for researchers all over the world who put all their efforts to improve current technologies as well as trying to develop new detection methods [81].

The requirements of the ideal detection method should include at least the following characteristics:

- high sensitivity,

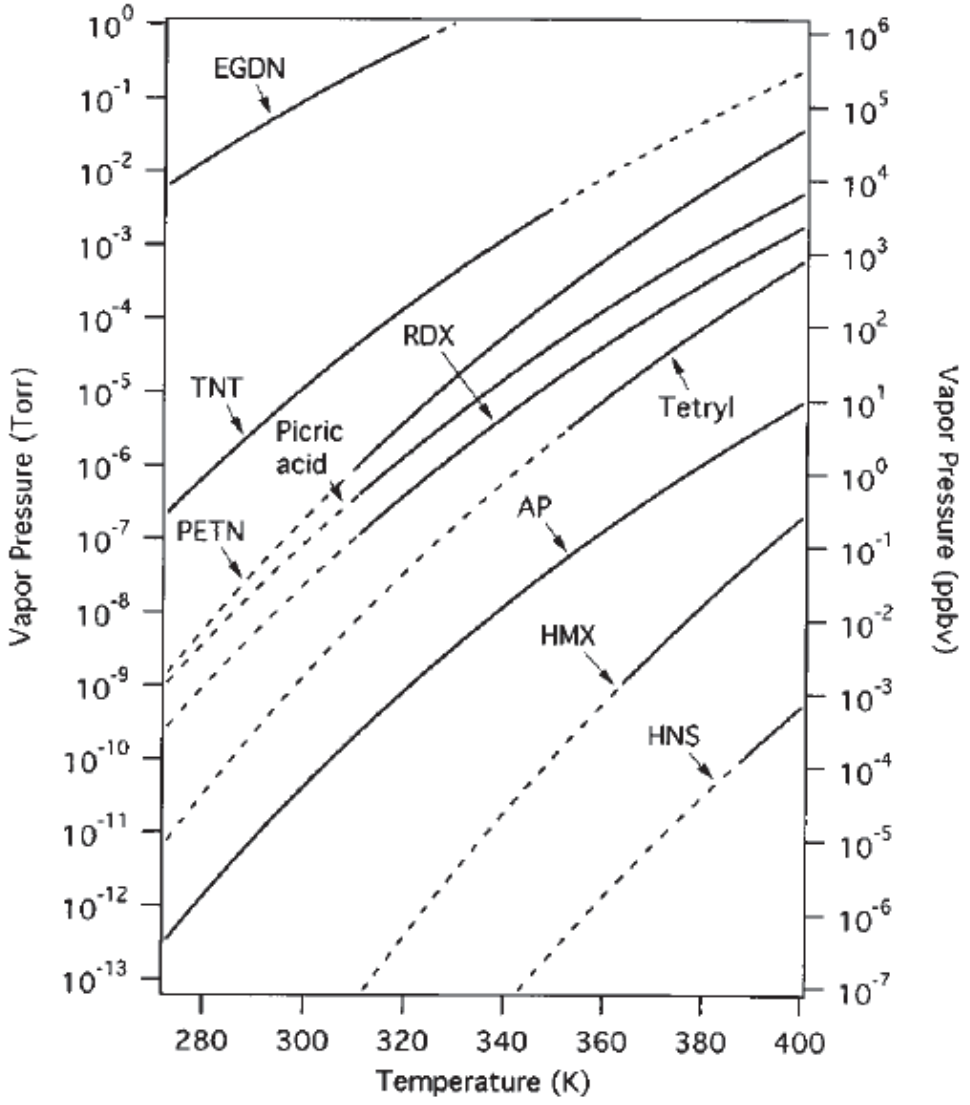

Figure 1.20 – Vapor pressure of several common explosives as a function of temperature. With solid lines are displayed approximate measured regions whereas in dashed lines are shown extrapolations [80].

- applicability to non-volatile and thermally unstable samples,
- high specificity and selectivity,
- rapid response times,
- no needing of sample preparation or handling,
- easy to operate and low cost sensors,
- low false alarms.

Unfortunately, nowadays none of the currently available methods meet all these criteria.

Classifications

The literature published on such a human-life concerning issue as the explosive detection is vast and extensive. Thus, different ways to classify the detection methods can be found.

J.S. Caygill et al. [82] make a global classification in detection of hidden explosives. According to these authors, areas that have to be covered in detection of explosives can be listed as follows:

- bulk detection,
- trace detection,
- vapors detection,
- stand-off detection.

Concerning the techniques used to achieve this purpose, the following classification gives a general and a clear idea:

- **Spectroscopic techniques**. The basic idea is to separate ions according to their mass/charge ratio by electrical and magnetic fields. Before separation, samples should be ionized in a mass spectrometer.

These methods provide detection and quantification with high sensitivity and selectivity. The principal drawbacks are the high costs and the requirements of relatively complex laboratory equipment, although a lot of work is being addressed to reduce both size and costs.

Within this category, there are several techniques making use of spectroscopy methods:

– Ion mobility spectroscopy (IMS) [83]. The sample is introduced into the gas-phase of the spectrometer where an electric field is applied in order to ionize it. The ionized vapors are guided to a drift region where the sample identification is made by its mass/charge ratio, comparing drift times of sample with known standards (cf. Figure 1.21).

  This technique is widely used in routine analysis due to both quantitative and qualitative characterization possibilities and the low detection limits that it can achieve. However, the ionization sources used by the available devices (^{63}Ni and ^{241}Am) [84] are radio-actives, therefore safety and environmental factors have to be taken into account.

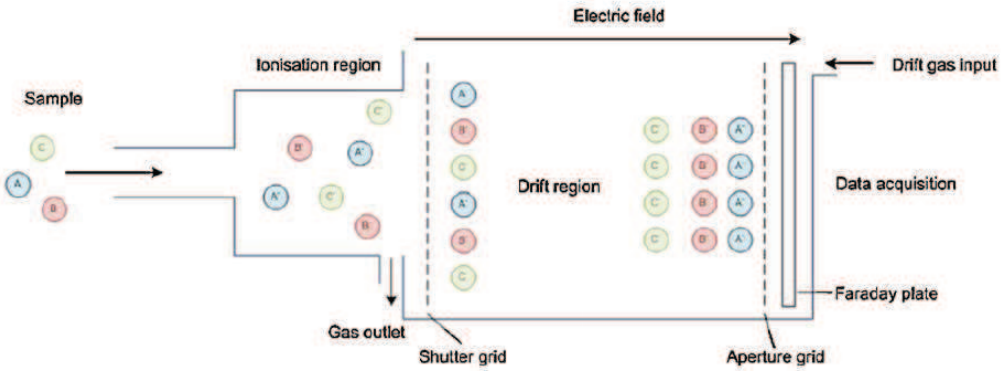

Figure 1.21 – Ion Mobility Spectrometer scheme [82].

– Terahertz spectroscopy (THzS) [85]. This non-ionizing radiation, its wavelength lies in the far infrared between 0.1–10 THz, can be

used to detect hidden explosives in clothing and common packing materials from their characteristics THz spectra.

Based on differential absorption, the analyte is irradiated with at least two different frequencies of THz radiation producing an excitation on the vibrational modes of molecules (cf. Figure 1.22). Thus, different explosives give the so-called "fingerprint", a unique THz spectrum, which can be used to discriminate between them using this Terahertz spectral imaging technique [86, 87]. The threshold of this technique is in the order

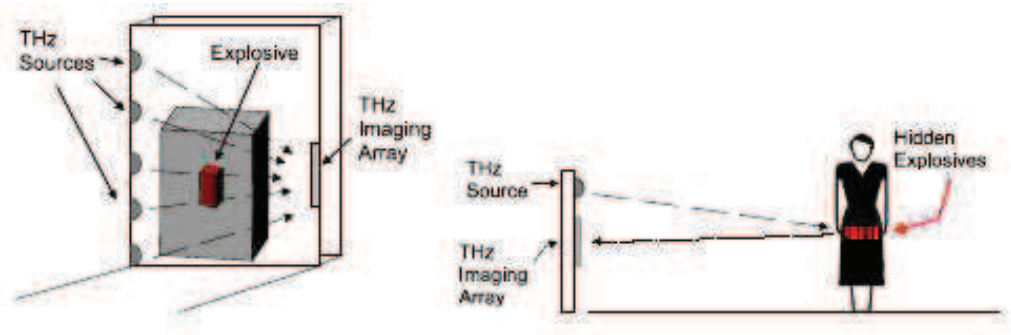

Figure 1.22 – TeraHertz imaging illustration [88].

– Laser-induced breakdown spectroscopy (LIBS) [89]. This technique uses a short laser pulse of high intensity to vaporize the sample, generating a small plasma plume. The excited ions emit light that enables the characterization of the sample. Each element has a unique spectral signature which allows to discriminate between them.

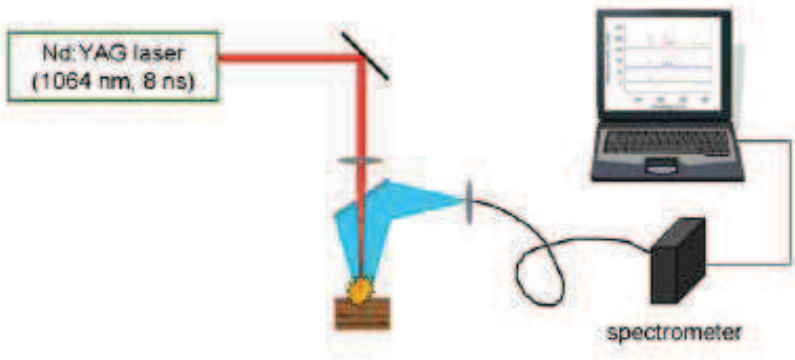

Figure 1.23 – Scheme of a Laser-Induced Breakdown Spectroscopy system [89].

LIBS has some advantages as a detection technique such as no need for sample preparation, very high sensitivity (nanograms-picograms produce an useful spectrum), real time measurements (less than 1 s) and possibility to be use as a stand-off detection system. However, LIBS gives the elemental composition of the sample and could be confusing when compounds with the same chemical composition, i.e. polymers and explosives, are analysed. Another drawback is the interference that oxygen and nitrogen in the atmosphere can cause with the ratios of oxygen and nitrogen relative to carbon and hydrogen when the technique is use as a stand-off detection method in open air [90].

– Raman spectroscopy (RS). Raman is an instantaneous process where some energy is lost to (or gained from) the target molecule when it is irradiated with monochromatic radiation. This difference corresponds to an energy shift in the molecule measured as vibrational transitions of scattered photons. The resulting spectrum gives the fingerprint of the sample that uniquely identifies the substance. Advantages of RS are almost real time measurements, no need for sample preparation and possibility of stand-off detection [91]. But sensitivity is not a strong point of this technique, unless Surface Enhanced Raman Spectrocopy (SERS) is used. It makes use of near-infra red lasers to reduce the fluorescence that

is an issue when acquiring Raman spectra.

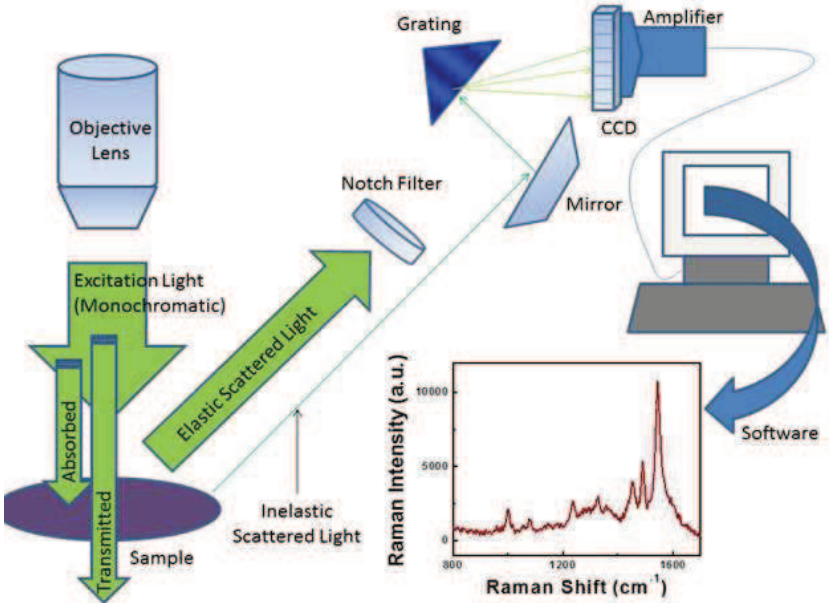

Figure 1.24 – Schematic for process involved in collecting Raman spectra [92].

- **Desorption ElectroSpray Ionization** (DESI). One promising method uses the DESI technique which is based on the interaction of charged particles generated by assisted electrospray with the target molecules present on almost any surfaces (metal, plastic, paper, polymer). It combines the advantages of sensitivity and specificity of mass spectrometry methods with fast responses, no sample preparation and in-situ detection on any surface [93, 94].

- **Sensors**. Nowadays, sensors are one of the most promising methods of detection underneath the most reliable method nowadays, the canine's smell. due to the low cost, portability and specificity, although there are also some drawbacks as sensitivity, reliability and reproducibility. Many groups are working on the improvement of these issues.

  explosives [95]. They can be classified as:

  A classification based on the physical principles and operating mechanisms of sensors used for the detection of explosives can be made.

– Olfactory type. The distinction can be made according to the nature of the sensor itself, either natural or artificial.

  * Animals. Currently, sniffer dogs are the most reliable "devices" on explosives detection. They are fast, directional and provide analysis in real-time [82]. But the effective cost of using these dogs is relatively high. Their efficacy declines over time and after extensive fieldwork. For example, in real scenarios, dogs become tired after around one hour of working, so the use of two or more dogs at each location is inevitable, multiplying the costs [96, 97].
    Some other animals like rats [98] and insects [99] have been used due to their discriminatory olfactory systems.

  * Electronic noses. Within this category are included a bunch of chemical sensors that can interact with vapors in different ways depending on the nature and concentration of these vapors. After that interaction, a pattern recognition unit determinates the analyte giving its concentration. Brudzewski et al. have developed a sensor array capable to detect RDX, PETN and TNT vapors at the ppm level [100].

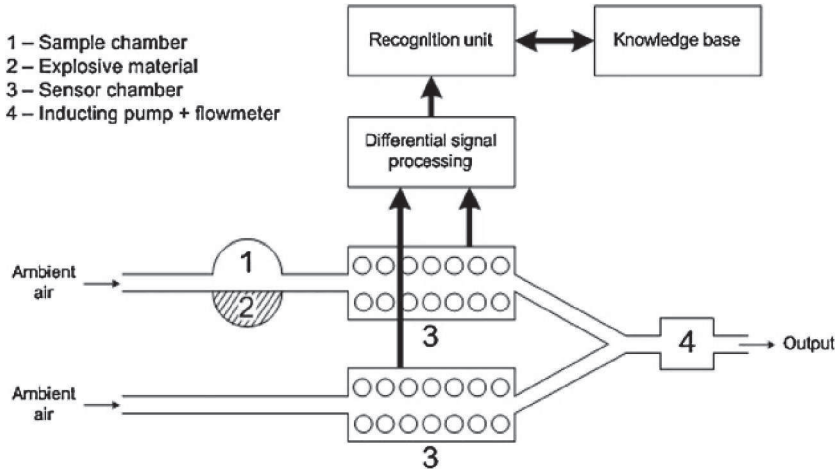

Figure 1.25 – Scheme of an electronic nose used for recognition of explosive materials [100].

In addition, due to the miniaturization of devices like mass spectrometers, gas chromatographs or ion mobility spectrometers, they can also be classified as electronic noses because they share the same functioning principle and they can detect and identify extremely low vapor concentration [101].

- Biosensors: Within this definition are analytical devices using a biological element attached to a solid-state surface. These devices enable a reversible and specific interaction with the target analyte.The principal advantage of biosensors is their high specificity for their target compounds. Examples of successful employment of biosensors use proteins [102] or enzymes [103]. An extended review for this kind of sensors can be found in the review paper of Smith et al [104].

- Chemical type. These sensors detect the products of a chemical reaction in which explosives are implied. Detection of these products implies changes in some of the physical properties on the products, i.e. colour, conductivity, etc.

  Two available commercial products using this approach are the detection kits Expray ®and DropEx ® [105] (cf. Figure 1.26).

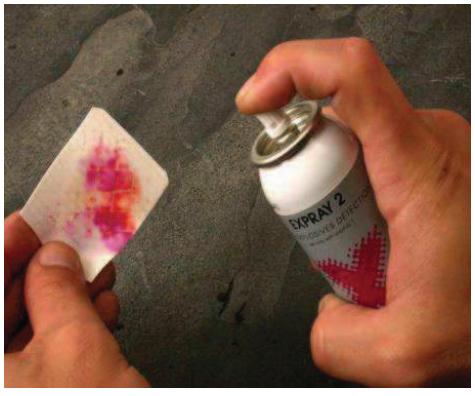

(a) Identification of explosives using the EXPRAY Detection Kit.

(b) Explosives Detection Field Test Kit.

Figure 1.26 – Commercial products for explosives detection based on chemical reactions.

- Electrochemical type: Into this group are included all sensors capable to detect changes produced when an electric current passes through the sensor electrodes and causes changes on the signal due to the electrode's interaction with the explosives, which are chemically modified or degradated. According to this approach, they can be classified as [95]:

  * potentiometric when the voltage is measured,
  * amperometric if the current is measured,
  * conductometric when the conductivity is measured.

  These kind of sensors need a mobile electrolyte in order to keep the charge balance. All nitro aromatics explosives, due to their redox properties, make them ideal candidates for this type of sensors.

  Advantages of these sensors are the specificity given by the electrodes, in the ppt (parts per trillion) range, reported by Gwenin and coworkers [106].They are also fast, cheap and ideal for miniaturization [107]. However, some drawbacks are their requirement of a mobile electrolyte and limited sensitivity. Conducting polymer coatings, like poly(3,4-dioxyethylene thiophene)(PEDOT) [108] can get over the mobile electrolyte issue at the expense of introducing more complexity to the sensor.

- MEMS-type sensors: These sensors take advantage of the existing semiconductors technology. Samples provoke bending or changing in the shape when their surface interact with them (microcantilever sensors) or change the heat capacity during the heating and cooling ramps applied (micro/nanocalorimetric sensors). Within this latter group is where we can allocate our system.

  * Micro-cantilever devices: The approach for the detection is based on the adsorption of explosives onto the sensor surface.

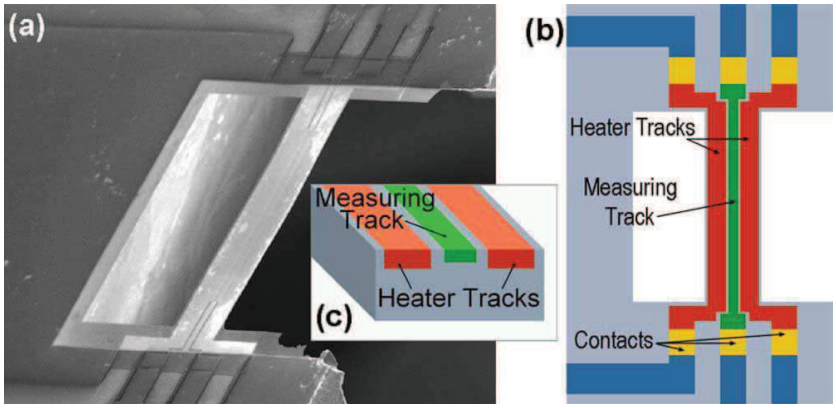

Figure 1.27 – Microfabricated silicon bridge structure [109].

The micro-cantilever is normally functionalized with a coating of materials, from self-assembled polymeric monolayers to nanostructured porous zeolites [78, 110–113], with high affinity for explosives. This bind between the explosive and the coating provokes the bending on the cantilever which is measured with a laser-photodiode using the same principle as in the atomic force microscopes.

The advantages of micro-cantilever sensors is the high surface-to-volume ratio that they can achieve.

Most of the papers using micro-cantilevers to detect explosives have in common the use of an explosive vapor generator [114]. Within this section, systems based on microfabricated bridges are included [109, 115]. They used a micro-cantilever positioned in a suspended bridge, both in the same plane (cf. Figure 1.27).

Another approach was developed by Spitzer et al. [116]. They tried to mimic the mechanism used by the Bombyx Mori, a silkmoth, for the identification of pheromones to detect single molecules of explosive vapors. With this idea in mind, they functionalized cantilevers achieving a LOD for TNT vapors in the sub-ppt range (cf. Figure 1.28).

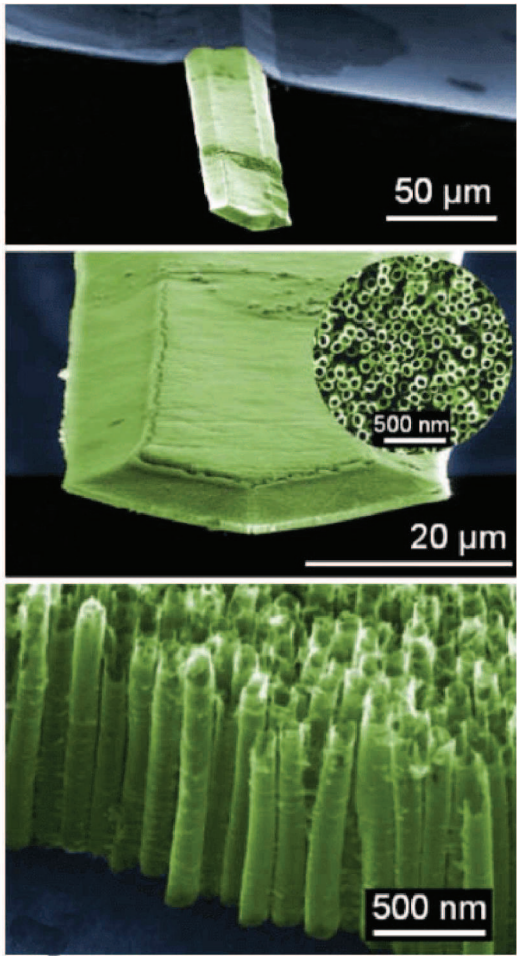

Figure 1.28 – Nanostructured microcantilever covered by TiO_2 nanotubes [116].

Studies of functionalized microcantilevers detecting TNT and o-nitrotoluene, respectively were also developed by Pinnaduwage et al. [110] and Urbiztondo et al. [117].

* Calorimetric devices: They state that the explosion potential of energetic materials can be measured from their thermal analysis profiles [118]. All these devices use MEMS technology which is vastly used in the semiconductor industry.
Currently, only a few micro/nanocalorimeter devices have been used for explosives detection.

Liu et al. [40] developed a prototype capable to analyze solid and liquid samples in the range of nanogram and nanoliters, respectively (cf. Figure 1.29).

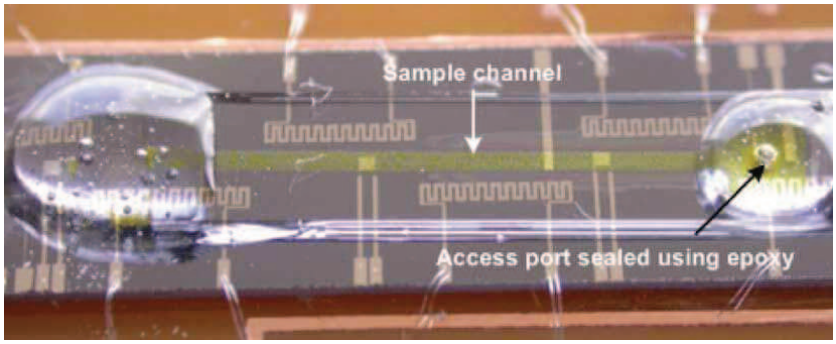

Figure 1.29 – Nanocalorimeter prototype loaded with a sample of ammonium iron (III) sulphate dodecahydrate [119].

They claim that explosives samples were successfully characterized using its prototype but they do not show any curve on their papers (only an acetone curve is shown).
Zuck et al. [39] used MEMS-based technology to perform differential scanning microcalorimetry at high heating rates (cf. Figure 1.30).

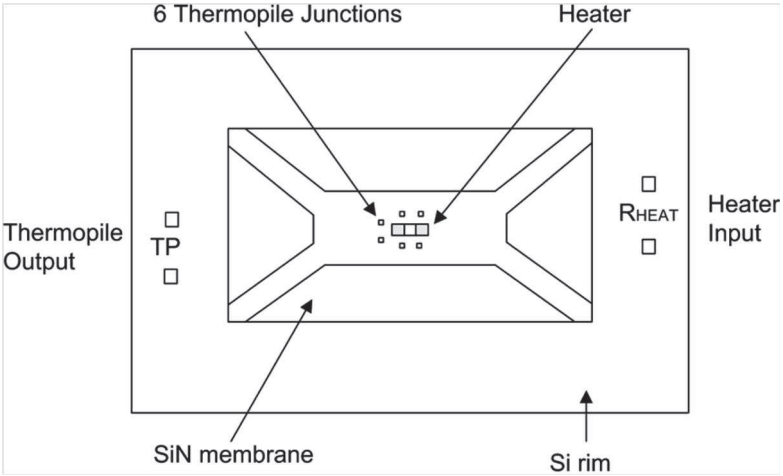

Figure 1.30 – Scheme of the microcalorimetric sensor [39].

The results shown in this paper are not consistent with the

data found in the literature, concerning the melting and decomposition temperatures of explosives.
Greeve et al. [118] used a micro-calorimetric sensor with an optimized temperature uniformity in order to detect traces of explosives. Future work will show measurements with real explosives.

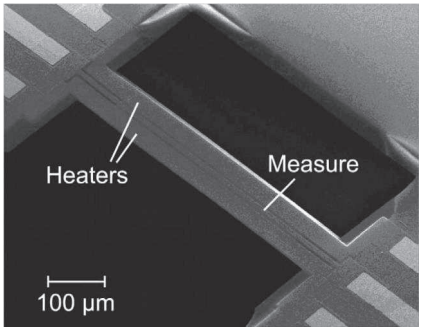

Figure 1.31 – SEM picture of the microcalorimetric sensor developed by Greeve et al. [118].

The paper written by Piazzon et al. [1] using Nanocalorimetry in the field of explosives detection shows measurements performed with micron-sized particles of explosives. This is the starting point of the work developed in this manuscript.

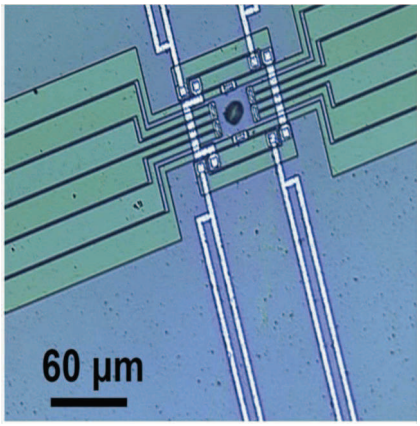

Figure 1.32 – RDX micron-sized crystal on a nanocalorimetric sensor [1].

- **Nanotechnology**

Nanotechnology is currently an area of expanding research due to the behavior showed by materials when they are in nano-size range compared to bulk materials.

– Polymers. Functional monomers can interact with the analyte of interest forming both covalent and non-covalent bondings [120]. Into this category, one can find the so-called MIPs (Molecularly Imprinted Polymers), which are formed when the monomers are cross-linked around a template (cf. Figure 1.33). MIPs allow the formation of molecules with recognition sites specific for a target analyte.

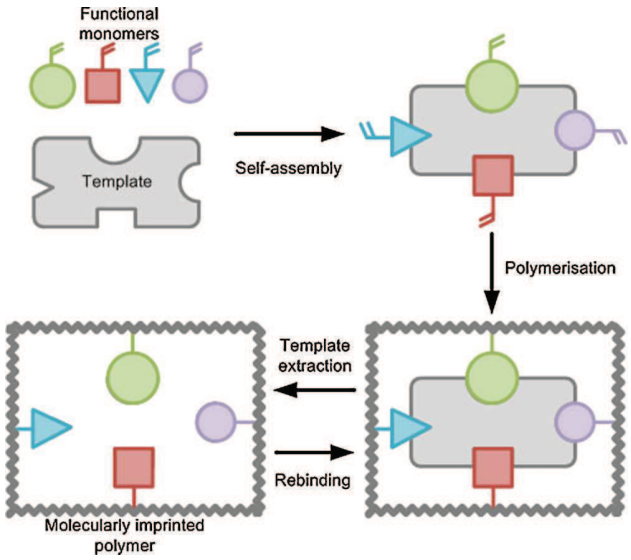

Figure 1.33 – Schematic of the development of a MIP [82].

– Semiconducting organic polymers. This approach takes into account the ability to transport optical excitations over large distances of these organic semiconducting polymers, which can be described as wide-band-gap semiconductors. With this idea in mind, Swager and coworkers developed a method to produce thin films of organic semiconductors with improved recognition of explosives [121].

Fido ®devices are based on this technology [122].

1.7 General conclusions

Nowadays, none of the devices on the market nor on research laboratories meet all the requirements of an ideal detection system in terms of sensitivity, specificity, response times, easy of use and price. Therefore, the idea of establishing a new method for detection of explosive particles and for characterization using a single particle is particularly challenging. My modest contribution and the driving force of the work described in this manuscript is an attempt to achieve these goals.

To perform an experiment using a single particle of an energetic material is quite advantageous, particularly in terms of security. Such materials, even in quantities in the range of milligrams, can undergo a very violent reaction during heating if enough precautions are not considered. That possibility is eliminated using just a single particle to perform the analysis using Nanocalorimetry. Moreover, the study of energetic co-crystals can enhance the possibilities of the technique because they allow to a better understanding the behavior of pristine compounds (e.g. CL-20) giving information that otherwise could not be obtain (e.g. crystallization rates).

In terms of characterization, the freedom given by setup of the nanocalorimeter used on this work permit to combine this technique with others such as X-ray scattering using a Synchrotron source to perform in-situ measurements of thermal behavior and structural analysis of different materials.

[1] N. Piazzon, M. Rosenthal, A. Bondar, D. Spitzer, D. Ivanov, *Journal of Physics and Chemistry of Solids* **2010**, *71*, 114–118.

[2] N. Piazzon, PhD thesis, Université de Haute Alsace, Mulhouse, **2010**.

[3] D. Fenby et al., *Pure Appl Chem* **1987**, *59*, 91–100.

[4] M. Brown, P. Gallagher, *Handbook of thermal analysis and calorimetry: Recent advances, techniques and applications*, *Vol. 5*, Elsevier, **2011**.

[5] ICTAC, Online; accesed 01-24-2015.

[6] O. Sĝrensen, J. Rouquerol, *Sample Controlled Thermal Analysis: Origin, Goals, Multiple Forms, Applications and Future*, *Vol. 3*, Springer, **2003**.

[7] G. Stewart, *Review of Scientific Instruments* **1983**, *54*, 1–11.

[8] J. Lerchner, *Thermochimica Acta* **1999**, *337*, 231.

[9] W. Hemminger, G. Höhne, Y. Goldman, *Calorimetry: fundamentals and practice*, Verlag Chemie Weinheim, **1984**.

[10] Slovenská Technická Univerzita. Fakulta Chemickej a Potravinárskej Technológie, Online; accesed 21-01-2015.

[11] V. Glazov, A. Pashinkin, M. Mikhailova, *Scandinavian journal of metallurgy* **2001**, *30*, 388–390.

[12] K. Ramakumar, M. Saxena, S. Deb, *Journal of Thermal Analysis and Calorimetry* **2001**, *66*, 387–397.

[13] O. Corbino, *Phys. Z* **1910**, *11*, 413–417.

[14] M. Efremov, E. Olson, M. Zhang, F. Schiettekatte, Z. Zhang, L. Allen, *Review of scientific instruments* **2004**, *75*, 179–191.

[15] M. Zhang, M. Efremov, F. Schiettekatte, E. Olson, A. Kwan, S. Lai, T. Wisleder, J. Greene, L. Allen, *Physical Review B* **2000**, *62*, 10548.

[16] M. Zhang, M. Efremov, E. Olson, Z. Zhang, L. Allen, *Applied Physics Letters* **2002**, *81*, 3801–3803.

[17] A. Kwan, M. Efremov, E. Olson, F. Schiettekatte, M. Zhang, P. Geil, L. Allen, *Journal of Polymer Science Part B: Polymer Physics* **2001**, *39*, 1237–1245.

[18] S. Adamovsky, A. Minakov, C. Schick, *Thermochimica Acta* **2003**, *403*, 55–63.

[19] K. Xiao, J. Gregoire, P. McCluskey, D. Dale, J. Vlassak, *Journal of Applied Physics* **2013**, *113*, 243501.

[20] M. Rosenthal, D. Doblas, J. Hernandez, Y. Odarchenko, M. Burghammer, E. Di Cola, D. Spitzer, A. Antipov, L. Aldoshin, D. Ivanov, *Journal of synchrotron radiation* **2013**, *21*, 223–228.

[21] P. McCluskey, K. Xiao, J. Gregoire, D. Dale, J. Vlassak, *Thermochimica Acta* **2014**.

[22] C. Riekel, E. Di Cola, M. Reynolds, M. Burghammer, M. Rosenthal, D. Doblas, D. Ivanov, *Langmuir* **2015**.
[23] J. Zhang, Y. Zhao, *Nature* **2004**, *430*, 332–335.
[24] J. Jones, S. Barenberg, P. Geil, *Polymer* **1979**, *20*, 903–916.
[25] A. Abramov, N. Deryagin, D. Tret'yakov, *Semiconductor science and technology* **1996**, *11*, 607.
[26] A. Minakov, C. Schick, *Review of Scientific Instruments* **2007**, *78*, 073902–073902.
[27] L. Allen, G. Ramanath, S. Lai, Z. Ma, S. Lee, D. Allman, K. Fuchs, *Applied physics letters* **1994**, *64*, 417–419.
[28] S. Lai, J. Guo, V. Petrova, G. Ramanath, L. Allen, *Physical Review Letters* **1996**, *77*, 99.
[29] E. Olson, M. Efremov, M. Zhang, Z. Zhang, L. Allen, *Microelectromechanical Systems Journal of* **2003**, *12*, 355–364.
[30] P. McCluskey, J. Vlassak, *Journal of Materials Research* **2010**, *25*, 2086–2100.
[31] A. Lopeandia, J. Rodriguez-Viejo, *Thermochimica Acta* **2007**, *461*, 82–87.
[32] Xensor Integration, Online; accesed 04-15-2015.
[33] D. Denlinger, E. Abarra, K. Allen, P. Rooney, M. Messer, S. Watson, F. Hellman, *Review of Scientific Instruments* **1994**, *65*, 946–959.
[34] E. Zhuravlev, C. Schick, *Thermochimica Acta* **2010**, *505*, 1–13.
[35] M. Efremov, E. Olson, M. Zhang, S. Lai, F. Schiettekatte, Z. Zhang, L. Allen, *Thermochimica Acta* **2004**, *412*, 13–23.
[36] A. Minakov, S. Adamovsky, C. Schick, *Thermochimica Acta* **2005**, *432*, 177–185.
[37] A. Minakov, A. Van Herwaarden, W. Wien, A. Wurm, C. Schick, *Thermochimica Acta* **2007**, *461*, 96–106.
[38] V. Mathot, M. Pyda, T. Pijpers, G. Poel, E. Van de Kerkhof, S. Van Herwaarden, F. Van Herwaarden, A. Leenaers, *Thermochimica Acta* **2011**, *522*, 36–45.
[39] A. Zuck, J. Greenblatt, A. Zifman, A. Zaltsman, S. Kendler, G. Frishman, S. Meltzer, I. Fisher, *Journal of Energetic Materials* **2008**, *26*, 163–180.
[40] Y. Liu, V. Ugaz, S. North, W. Rogers, M. Mannan, *Journal of hazardous materials* **2007**, *142*, 662–668.
[41] W. W. Bannister, C.-C. Chen, W. A. Curby, E. B. Chen, P. L. Damour, A. Morales, Thermal analysis for detection and identification of explosives and other controlled substances, US Patent 6,406,918, **June 18, 2002**.

[42] J. Gregoire, K. Xiao, P. McCluskey, D. Dale, G. Cuddalorepatta, J. Vlassak, *Applied physics letters* **2013**, *102*, 201902.
[43] J. Gregoire, P. McCluskey, D. Dale, S. Ding, J. Schroers, J. Vlassak, *Scripta Materialia* **2012**, *66*, 178–181.
[44] M. Grapes, T. LaGrange, L. Friedman, B. Reed, G. Campbell, T. Weihs, D. LaVan, *Review of Scientific Instruments* **2014**, *85*, 084902.
[45] M. Grapes, T. LaGrange, K. Woll, B. Reed, G. Campbell, D. LaVan, T. Weihs, *APL Materials* **2014**, *2*, 116102.
[46] M. van Drongelen, T. Meijer-Vissers, D. Cavallo, G. Portale, G. V. Poel, R. Androsch, *Thermochimica Acta* **2013**, *563*, 33–37.
[47] W. Donald, R. Leib, J. O'Brien, A. Holm, E. Williams, *Proceedings of the National Academy of Sciences* **2008**, *105*, 18102–18107.
[48] H. Czerski, PhD thesis, University of Cambridge, **2006**.
[49] J. Agrawal, *High energy materials: propellants, explosives and pyrotechnics*, John Wiley & Sons, **2010**.
[50] R. Meyer, A. Homburg, *Explosives*, John Wiley & Sons, **2007**.
[51] J. Akhavan, *The Chemistry of Explosives*, The Royal Society of Chemistry, TJ International Ltd, Padstow, Cornwall, UK, **2004**.
[52] J. Field, *Accounts of chemical Research* **1992**, *25*, 489–496.
[53] C. Tarver, S. Chidester, A. Nichols, *The Journal of Physical Chemistry* **1996**, *100*, 5794–5799.
[54] B. Risse, PhD thesis, Université de Lorraine, **2012**.
[55] A. Bond, *CrystEngComm* **2007**, *9*, 833–834.
[56] N. Qiao, M. Li, W. Schlindwein, N. Malek, A. Davies, G. Trappitt, *International Journal of pharmaceutics* **2011**, *419*, 1–11.
[57] E. Choi, M. Jazbinsek, S. Lee, P. Günter, H. Yun, S. Lee, O. Kwon, *CrystEngComm* **2012**, *14*, 4306–4311.
[58] A. S. Tayi, A. Shveyd, A.-H. Sue, J. Szarko, B. Rolczynski, D. Cao, T. Kennedy, A. Sarjeant, C. Stern, W. Paxton, et al., *Nature* **2012**, *488*, 485–489.
[59] L. Zhu, Y. Yi, Y. Li, E. Kim, V. Coropceanu, J. Brédas, *Journal of the American Chemical Society* **2012**, *134*, 2340–2347.
[60] A. Sikder, N. Sikder, *Journal of hazardous materials* **2004**, *112*, 1–15.
[61] K. Landenberger, A. Matzger, *Crystal Growth & Design* **2010**, *10*, 5341–5347.
[62] O. Bolton, A. Matzger, *Angewandte Chemie International Edition* **2011**, *50*, 8960–8963.
[63] O. Bolton, L. Simke, P. Pagoria, A. Matzger, *Crystal Growth & Design* **2012**, *12*, 4311–4314.
[64] H. Li, Y. Shu, S. Gao, L. Chen, Q. Ma, X. Ju, *Journal of molecular modeling* **2013**, *19*, 4909–4917.

[65] K. Landenberger, O. Bolton, A. Matzger, *Angewandte Chemie International Edition* **2013**, *52*, 6468–6471.
[66] D. Spitzer, B. Risse, F. Schnell, V. Pichot, M. Klaumünzer, M. Schaefer, *Scientific reports* **2014**, *4*.
[67] Z. Yang, Q. Zeng, X. Zhou, Q. Zhang, F. Nie, H. Huang, H. Li, *RSC Advances* **2014**, *4*, 65121–65126.
[68] Y. Wang, Z. Yang, H. Li, X. Zhou, Q. Zhang, J. Wang, Y. Liu, *Propellants Explosives Pyrotechnics* **2014**, *39*, 590–596.
[69] Y. Gao, H. Zu, J. Zhang, *Journal of Pharmacy and Pharmacology* **2011**, *63*, 483–490.
[70] D. Spitzer, V. Pichot, B. RISSE, Method for manufacturing nanoparticles by detonation, WO Patent App. PCT/EP2013/054,107, **Sept. 2013**.
[71] B. Risse, D. Hassler, D. Spitzer, Preparation of nanoparticles by flash evaporation, WO Patent App. PCT/EP2013/052,478, **Aug. 2013**.
[72] B. Risse, D. Spitzer, D. Hassler, F. Schnell, M. Comet, V. Pichot, H. Muhr, *Chemical Engineering Journal* **2012**, *203*, 158–165.
[73] R. Woodfin, *Trace chemical sensing of explosives*, John Wiley & Sons, **2006**.
[74] G. Asbury, J. Klasmeier, J. H. Hill, *Talanta* **2000**, *50*, 1291–1298.
[75] U. S. E. P. Agency, Technical Fact Sheet - TNT, tech. rep. EPA505-F-11-011, Office of Solid Waste and Emergency Response, **May 2012**.
[76] W. McConnell, R. Flinn, *The Journal of industrial hygiene and toxicology* **1946**, *28*, 76.
[77] B. Dionne, D. Rounbehler, E. Achter, J. Hobbs, D. Fine, *Journal of Energetic Materials* **1986**, *4*, 447–472.
[78] I. Pellejero, M. Miana, M. Pina in Anales de la Real Sociedad Española de Química, Real Sociedad Española de Química, **2013**, pp. 97–105.
[79] P. Kolla, *Angewandte Chemie International Edition* **1997**, *36*, 800–811.
[80] D. Moore, *Review of Scientific Instruments* **2004**, *75*, 2499–2512.
[81] J. Yinon, *Handbook of Analytical Separations* **2008**, *6*, 823–838.
[82] J. Caygill, F. Davis, S. Higson, *Talanta* **2012**, *88*, 14–29.
[83] R. Ewing, D. Atkinson, G. Eiceman, G. Ewing, *Talanta* **2001**, *54*, 515–529.
[84] R. Ewing, M. Waltman, *International Journal for Ion Mobility Spectrometry* **2009**, *12*, 65–72.
[85] M. Kemp, P. Taday, B. Cole, J. Cluff, A. Fitzgerald, W. Tribe in AeroSense 2003, International Society for Optics and Photonics, **2003**, pp. 44–52.

[86] J. Chen, Y. Chen, H. Zhao, G. Bastiaans, X. Zhang, *Optics Express* **2007**, *15*, 12060–12067.
[87] Y. Shen, T. Lo, P. Taday, B. Cole, W. Tribe, M. Kemp, *Applied Physics Letters* **2005**, *86*, 241116–241116.
[88] J. Federici, B. Schulkin, F. Huang, D. Gary, R. Barat, F. Oliveira, D. Zimdars, *Semiconductor Science and Technology* **2005**, *20*, S266.
[89] J. Gottfried, J. F. D. Lucia, C. Munson, A. Miziolek, *Analytical and Bioanalytical Chemistry* **2009**, *395*, 283–300.
[90] P. Lucena, A. Dona, L. Tobaria, J. Laserna, *Spectrochimica Acta Part B: Atomic Spectroscopy* **2011**, *66*, 12–20.
[91] E. Izake, *Forensic science international* **2010**, *202*, 1–8.
[92] The Prashant Kamat Laboratory. University of Notre Dame, Online; accesed 25-03-2014.
[93] R. Cooks et al., *Chemical communications* **2005**, 1950–1952.
[94] I. Cotte-Rodríguez, Z. Takáts, N. Talaty, H. Chen, R. Cooks, *Analytical chemistry* **2005**, *77*, 6755–6764.
[95] S. Singh, *Journal of Hazardous Materials* **2007**, *144*, 15–28.
[96] K. Furton, L. Myers, *Talanta* **2001**, *54*, 487–500.
[97] R. Harper, J. Almirall, K. Furton, *Talanta* **2005**, *67*, 313–327.
[98] J. Otto, M. Brown, W. Long, *Applied Animal Behaviour Science* **2002**, *77*, 217–232.
[99] B. Marshall, C. Warr, M. de Bruyne, *Chemical senses* **2010**, *35*, 613–625.
[100] K. Brudzewski, S. Osowski, W. Pawlowski, *Sensors and Actuators B: Chemical* **2012**, *161*, 528–533.
[101] J. Yinon, *Analytical Chemistry* **2003**, *75*, 98–A.
[102] Z. Naal, J. Park, S. Bernhard, J. Shapleigh, C. Batt, H. Abruna, *Analytical chemistry* **2002**, *74*, 140–148.
[103] R. Freeman, I. Willner, *Nano letters* **2008**, *9*, 322–326.
[104] R. Smith, N. D'Souza, S. Nicklin, *Analyst* **2008**, *133*, 571–584.
[105] Expray, Online; accesed 08-15-2013.
[106] C. Gwenin, M. Kalaji, P. Williams, R. Jones in International Society of Electrochemistry 55th Annual Meeting, **2004**.
[107] P. Rabenecker, K. Pinkwart, *Propellants Explosives Pyrotechnics* **2009**, *34*, 274–279.
[108] A. Díaz Aguilar, E. Forzani, M. Leright, F. Tsow, A. Cagan, R. Iglesias, L. Nagahara, I. Amlani, R. Tsui, N. Tao, *Nano letters* **2009**, *10*, 380–384.
[109] D. Yi, A. Greve, J. Hales, L. Senesac, Z. Davis, D. Nicholson, A. Boisen, T. Thundat, *Applied Physics Letters* **2008**, *93*, 154102–154102.

[110] L. Pinnaduwage, A. Gehl, D. Hedden, G. Muralidharan, T. Thundat, R. Lareau, T. Sulchek, L. Manning, B. Rogers, M. Jones, et al., *Nature* **2003**, *425*, 474–474.

[111] L. Pinnaduwage, V. Boiadjiev, J. Hawk, T. Thundat, *Applied Physics Letters* **2003**, *83*, 1471–1473.

[112] L. Pinnaduwage, A. Wig, D. Hedden, A. Gehl, D. Yi, T. Thundat, R. Lareau, *Journal of Applied Physics* **2004**, *95*, 5871–5875.

[113] P. Datskos, N. Lavrik, M. Sepaniak, *Sensor Letters* **2003**, *1*, 25–32.

[114] J. Davies, R. Larson, L. Goodrich, H. Hall, B. Stoddard, S. Davis, T. Kaser, F. Conrad, Calibrated vapor generator source, US Patent 5,452,600, **Sept. 1995**.

[115] L. Senesac, D. Yi, A. Greve, J. Hales, Z. Davis, D. Nicholson, A. Boisen, T. Thundat, *Review of Scientific Instruments* **2009**, *80*, 035102–035102.

[116] D. Spitzer, T. Cottineau, N. Piazzon, S. Josset, F. Schnell, S. Pronkin, E. Savinova, V. Keller, *Angewandte Chemie International Edition* **2012**, *51*, 5334–5338.

[117] M. Urbiztondo, I. Pellejero, M. Villarroya, J. Sesé, M. Pina, I. Dufour, J. Santamaría, *Sensors and Actuators B: Chemical* **2009**, *137*, 608–616.

[118] A. Greve, J. Olsen, A. Boisen, N. Privorotskaya, W. King, L. Senesac, T. Thundat in Sensors, 2009 IEEE, IEEE, **2009**, pp. 723–726.

[119] Y. Liu, V. Ugaz, W. Rogers, M. Mannan, S. Saraf, *Journal of Loss Prevention in the Process Industries* **2005**, *18*, 139–144.

[120] A. McCluskey, C. Holdsworth, M. Bowyer, *Organic & biomolecular chemistry* **2007**, *5*, 3233–3244.

[121] T. Swager in *Electronic Noses & Sensors for the Detection of Explosives*, Springer, **2004**, pp. 29–37.

[122] Fido ® XT Explosives Detector, Online, accesed 08-15-2013.

Chapter 2

Materials and methods

In this chapter, the materials and main techniques used in this work are described. Both, direct-space techniques (e.g. Polarized Optical Microscopy) as well as reciprocal-space techniques (e.g. Wide-Angle X-ray scattering) which make use of the combination of the particular set-up provided by the nanocalorimeter are introduced. These techniques are complementary to Nanocalorimetry and are employed for a better understanding of the systems in question.

2.1 Materials

In this first part of the chapter, a description of the energetic materials used in this work will be given. The materials have been preliminarily characterized by Nuclear Magnetic Resonance and Raman Spectroscopy.

2.1.1 Octogen (HMX)

1, 3, 5, 7-tetranitro-1, 3, 5, 7-tetraaza-cyclooctane is the IUPAC name for HMX (also known as octogen). It was first synthesized in 1941 by W. E. Bachmann and J. Sheehan when they were trying to develop an easier way to synthesize RDX [1].

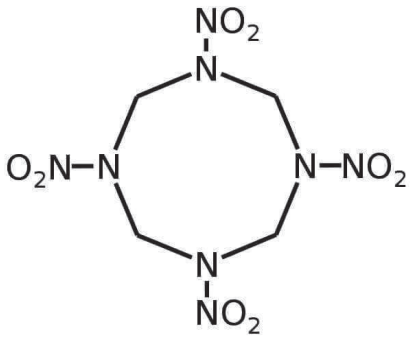

(a) Chemical formula of HMX.

(b) 3-D molecular model of HMX in the conformation corresponding to beta-phase.

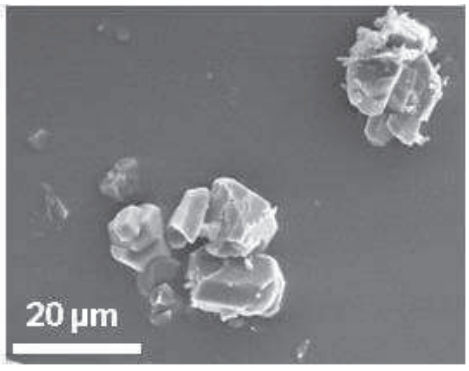

(c) SEM micrograph of HMX crystals.

Figure 2.1 – HMX: Chemical structure and crystal habit.

HMX is produced when hexamethylenetretamine, acetic anhydride, glacial acetic acid, nitric acid and ammonium nitrate are added in the same proportion and mixed in a batch reactor at 45 °C during 15 minutes [2]. The precipitate that contains 73 % of HMX and 27 % of RDX, which will be destroyed afterwards during purification.

$$(CH_2)_6N_4 + 4\,HNO_3 \longrightarrow (CH_2NNO_2)_4 + 2\,CH_2O + 2\,H_2O$$

Sample characterization was done by NMR and Raman. The operation parameters for the Varian MR 400 MHz solid-state NMR spectrometer were:

- Spectrometer Frequency: 399.685 MHz
- Temperature: 298.1 K
- Relaxation delay: 2.0 s
- Pulse: 45.0 deg
- Acquisition time: 1.861 s
- Width: 8802.8 Hz
- 32 repetitions per experiment

Samples of HMX used had a purity > 99.5 %. The resolution of the peak at 6.3 ppm shown in Figure 2.2 confirms this value.

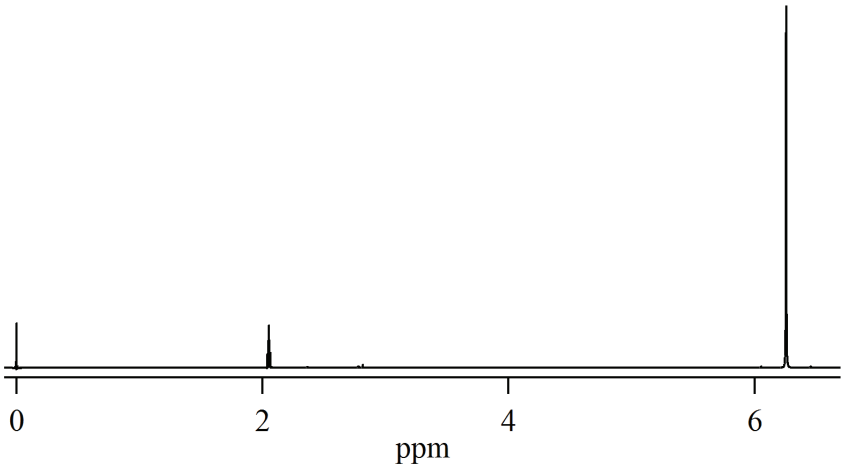

Figure 2.2 – ^{1}H NMR spectrum of HMX sample used in this work.

The configuration used for the inVia Raman microscope is detailed below:

- Laser wavelength: 633 nm
- Power: 10 %
- Exposure: 10 s
- Accumulations: 1

Figure 2.3 shows a Raman spectrum of the HMX crystals used in this work. The spectrum is in good agreement with literature data [3]. As it can be seen, between 830-950 cm^{-1} are the ring stretch vibrations, N–N stretch and symmetric N–O_2 stretch vibrations appear at 1230-1320 cm^{-1}, asymmetric N–O_2 stretch vibrations are at 1520-1580 cm^{-1} and the strong peaks at 2990-3040 cm^{-1} belong to the C–H stretch vibrations [4].

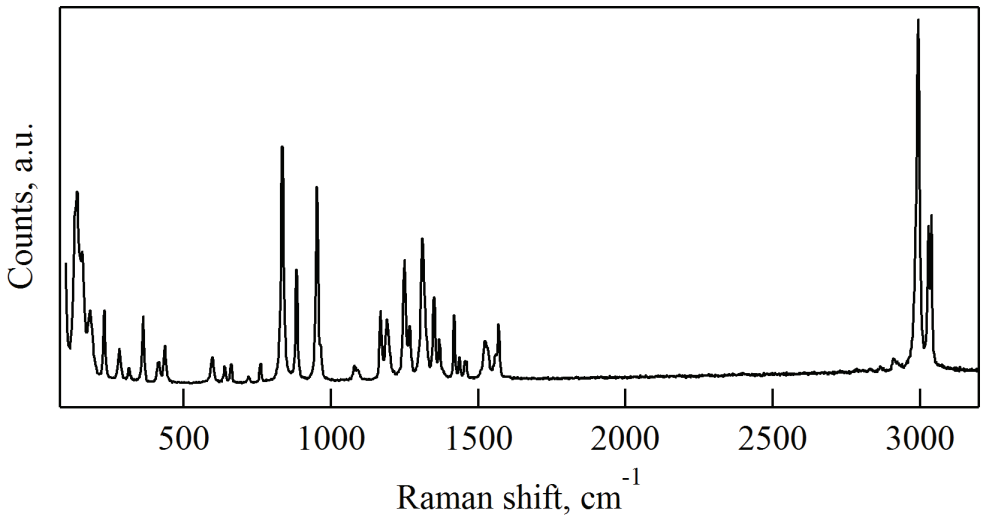

Figure 2.3 – Raman spectrum of the HMX sample used in this work.

Physical properties

HMX consists of alternating CH_2 and N–NO_2 groups in a non-planar eight-membered ring molecule as shown in Figure 2.1a. It forms colorless crystals with a maximum density of 1.96 g/cm^3. The crystals melt in-between 275 and 282 °C [5, 6]. Both HMX and RDX (cf. Figures 2.1a and 2.4a) are

very similar compounds sharing some physical properties, e.g., their melting points are close to their ignition temperatures [2]. The crystal structure of the stable form at room temperature, β-HMX, is monoclinic and its space group is $P2_1/c$ [6, 7].

McCrone [8] reported four different polymorphs of HMX at ambient pressure, but apparently there were only three, which are different [6]. These polymorphics structures are listed below:

- α-HMX is not a thermodynamically stable polymorph at room temperature, but it can be preserved indefinitely if the solvent and crystallization conditions are properly chosen.
- β-HMX is the thermodynamically stable form of HMX. It is the most dense polymorph (1.96 g/cm^3).
- γ-HMX form is not a true polymorph but rather a hydrated molecule. It can be kept for long time at room temperature.
- δ-HMX is quite similar to the α-phase but it has not the perfect two-fold symmetry found in α-HMX. It can transform to the β-phase just in presence of β-HMX.

A summary of the structural data is given in Table 2.1.

Name	Crystal System	Density (g/cm^3)	Stability range (°C)
α-HMX	Orthorhombic	1.84	115 to 156
β-HMX	Monoclinic	1.96	RT to 115
γ-HMX	Monoclinic	1.76	$\sim$ 156
δ-HMX	Hexagonal	1.80	156 to melting

Table 2.1 – Crystal structures of HMX phases.

According to Yoo et al., there is an evidence of two more phases, ε-HMX and ϕ-HMX, although they can only appear at high pressures (12 and 27 GPa, respectively) [9]. As in the case of RDX, the polymorphic structures can be prepared using different crystallization conditions [8, 10].

The values of both impact and friction sensitivity, according to the French norms NF T70-500 and NF T70-503, are 7.4 N·m and 120 N, respectively [11, 12]. The detonation velocity reaches 9100 m/s at its maximum density. It has a negative oxygen balance of -21.6 % [5].

2.1.2 Hexogen (RDX)

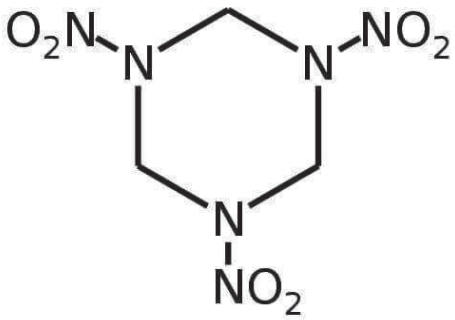

(a) Chemical formula of RDX.

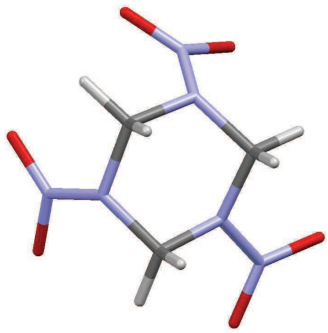

(b) Molecular conformation of RDX in the alpha phase.

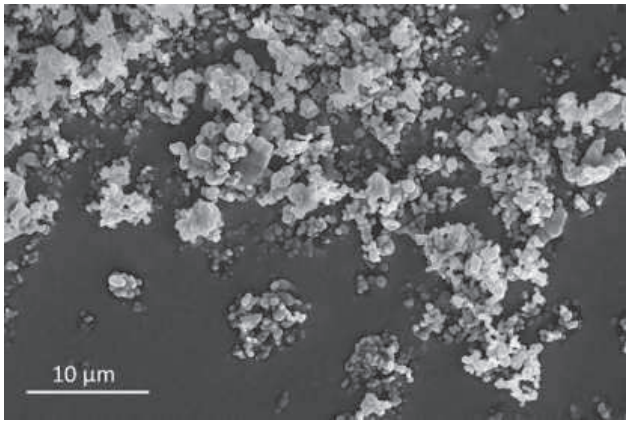

(c) SEM micrograph of RDX crystals.

Figure 2.4 – RDX: Chemical structure and crystal habit.

1, 3, 5-trinitroperhydro-1, 3, 5-triazine is the IUPAC designation for RDX (also known as cyclonite or hexogen) was first synthesized in 1899 by G. Friedrich

for medical use due to its effect to dilate blood vessels [13]. It was more than 20 years later when its potential as an high explosive was explored [14, 15].

The chemical structure of α-RDX (2.4a), a 3-D model (2.4b) and a SEM micrograph of RDX crystals (2.4c) are shown in Figure 2.4.

RDX is produced when hexamethylenetretamine and concentrated nitric acid are mixed in a batch reactor at 55 ℃ [2].

$$(CH_2)_6N_4 + 4\,HNO_3 \longrightarrow (CH_2NNO_2)_3 + 3\,HCHO + NH_4^+ + NO_3^-$$

In this work RDX used had a purity > 99.6 %. The integration of peak at 6.3 ppm shown in the ^{1}H NMR spectrum (cf. Figure 2.5) confirms this value. The spectra of RDX is quite similar to the HMX one due to the similarities of the molecules.

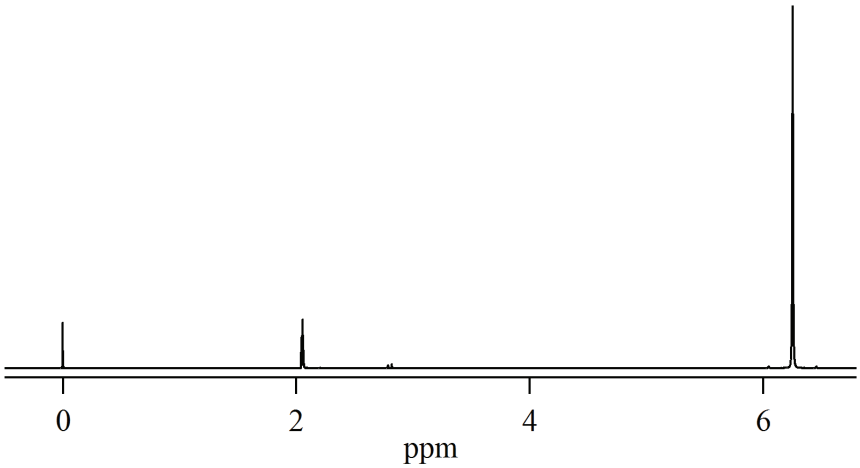

Figure 2.5 – ^{1}H NMR spectrum of RDX sample used in this work.

RDX is the main part of the well-known explosives C4 (91% of RDX and other additives), Semtex (50.2% of RDX and 49.8% of PETN in the A-form) and many others polymer bonded explosives (PBX-9XXX-series), explosives embedded in polymers matrices in order to obtain insensitive munitions.

In Figure 2.6, Raman Spectroscopy was performed on the RDX crystals. The intense and sharp peak at ~880 cm^{-1} belongs to the stretching vibration modes of the ring. A weak peak at ~850 cm^{-1} is assigned to the deformation of the nitro group. The three intense peaks at ~3000 cm^{-1} correspond to

the stretching modes of the CH_2 group. This spectrum corresponds well to α-RDX, according to the literature [16].

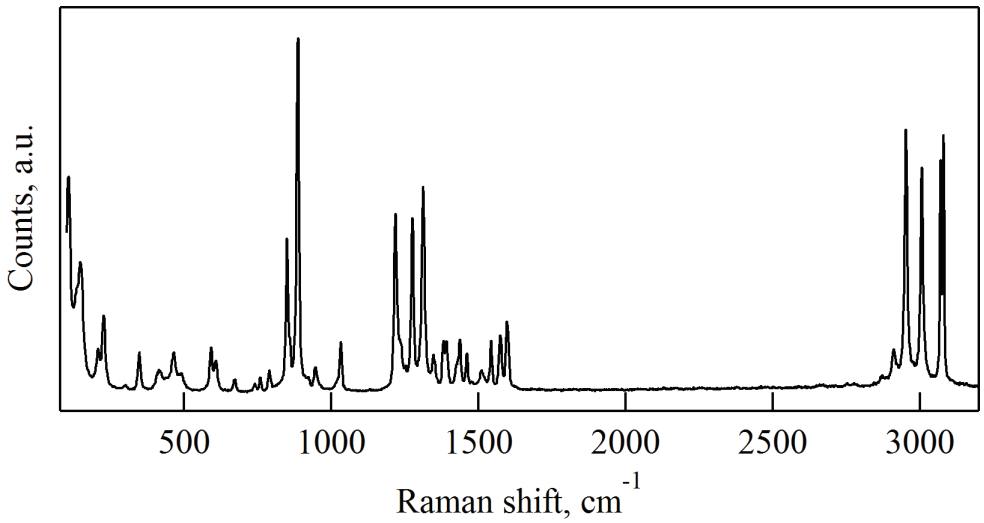

Figure 2.6 – Raman spectrum of RDX sample used in this work.

Physical properties

RDX is a non-planar six-membered ring molecule with alternated CH_2 and N–NO_2 groups. It forms colorless crystals with a maximum density of 1.82 g/cm^3. The crystals melt in-between 204 and 206 °C followed by their decomposition. The crystal structure of the stable form at room temperature, α-RDX is orthorhombic and its space group is Pbca [5, 6].

RDX has four different polymorphs which can be obtained by varying the crystallization conditions (i.e., solvents, pressure, etc.) [8, 16]:

- α-RDX has a plate-like structure and is the thermodynamically stable polymorph at ambient conditions [17].

- β-RDX is a highly metastable polymorph that can be obtained also at ambient conditions by changing the solvent, to nitrobenzene or thymol for example, but in the presence of the α-RDX it transforms to this latter polymorph [8, 16].

- γ-RDX can be formed after a reversible, first-order transition, at pressures higher than 3.9 Gpa from the α-RDX polymorph. In these experiments, pressure was not varying with temperature [18]. Only the rate of transformation was observed to increase with temperature.

- δ-RDX is a high-pressure polymorph (from $\sim$ 18 GPa) which forms through a reversible transition from γ-RDX polymorph [19, 20].

The main concern with pure RDX is its sensitivity to detonation either by impact or friction. According to the French norms NF T70-500 and NF T70-503, these values are 7.4 N·m and 120 N, respectively [11, 12]. The detonation velocity reaches 8750 m/s at its maximum density. It has a negative oxygen balance of -21.6 %.

2.1.3 Hexanitrohexaazaisowurtzitane (CL-20)

2,4,6,8,10,12-hexanitro-2,4,6,8,10,12-hexaaza-tetracyclo[5, 5, $0^{3.11}$, $0^{5.9}$]-dodecane is the IUPAC name for CL-20 (also known as HNIW). It was first synthesized in 1987 by Nielsen [21] in the laboratories of the Naval Air Warfare Center Weapons Division in China Lake, from where its name comes. It is characteristic by its cage structure, as it is shown in Figure 2.7a. Nowadays it is considered the most powerful, non-nuclear, manageable explosive [22].

CL-20 is prepared from benzylamine and glyoxal in the presence of a catalyst to produce hexabensylhexaazaisourtzitane (HBIW). In a second step, HBIW is reductively acylated to produce dibenzyltetraacetylhexaazaisowurtzitane (TAIW) which is finally debenzylated and nitrated to produce HNIW [23].

$$6\mathrm{BnNH_2} + 3\mathrm{CHO_2} \longrightarrow (\mathrm{CHNNO_2})_6$$

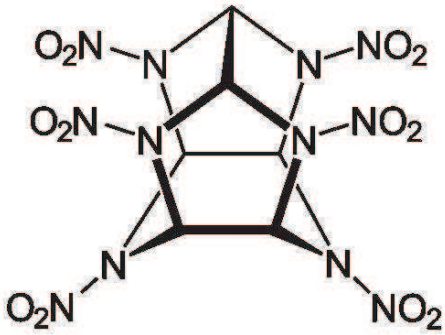

(a) Chemical formula of CL-20.

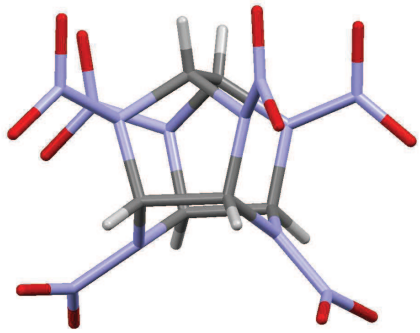

(b) Molecular conformation of CL-20 in the ϵ-phase.

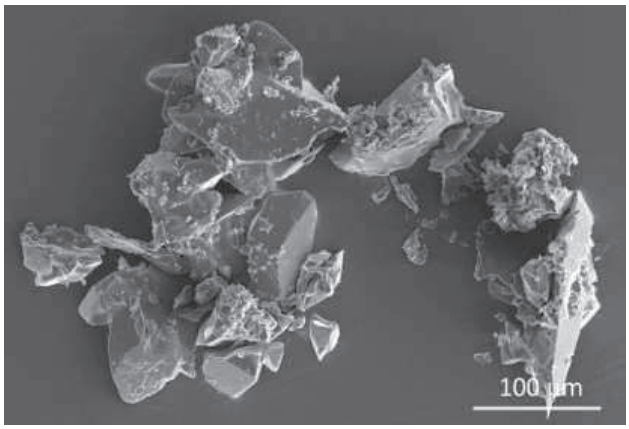

(c) SEM micrograph of ϵ-CL-20 crystals.

Figure 2.7 – CL-20: Chemical structure and crystal habit.

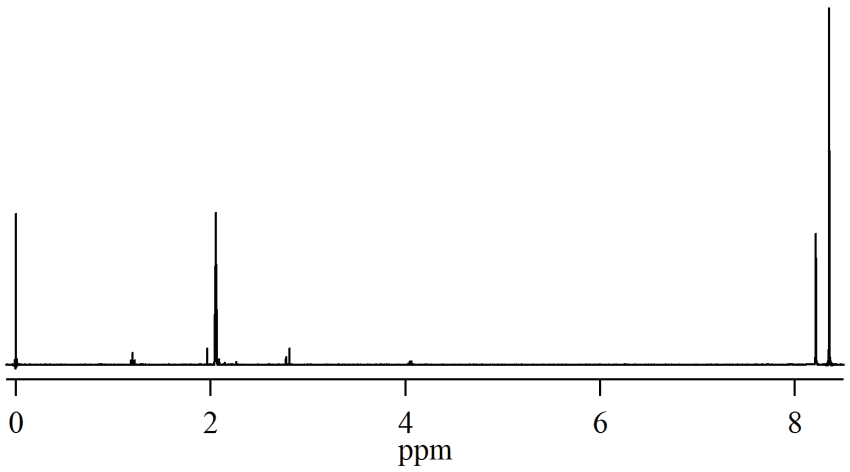

Figure 2.8 – ^{1}H NMR spectrum of CL-20 sample used in this work.

In this work CL-20 used had a purity > 93.6 % given by the integration of the double peak at $\sim$ 8.25 ppm shown in the ^{1}H NMR spectrum (cf. Figure 2.8).

In Figure 2.9 is shown a Raman spectrum of CL-20 crystals. The peaks at 250–300 cm^{-1} are assigned to the "cage" stretch vibrational modes. The peaks at 810–870 cm^{-1} correspond to the stretching of the ring and to the NO_2 scissoring. At 1200–1400 cm^{-1} appear the symmetric NO_2 stretch bands and at 3010–3070 cm^{-1} the C–H stretch lines. The strong peak at 3050 cm^{-1} confirms that it corresponds to the ϵ-phase [24].

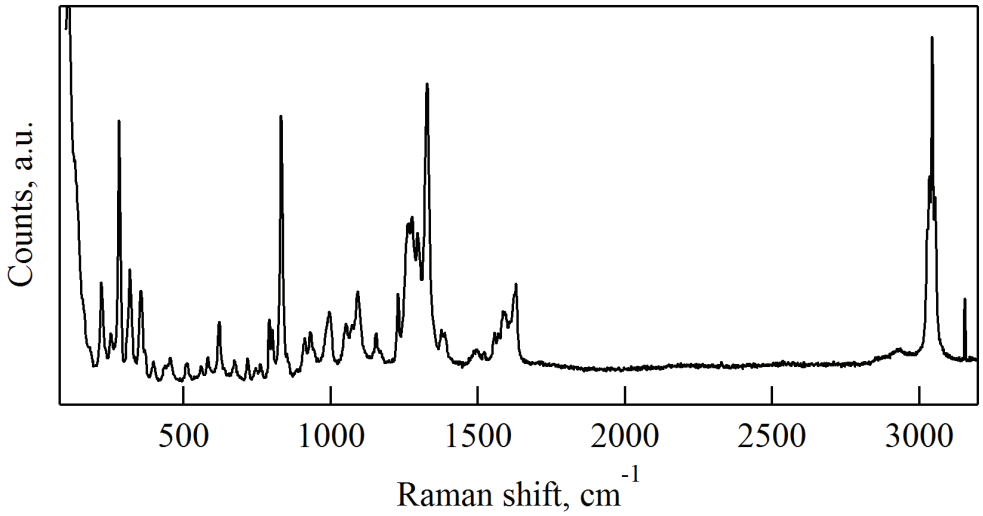

Figure 2.9 – Raman spectrum of the CL-20 sample used in this work.

Physical properties

CL-20 molecule belongs to the group of nitramines like RDX and HMX but it has a polycaged structure. The crystal structure of the most used form at room temperature, ϵ-CL-20 is monoclinic and its space group is $P2_1/a$ [25]. CL-20 has six different polymorphs, named from α to ζ. In Figure 2.10, the four polymorphs stable at room temperature and ambient pressure are presented [26].

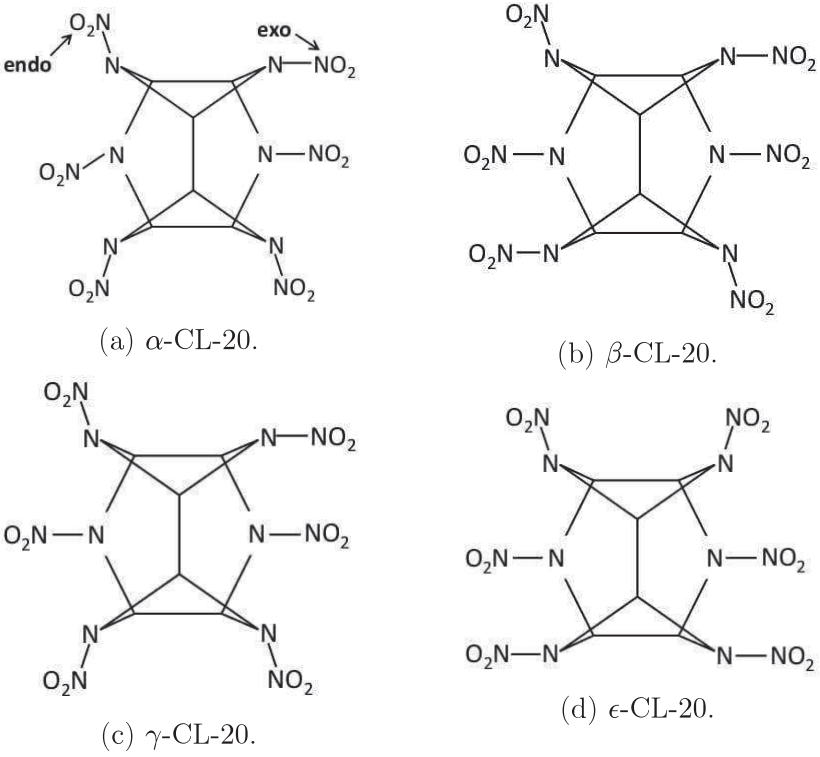

(a) α-CL-20.

(b) β-CL-20.

(c) γ-CL-20.

(d) ϵ-CL-20.

Figure 2.10 – Polymorphs of CL-20 at room temperature and ambient pressure.

Foltz et al. reported the thermodynamic stability order of the polymorphs mentioned above, which decreases from $\epsilon > \gamma > \alpha$-hydrate $> \beta$ [27].

The sensitivity to impact and friction for the ϵ-CL-20 are 4 N·m and 48 N, respectively [5]. Thus, according to these values, ϵ-CL-20 can be classified between primary and secondary-type explosive. Also, this phase has extraordinary properties in terms of stability, density (2.044 g/cm^3) and detonation velocity (9660 m/s) [26]. It has a negative oxygen balance of -10.95 %.

2.1.4 Pentrite (PETN)

3-nitrooxy-2, 2-bis(nitrooxymethyl)propylnitrate is the IUPAC name for PETN (it is known also as pentaerythritol tetranitrate or pentrite). It was first syn-

thesized in 1891 by B. Tollens and F. Wigand [28]. Like RDX, it is also used in medicine as a vasodilator drug to treat heart conditions [29, 30].

The chemical structure (2.11a), a 3-D model (2.11b) and a SEM micrograph of PETN crystals (2.11c) are shown on Figure 2.11.

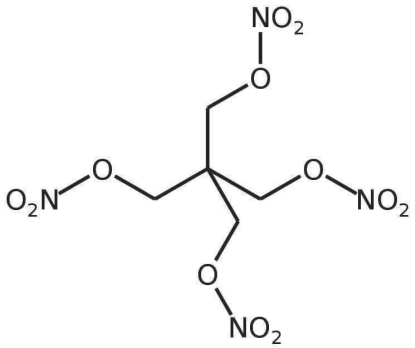

(a) Chemical formula of PETN.

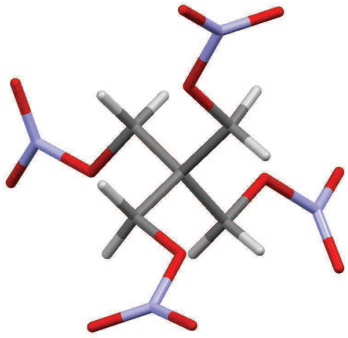

(b) Conformation of PETN in the PETN-I phase.

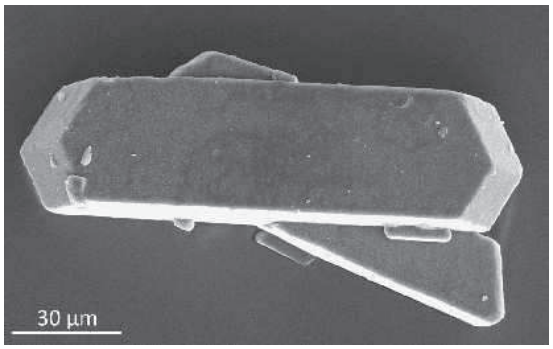

(c) SEM micrograph of PETN crystals.

Figure 2.11 – PETN: Chemical structure and crystal habit.

The condensation at 65-70 °C during 2 hours of acetaldehyde with excess formaldehyde in the presence of aqueous calcium hydroxide yields pentaerythritol, which after esterification with absolute nitric acid yields PETN [31]:

$$CH_3CHO + 4H_2C{=}O \xrightarrow{HNO_3} C(CH_2ONO_2)$$

PETN crystals used in this work had a purity greater than 99.1 % obtained after the integration of the peak at 4.65 ppm shown in the ^{1}H NMR spectrum (cf. Figure 2.12).

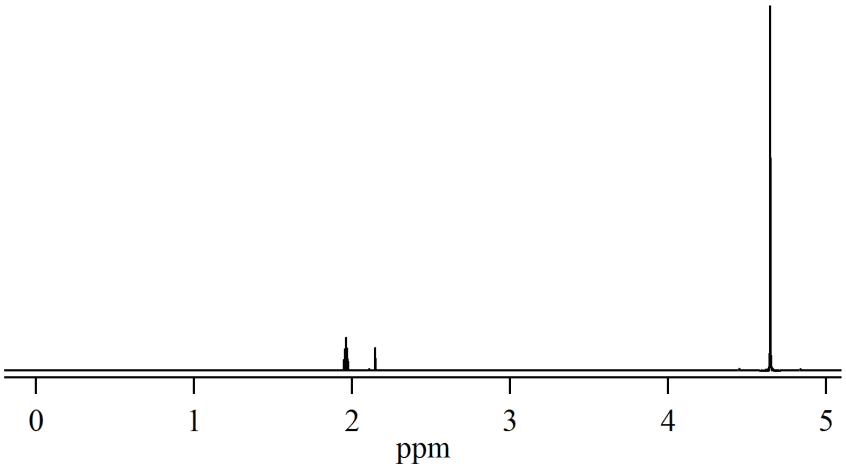

Figure 2.12 – ^{1}H NMR spectrum of PETN sample used in this work.

In Figure 2.13 is shown the Raman spectrum of PETN. Peaks at $\sim$ 3000 cm^{-1} are assigned to symmetric and asymmetric C–H bond stretching. The intense broad peak at 870–890 cm^{-1} corresponds to the stretching modes of the N–O bond whereas the symmetric and asymmetric stretching vibrations corresponding to the nitro groups appear at 1280–1300 and 1630–1670 cm^{-1}, respectively [32].

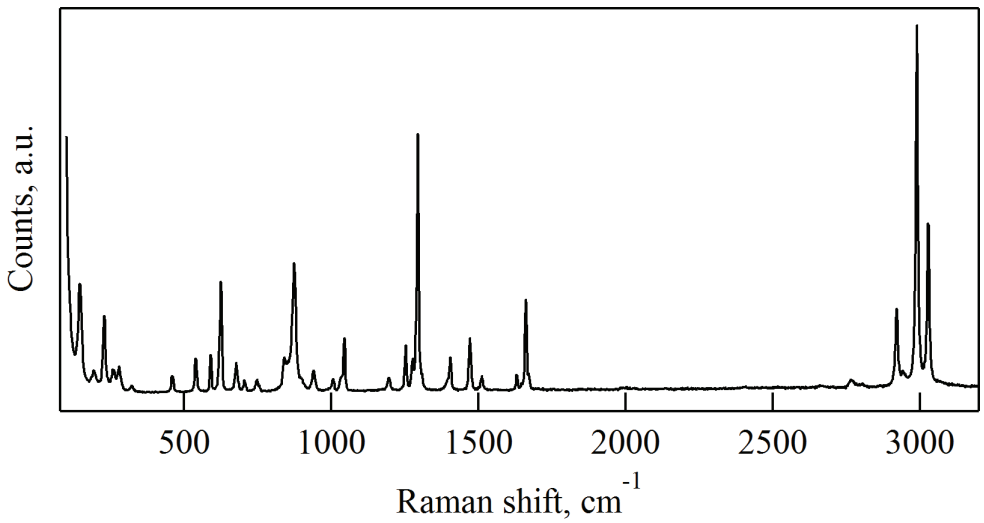

Figure 2.13 – Raman spectrum of PETN sample used in this work.

Physical properties

PETN is a highly symmetric molecule, as it can be seen in Figure 2.11b. It presents the two following polymorphic structures [33]:

- PETN-I. This polymorph is the stable structure at room temperature and ambient pressure. It adopts a tetragonal lattice when it crystallizes into white crystals. Its space group is $P\bar{4}2_1c$. This phase is stable up to 130 ℃.

- PETN-II is an orthorhombic structure. Its space group is Pcnb. It is stable from 130 ℃ to its melting point (141.3 ℃). The PETN-II phase is not stable at temperatures below 130 ℃ and quickly transforms to the PETN-I phase.

PETN is a powerful high explosive which exhibits great brisance on detonation. Its detonation velocity reaches 8310 m/s at the highest density (1.77 g/cm^3). It is the most stable and least reactive of the common nitrate ester explosives [34]. According to the French norms NF T70-500 and NF T70-503, the sensitivity to impact and friction is 3 N·m and 60 N, respectively [11, 12]. It has an oxygen balance of -10.1 % [5].

2.1.5 Trinitrotoluene (TNT)

2-methyl-1,3,5-trinitrobenzene is the IUPAC name for TNT (also known as 2,4,6-trinitrotoluene). TNT was first synthesised in 1863 by J. Wilbrand [35].

The chemical structure (2.14a), a 3-D model (2.14b) and a micrograph of TNT crystals (2.14c) used on this work are show on Figure 2.14:

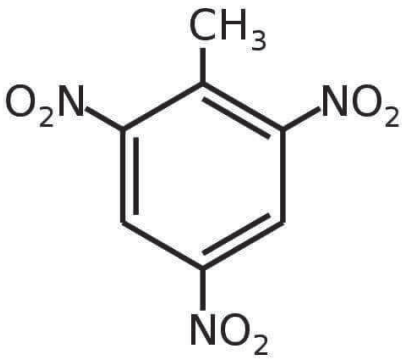

(a) Chemical formula of TNT.

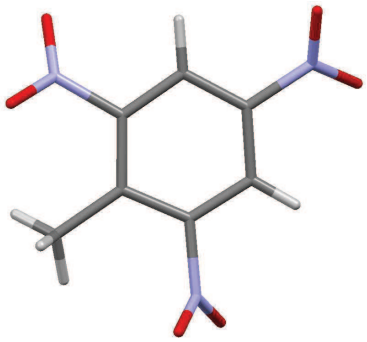

(b) Molecular conformation of TNT in the monoclinic phase.

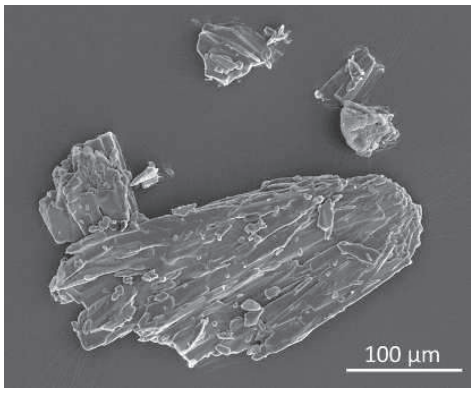

(c) SEM micrograph of TNT crystals.

Figure 2.14 – TNT: Chemical structure and crystal habit.

It is produced by step-wise nitration of toluene with mixed nitric and sulfuric acid.

$$C_7H_8 + 3HNO_3 \longrightarrow C_7H_5N_3O_6 + 3H_2O$$

TNT crystals used in this work had a purity greater than 99.7 %. This is the value obtained after the integration of the peak at 9 ppm shown in the ^{1}H NMR spectrum (cf. Figure 2.15).

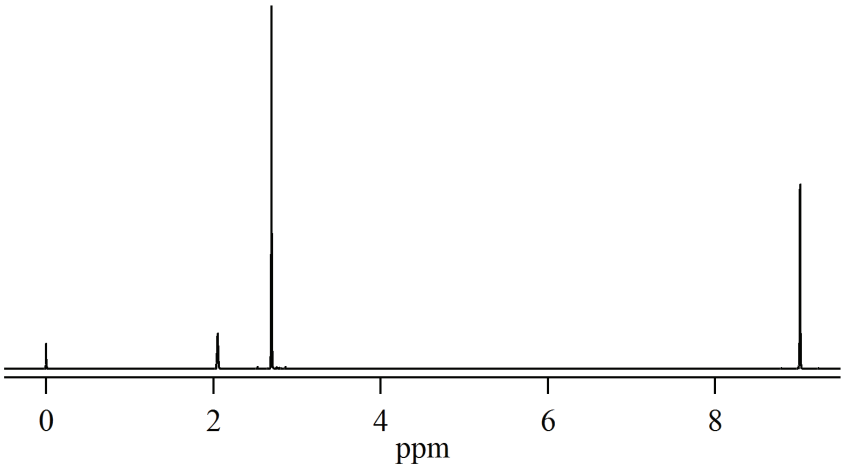

Figure 2.15 – ^{1}H NMR spectrum of the TNT sample used in this work.

In Figure 2.16 it is shown the TNT Raman spectrum. The strongest peak at ∼1400 cm^{-1} can be assigned to the CH_3 symmetric bend mode. The two sharp peaks at 1369 and 1533 belong to the symmetric and antisymmetric N–O_2 bands [36].

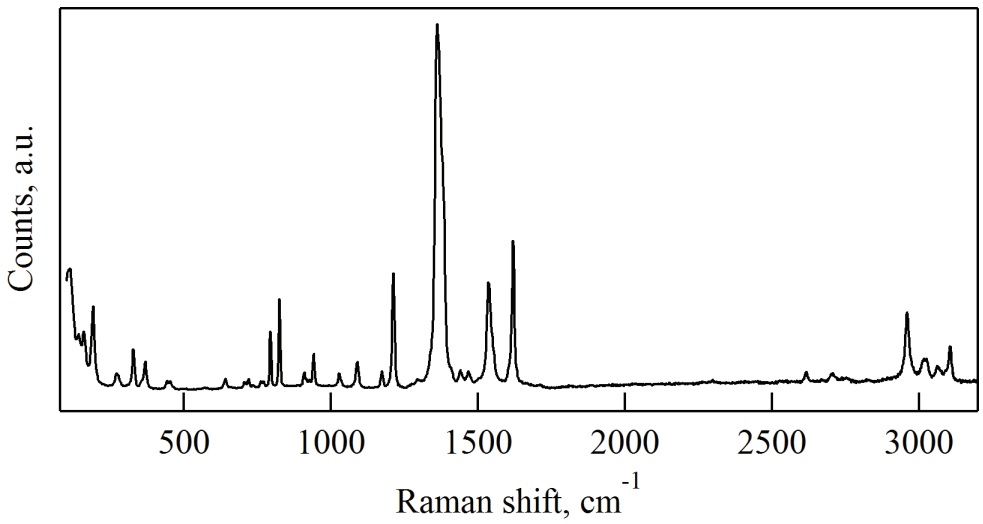

Figure 2.16 – Raman spectrum of TNT sample used in this work.

Physical properties

Two polymorphic structures of TNT are described in the literature [8]. It can exist as colorless orthorhombic crystals or as pale yellow monoclinic needles. The orthorhombic form is a metastable structure at room temperature that undergoes a solid-solid phase transition at 70 ℃ followed by its melting at 81 ℃. This transition has also been observed by Gallagher et al. after a long period of storage [37].

On the contrary, the monoclinic form is stable at room temperature until its melting point at 81 ℃ [6]. Its space group is $P2_1/c$ [38]. In this form, TNT reaches a density of 1.60 g/cm^3 and detonation velocities of 6900 m/s and has an oxygen balance of -73.9 % [5]. According to the French norms NF T70-500 and NF T70-503, the sensitivity to impact and friction is 15 N·m and 353 N, respectively [11, 12].

2.1.6 Co-crystals of CL-20/TNT and CL-20/HMX

Two co-crystals has been studied. CL-20/TNT in an equimolar proportion and CL-20/HMX with a molar ratio of 2:1. In 2011, Bolton and Matzger synthesize for the first time the co-crystal CL-20/TNT growth from saturated solutions by a solvent-mediated conversion [39]. Some years later, Spitzer et al. synthesized the same compound using the Spray Flash Evaporation process [40], which leads to smaller crystals. The special feature of this compound is that it solves the problematic of high sensitivity of pure CL-20 retaining the explosives properties of its components by dilution with TNT.

As it is shown in Figure 2.17a, it is composed by TNT and CL-20 molecules which are linked by hydrogen bonds.

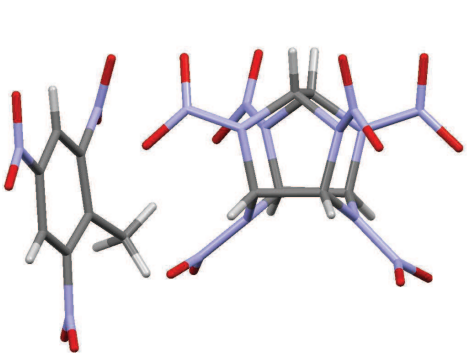

(a) 3-D model of CL-20/TNT.

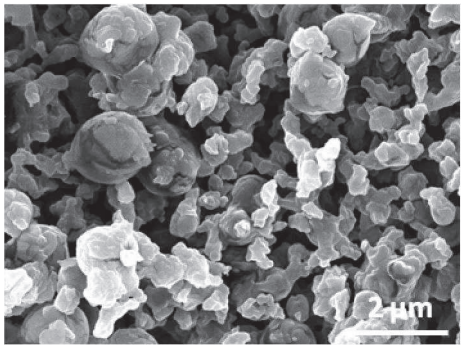

(b) SEM micrograph of CL-20/TNT co-crystals used in this work.

Figure 2.17 – 3-D model and micrograph of CL-20/TNT co-crystal.

On the other hand, CL-20/HMX is formed in a 2:1 molar ratio, as it can be seen from Figure 2.18a. It was first synthesized by Bolton et al. [41] by slow evaporation of a saturated solution, although as in the case of CL-20/TNT, it can be synthesized using the Spray Flash Evaporation process as well. From a military point of view, this co-crystal is more interesting than its homologue with TNT due to the higher explosive power of HMX.

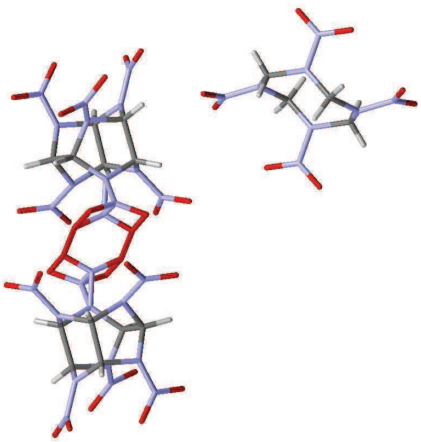

(a) 3-D model of CL-20/HMX.

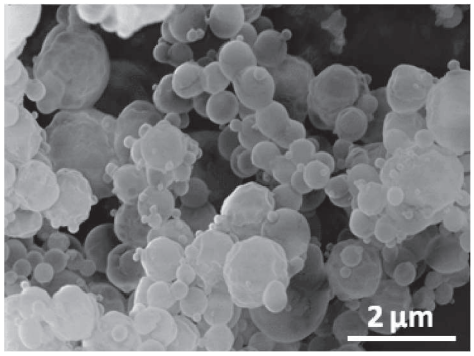

(b) SEM micrograph of CL-20/HMX co-crystals used in this work.

Figure 2.18 – 3-D model and micrograph of CL-20/HMX co-crystal.

Physical properties

CL-20-TNT is formed by hydrogen bonds between nitro group oxygens and aliphatic hydrogens as well as by interactions between the electron-deficient ring of TNT and the nitro groups of CL-20. A key feature of this co-crystal is the combination of aromatic and aliphatic energetic components in the same crystalline structure. The space group of the form used in this work is Pbca, but we found that its lattice is slightly distorted with respect to the literature data. The b parameter of the orthorhombic lattice is slightly larger than the one of the structure described in the literature. Our supposition is that the difference is due to the different synthesis path, growth from saturated solution for the structure reported in the literature and from Spray Flash Evaporation in our case. Also, there is a small amount of pure ϵ-CL-20 ($\sim$ 3%) in our co-crystals (cf. Figure 5.5).

This structure is stable up to 130-135 ℃ where it melts to liquid TNT (T_m = 81 ℃) and ϵ-CL-20.

The particle size analysis performed on the CL-20/TNT sample reveals an average particle size of 100 nm, as it can be seen in Figure 5.4a. This data clearly shows that the Flash Evaporation process can produce much smaller particles than the classical methods of recrystrallization.

As in the case of CL-20/TNT, hydrogen bonds maintain the co-crystal structure in CL-20/HMX. The space group of this compound is P21/c. In this case, even if the sample analyzed was synthesized using another method, the disagreement with data described in the literature is negligible, as it can be seen on Figure 5.5.

Figure 5.4b shows a particle size distribution. The mean size for these particles is even smaller (58 nm) by the same reason as in the case of CL-20/TNT.

Summary of the thermodynamic data of the energetic materials studied in this work

In Table 2.2 are summarized the thermodynamic data of the energetic materials used in this work. Most of the parameters have been determined from experimental DSC measurements at 5 °C min^{-1}.

Material	C_p at 298 K ($Jg^{-1}K^{-1}$)	Melting onset (°C)	$\Delta H_{melt.}$ change (Jg^{-1})	Decomposition peak max. (°C)	$\Delta H_{decomp.}$ change (Jg^{-1})
HMX	1.25*	-	-	274.2	3754.3
RDX	1.25*	203.9	85.1	209.8	3590.4
CL-20	1.45	-	-	235.6	5848.4
PETN	1.38*	139.3	142.9	185.2	3381.0
TNT	1.09*	79.1	87.4	303.5	3487.8
CL-20/TNT	1.69	130.3	83.3	214.3	4291.5
CL-20/HMX	1.64	-	-	227.7	5665.8

Table 2.2 – Thermoanalytical data of the materials studied on this work.* Taken from [5]

2.2 Characterization techniques

In this second part of this chapter, a short description of the techniques used in this work is given. Due to its importance in this work, the description of Nanocalorimetry will be presented more extensively in Chapter 3.

2.2.1 Differential Scanning Calorimetry

The principle of a DSC have been explained in the previous chapter.

A heat-flux DSC, Mettler-Toledo DSC 1 (cf. Figure 2.19a), was used to characterize the energetic materials used in this work. The resolution of this device is 0.4 µW and 0.2 K of accuracy, according to the manufacturer.

A DSC Q1000 from TA Instruments (cf. Figure 2.19b) was also used. This calorimeter has a temperature precision of 0.05 K and a sensitivity of 0.2 µW, according to the manufacturer. In both devices, the heating rates used were from 1 to 40 °C/min.

DSC-M20 gold plated crucibles of 20 µl from Swissi were used due to the high pressure generated during the decomposition of the materials. They can manage up to 217 bars.

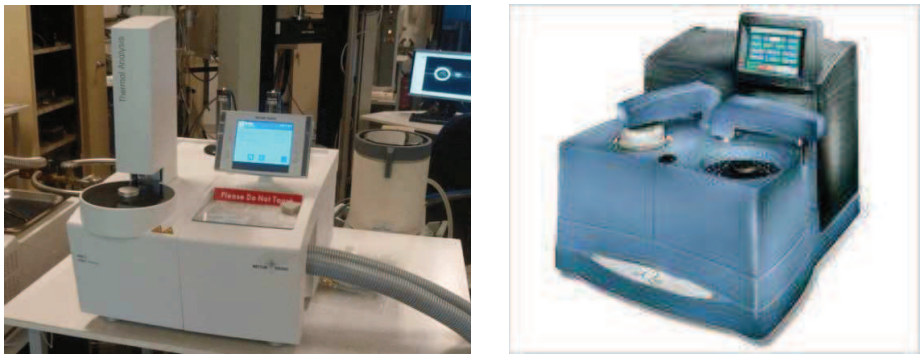

(a) Mettler-Toledo DSC 1. (b) TA DSC Q1000.

Figure 2.19 – DSC devices used to characterize energetic materials.

2.2.2 Polarized optical microscopy

Optical microscopy is a relatively useful technique despite its apparent simplicity. In this work, both reflection and transmission geometries have been used.

In polarized optical microscopy (POM), the birefringence is used to distinguish different morphological features on the sample. Birefringence is an inherent property of materials which rotate the polarization plane of linearly-polarized light when it passes through them. The birefringence is given by:

$$\Delta n = n_1 - n_2 \tag{2.2.1}$$

where n_1 and n_2 are refractive indices corresponding to the two perpendicular directions.

In this work, POM observations have been carried out using an Olympus BX51 microscope equipped with a DCM 310 Microscope CMOS camera, in transmission geometry. This camera employs a single-chip charge-coupled device (CCD) sensor of 3.2 million effective pixels. A Leica DM2500 microscope with a Sony DXC-390P camera have been used in reflection geometry. This camera has a 1/3" type DSP 3-CCD sensor.

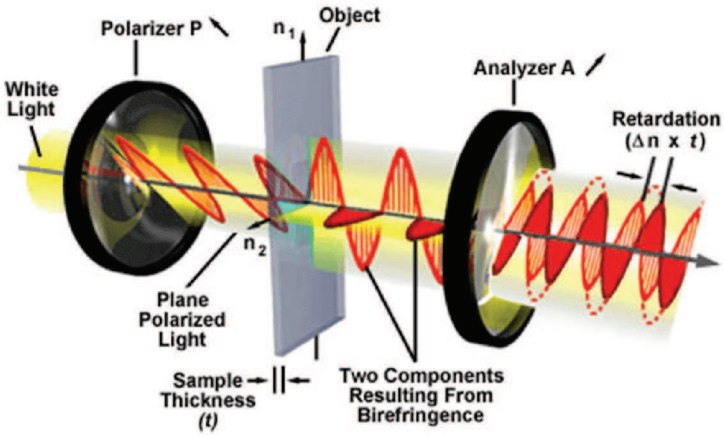

Figure 2.20 – In polarized optical microscopy, the sample is placed between crossed polars.

2.2.3 Raman Spectroscopy

It is a spectroscopic technique used to observe vibrational, rotational, and other low-frequency modes in a sample. It is commonly used in material science to provide a fingerprint to identify molecules in a sample.

The principle of this technique is based on inelastic scattering, or Raman scattering, of monochromatic light. This light interacts with molecular vibrations, phonons or other excitations in the sample, resulting in the energy of the photons being shifted up or down. The shift in energy gives information about the vibrational modes in the sample. If the final vibrational state of the molecule is more energetic than the initial state, the inelastically scattered photon will be shifted to a lower frequency for the total energy of the system to remain balanced (Stokes shift). If the final vibrational state is less energetic than the initial state, then the inelastically scattered photon will be shifted to a higher frequency (anti-Stokes shift). Raman scattering is an example of inelastic scattering because of the energy and momentum transfer between the photons and the molecules during the interaction. Rayleigh scattering is an example of elastic scattering, the energy of the scattered Rayleigh scattering is of the same frequency (wavelength) as the incoming electromagnetic radiation. In Figure 2.21 these interactions are depicted.

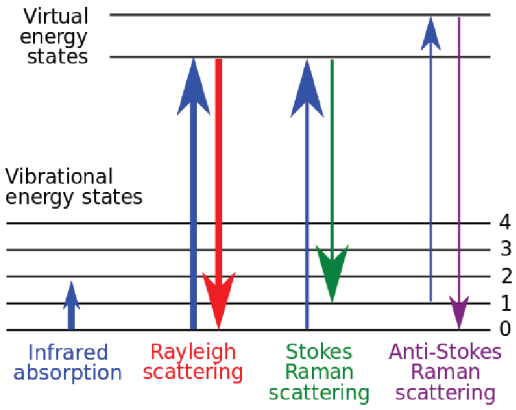

Figure 2.21 – Energy-levels diagram of the states involved in Raman signal. The line thickness is roughly proportional to the signal strength from the different transitions.

In our case, a Renishaw inVia Raman microscope with a 633 nm green laser was used to obtain the local-scale spectra of the materials used in this work. The Raman spectra were obtained from 200 cm^{-1} to 3200 cm^{-1}. The system was calibrated using a silicon wafer (vibration at 520.56 cm^{-1}). The acquisition of each spectrum was performed by varying the acquisition time. Preliminary experiments were performed to determine the maximal laser power one can use without destroying sample, the laser power was then fixed at 10% for the experiments.

2.2.4 Wide-Angle X-ray Scattering using synchrotron radiation

In Figure 2.22 a general scheme of a synchrotron radiation facility is shown. A synchrotron is an extremely powerful source of X-rays produced by highly energetic electrons (light blue beam) moving in a large circle in a storage ring. From physics, it is known that when charged particles are in uniform motion, no radiation is observed. What it is observed as electromagnetic radiation is a field perturbation during acceleration of these charged particles due to the rearrangement of their electric fields traveling away from the charge at the velocity of light. This is the phenomenon behind all synchrotron science.

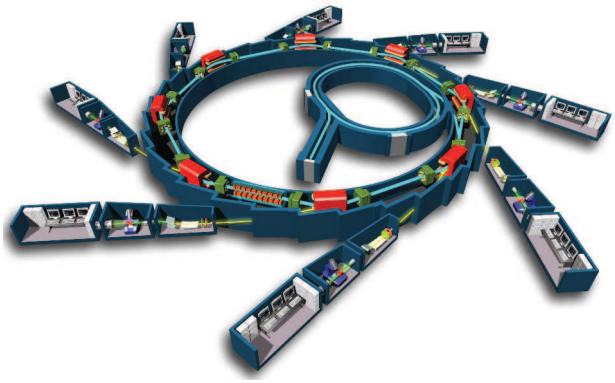

Figure 2.22 – General diagram of a Synchrotron Facility. The image is taken from Wikipedia.

The principle elements of a synchrotron radiation facility are:

- Linac: is an electron gun that produces accelerated electrons. The electrons are packed in "bunches" and accelerated to a relatively high energy (200 million eV ca.), which is sufficient for injection into the booster synchrotron.

- Booster synchrotron: is a pre-accelerator ring where the electrons are accelerated to a very high energy (several GeV) before being injected into the synchrotron storage ring. The booster synchrotron only works a few times a day for a few minutes, when the storage ring is refilled. Every very short time pulses (some milliseconds), it can send a bunch of high energy electrons into to the storage ring.

- Synchrotron (storage ring): is a circular tube where the electrons circle for hours close to the speed of light, being accelerated by electric fields in the straight sections between the green squares (cf. Figure 2.22). The tube is maintained at very low pressure (around 10^{-9} mbar). As the electrons travel through the ring, they pass through different types of magnets that bend the beam. When the beam is bent the electrons emit synchrotron radiation (shown in yellow).

- Beamlines: The X-ray beams emitted by the electrons are directed toward the "beamlines" (the straight lines branching out of the synchrotron) that surround the storage ring in the experimental hall. Each beamline is designed for use with a specific technique or for a specific type of research.

2.3 Sample preparation

Samples in the form of micro-particles are placed on the sensors using a Micromanipulator MM-33 from Sutter Instrument. Due to the size of the

samples used in this study, an eyelash as a tip of the micromanipulator has been used (cf. Figure 2.23).

When the micro-particles are picked up from a glass slide where they have been previously dispersed, they are placed on the active area of the sensors under an optical microscope working in reflection mode (cf. Figure 2.24).

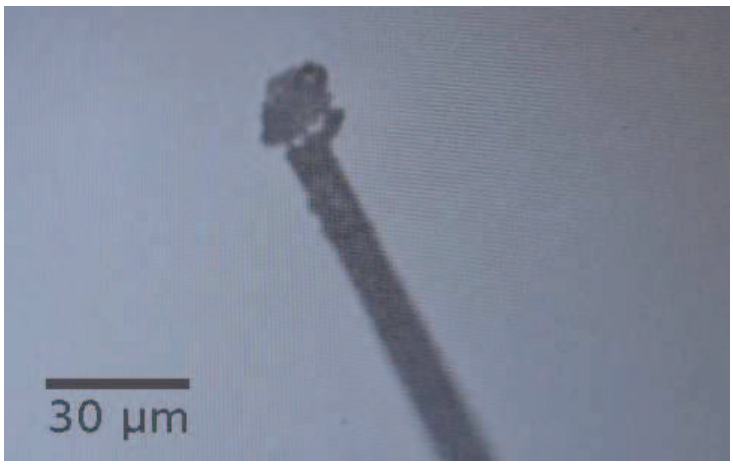

Figure 2.23 – Eyelash with an explosive micro-particle on the tip. Notice the dimensions of the samples used in this work.

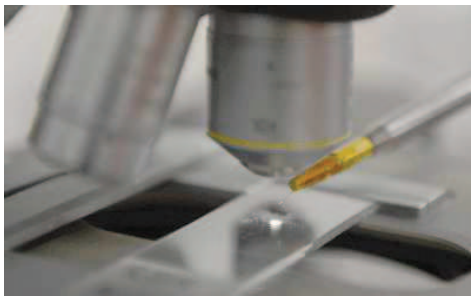

(a) Picking up explosives particles with the micromanipulator.

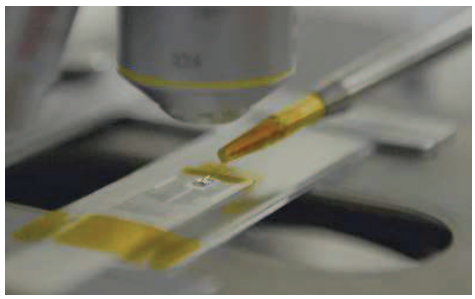

(b) Placing samples on the nanocalorimetric sensor.

Figure 2.24 – Sample preparation.

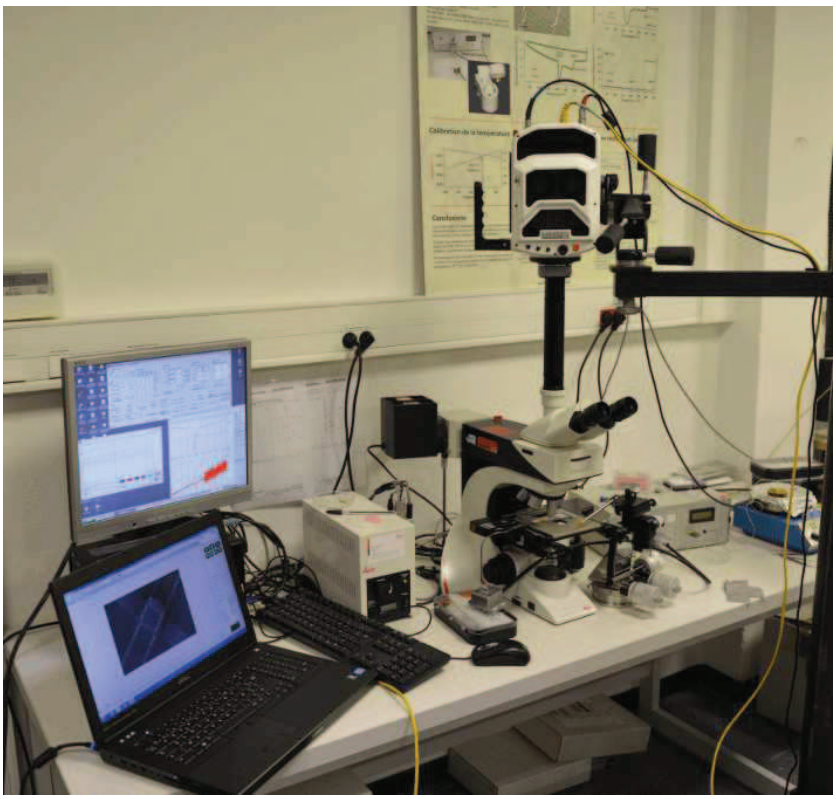

Figure 2.25 – Set-up for the combination of nanocalorimeter with a Fast CCD Camera.

The set-up shown in Figure 2.25 is especially useful to follow the experiments performed with the nanocalorimeter. Due to the extremely high temporal resolution provided by this latter, a high-speed camera Phantom V1610 from Vision Research has been used to follow the course of the heating/cooling processes. This camera can record up to 1 million frames per second at the lowest resolution. In the experiments performed in this work, a resolution of 512 × 512 pixels has been used with a frame rate of 20000 images per second. It makes use of a widescreen CMOS 35.8×22.4 mm sensor saving the footage at the speed of 16 gigapixels per second. The sensor pixel size is 28 µm with 12-bit depth per pixel.

The synchronization between the high-speed camera and the nanocalorimeter was done via a TTL connection provided by the nanocalorimeter which can trigger a 5 volts signal to the camera.

[1] W. Bachmann, J. Sheehan, *Journal of the American Chemical Society* **1949**, *71*, 1842–1845.
[2] J. Akhavan, *The Chemistry of Explosives*, The Royal Society of Chemistry, TJ International Ltd, Padstow, Cornwall, UK, **2004**.
[3] D. Moore, R. Scharff, *Analytical and bioanalytical chemistry* **2009**, *393*, 1571–1578.
[4] K. McNesby, J. Wolfe, J. Morris, R. Pesce-Rodriguez, *Journal of Raman spectroscopy* **1994**, *25*, 75–87.
[5] R. Meyer, A. Homburg, *Explosives*, John Wiley & Sons, **2007**.
[6] G. Miller, A. Garroway, A Review of the Crystal Structures of Common Explosives. Part I: RDX, HMX, TNT, PETN, and Tetryl, tech. rep., DTIC Document, **2001**.
[7] H. Cady, A. Larson, D. Cromer, *Acta Crystallographica* **1963**, *16*, 617–623.
[8] W. McCrone, *Analytical Chemistry* **1950**, *22*, 1225–1226.
[9] C. Yoo, H. Cynn, *The Journal of Chemical Physics* **1999**, *111*, 10229–10235.
[10] C. Achuthan, C. Jose, *Propellants Explosives Pyrotechnics* **1990**, *15*, 271–275.
[11] AFNOR, MATERIAUX ENERGETIQUES DE DEFENSE - SECURITE, VULNERABILITE - SENSIBILITE AU CHOC, NF T70–500, Association Française de Normalisation, France.
[12] AFNOR, MATERIAUX ENERGETIQUES DE DEFENSE - SECURITE, VULNERABILITE - SENSIBILITE AU FROTTEMENT, NF T70–503, Association Française de Normalisation, France.
[13] H. Henning, Patent, 104:280, **1899**.
[14] E. von Herz, Patent, 88:759, **1920**.
[15] E. von Herz, Patent, 92:926, **1921**.
[16] R. Karpowicz, S. Sergio, T. Brill, *Industrial & engineering chemistry product research and development* **1983**, *22*, 363–365.
[17] P. Hakey, W. Ouellette, J. Zubieta, T. Korter, *Acta Crystallographica Section E: Structure Reports Online* **2008**, *64*, o1428.
[18] P. Miller, S. Block, G. Piermarini, *Combustion and Flame* **1991**, *83*, 174–184.
[19] J. Ciezak, T. Jenkins, *Propellants Explosives Pyrotechnics* **2008**, *33*, 390–395.
[20] J. Ciezak, T. Jenkins, Z. Liu, R. Hemley, *The Journal of Physical Chemistry A* **2007**, *111*, 59–63.
[21] A. Nielsen, Synthesis of polynitropolyaza caged nitramines, **1987**.

[22] U. Nair, R. Sivabalan, G. Gore, M. Geetha, S. Asthana, H. Singh, *Combustion Explosion and Shock Waves* **2005**, *41*, 121–132.
[23] A. Nielsen, Caged polynitramine compound, US Patent 5,693,794, **1997**.
[24] P. Goede, N. Latypov, H. Östmark, *Propellants Explosives Pyrotechnics* **2004**, *29*, 205–208.
[25] A. van der Heijden, R. Bouma, *Crystal growth & design* **2004**, *4*, 999–1007.
[26] S. Dumas, PhD thesis, Université Claude Bernard-Lyon I, **2003**.
[27] M. Foltz, C. Coon, F. Garcia, A. Nichols, *Propellants explosives pyrotechnics* **1994**, *19*, 19–25.
[28] B. Tollens, P. Wigand, *Justus Liebigs Annalen der Chemie* **1891**, *265*, 316–340.
[29] M. Ebadi, *CRC desk reference of clinical pharmacology*, CRC Press, **1997**.
[30] H. Russek, *The American journal of the medical sciences* **1966**, *252*, 9–20.
[31] T. Davis, *Chemistry of Powder and Explosives*, Angriff Press, reprint edition, **2012**.
[32] K. E. Lipinska-Kalita, M. G. Pravica, M. Nicol, *The Journal of Physical Chemistry B* **2005**, *109*, 19223–19227.
[33] H. Cady, A. Larson, *Acta Crystallographica Section B: Structural Crystallography and Crystal Chemistry* **1975**, *31*, 1864–1869.
[34] J. Agrawal, R. Hodgson, *Organic chemistry of explosives*, Wiley. com, **2007**.
[35] J. Wilbrand, *Justus Liebigs Annalen der Chemie* **1863**, *128*, 178–179.
[36] I. R. Lewis, N. W. Daniel, P. R. Griffiths, *Applied spectroscopy* **1997**, *51*, 1854–1867.
[37] H. Gallagher, J. Sherwood, *J. Chem. Soc. Faraday Trans.* **1996**, *92*, 2107–2116.
[38] H. Gallagher, K. Roberts, J. Sherwood, L. Smith, *Journal of material chemistry* **1997**, *7*, 229–235.
[39] O. Bolton, A. Matzger, *Angewandte Chemie International Edition* **2011**, *50*, 8960–8963.
[40] D. Spitzer, B. Risse, F. Schnell, V. Pichot, M. Klaumünzer, M. Schaefer, *Scientific reports* **2014**, *4*.
[41] O. Bolton, L. Simke, P. Pagoria, A. Matzger, *Crystal Growth & Design* **2012**, *12*, 4311–4314.

Chapter 3

Nanocalorimetry

This chapter is devoted to Nanocalorimetry. In the first part of the chapter a description of the set-up and notions of the operations which can be done with the device used in this work will be given, along with a short description of the calibration procedure. The thermal gradients across the nanocalorimetric sensors are measured by placing an indium particle at different places on the active area of the sensors.

To conclude, a paper showing the possibilities of combination of the set-up provided by the nanocalorimeter with synchrotron radiation at the European Synchrotron Radiation Facility.

3.1 The nanocalorimeter

The uniqueness of Nanocalorimetry is the ability to handle extremely small amounts of sample, i.e., in the range of nano- or pico-grams. It is noteworthy that conventional DSC typically uses milli-grams of sample. This makes a difference of about six orders of magnitude with Nanocalorimetry. The sensitivity required to sense such small amounts of sample is due to the possibility to perform heating/cooling ramps at extremely high rates (up 10^6 °C s^{-1}), which is a consequence of using such small sample masses in the measurements. This allows to investigate samples which cannot be addressed with conventional DSC, such as ultra-thin films [1, 2], metal nanoparticles [3, 4] or materials in their real conditions of processing [5–7].

The nanocalorimeter used in this work employs commercial gas sensors (cf. Figure 3.1). The ceramic housing allows measurements in transmission. The active area of these nanocalorimetric sensors is fabricated on a thin free-standing membrane of silicon nitride, a material with a relatively low thermal conductivity. Heating of the nanocalorimetric sensor can be realized by applying voltage on specially designed heating resistances (horizontal wide green stripes on Figure 3.1b). The sensor temperature can be measured using an array of thermopiles (cf. six small rectangles on Figure 3.1b) assembled on the active area.

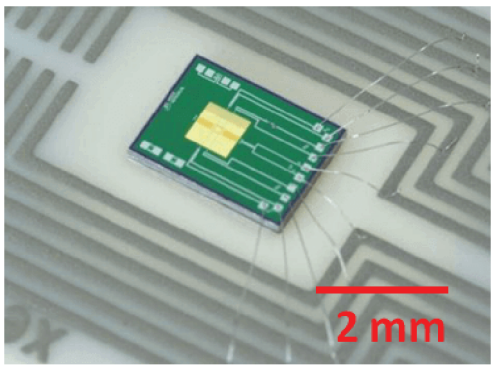

(a) Sensor mounted on a ceramic planar housing.

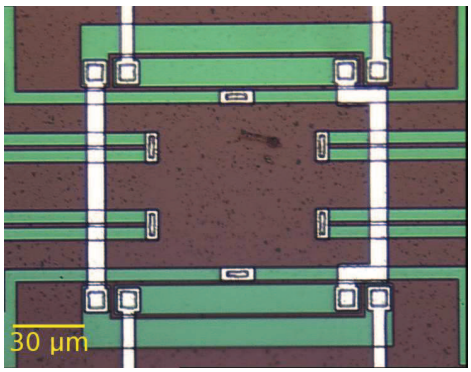

(b) Close view of the active area of a XEN-39391 sensor.

Figure 3.1 – Commercial gas sensors used in this work.

The nanocalorimeter is designed to work with its own interface which can be controlled through the following windows:

- Main control panel (cf. Figure 3.2).

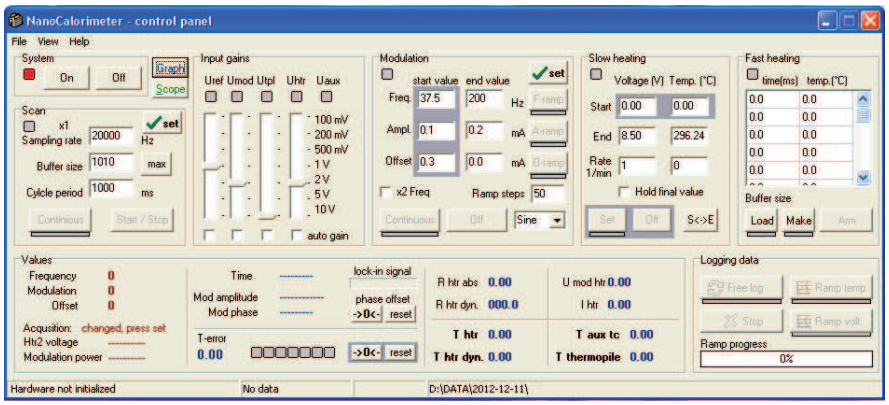

Figure 3.2 – Main control panel of the nanocalorimeter

This is the main panel of the nanocalorimeter. All operations can be realized from here and also other windows can be activated from it (e.g., the Calibration window, Signal viewer, etc.).

- Graph panel (cf. Figure 3.3).

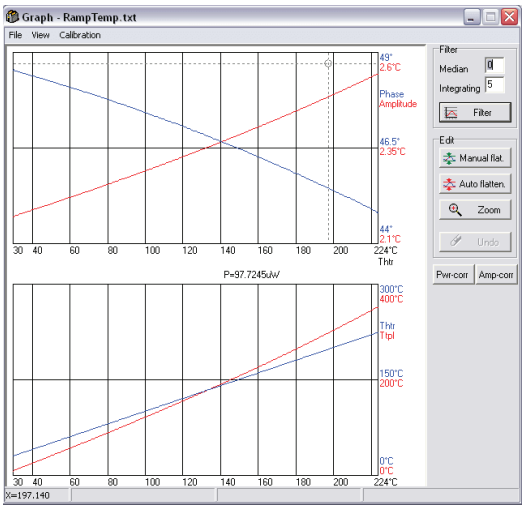

Figure 3.3 – Heating process displayed in the graph panel.

The graph panel is used to monitor the current experiment and to make a rough analysis of the results obtained. For example, it is possible to fit data using the built-in functions or to flatten the curves for a better visualization of the thermal events.

- Scope panel (cf. Figure 3.4).

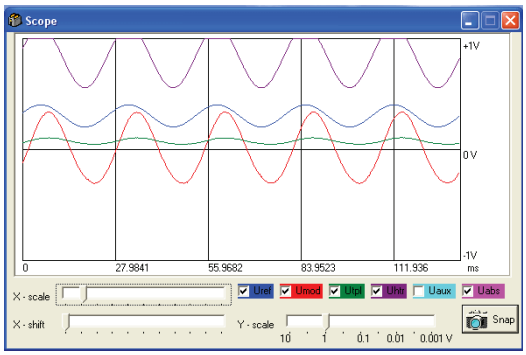

Figure 3.4 – Signals of the interface channels displayed in real time.

The scope window allows monitoring signals in all channels in real time. When "Fast Heating" mode is used, it allows displaying the voltage pulse that it will be applied. It is possible also to save the waveforms into a text file using the "Snapshot" button.

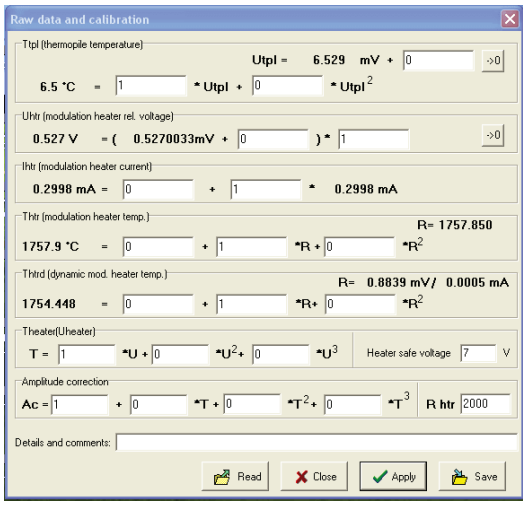

Figure 3.5 – Calibration window where all the calibration coefficients will be stored.

- Raw data and calibration panel (cf. Figure 3.5).

  All the calibration coefficients are accessible from this panel. The panel allows to save or to load different calibration files corresponding to different types of sensors.

The AC and DC nanocalorimetric experiments can be realized, thanks to the home-built controller (cf. Figure 1.10) that can be operated from a computer running under Windows OS. It is capable of applying custom temperature programs to the heaters of the nanocalorimetric sensor and performing fast readout of the thermopile signal of the sensor. During the experiment, a pulse of current is applied through the metal strips, which are heated by Joule heating. In addition, the controller can measure in real time the electrical resistance of these heating elements, the so-called guard and/or modulator heaters, to refine the computation of the Joule power released by the heaters and to determine the heater temperature. In the AC mode, the controller sends a periodic oscillating signal to the heaters and performs an on-time Fourier analysis of the thermopile response to evaluate the reversing and non-reversing components of the heat capacity.

3.2 Calibration of nanocalorimetric sensors

One of the most important preparation steps is the calibration procedure because all quantitative thermal measurements rely on the calibration coefficients. These coefficients link the voltage on the sensor and its temperature or describe the temperature dependence of the heater resistance as well as the one for the thermopiles. In order to perform the calibration, standard temperature calibrants are used (e.g., indium, tin and zinc) [8].

It is noteworthy that the sensors have to be annealed before starting any measurement. This is a mandatory step because we often observe an exponential decay of the electrical resistance of the sensors over the number

of experiments performed. An example concerning XEN-39391 sensors after consecutive experiments is shown in Figure 3.6.

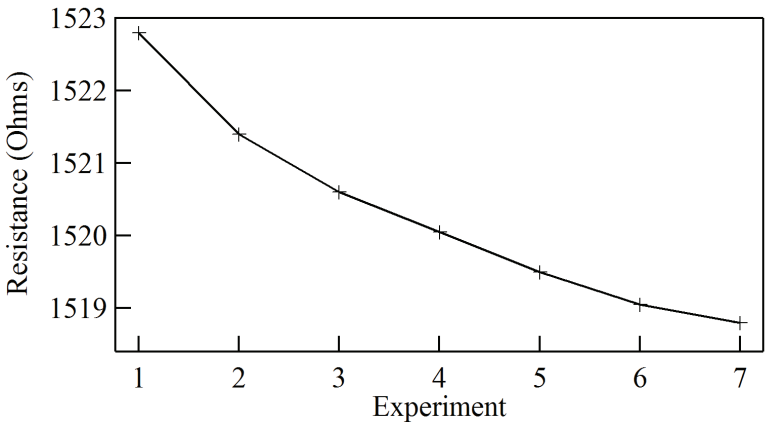

Figure 3.6 – Resistance decay as a function of the number of consecutive experiments performed on XEN-39391 sensors.

To avoid such change in the electrical resistance of the heaters, the sensors have to be annealed in vacuum at moderate temperatures (150–200 °C) during one hour approximately in order to relax the stresses generated during the fabrication process. After this thermal treatment, the resistance value stays practically constant (cf. Figure 3.7).

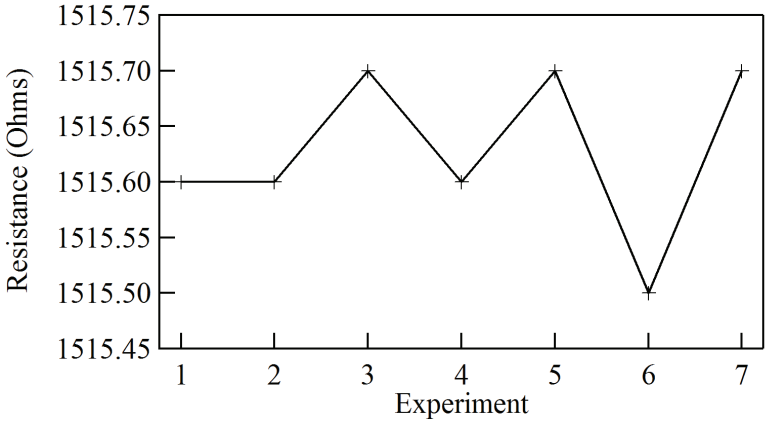

Figure 3.7 – Resistance values after annealing for XEN-39391 sensors.

The temperature calibration procedure is fully described on Ref. [9]. But

a slightly changed version of the calibration procedure has been used in this work. In this case, the calibration steps are the following:

- To correlate the heater resistance with the heater temperature.
- To correlate the applied voltage on the heater with the heater temperature.
- To correlate the measured voltage on the thermopiles with the thermopile temperature

The novelty in this new approach is the way to obtain the relation between the resistance and the heater temperature. In our case, three calibrant particles (cf. Figure 3.8) are placed altogether, as close as possible to one of the thermopiles. After that, a voltage ramp is performed. At this moment there is no relation between the resistance and the heater temperature, so the values registered as heater temperature provide just the corresponding resistance values. The output file of the measurement can be exported to any data analysis software (e.g., Igor Pro).third order polynomial equation the heater temperature as a function and stored in the calibration file.

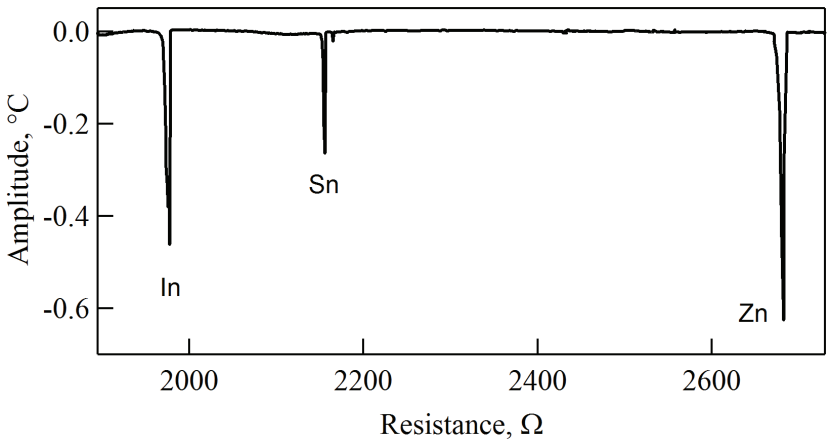

Figure 3.8 – Heating curve showing the melting points of the calibrant particles placed on the sensor.

This approach is more accurate and considerably faster than the one used on Ref. [9].

This new calibration procedure has been given to the micro/nano-focus ID13 beamline staff at ESRF as part of the set-up of the nanocalorimeter as a new equipment for the beamline.

3.3 Thermal gradients across the nanocalorimetric sensors

In this section, we describe the method to quantify the thermal gradients built across the membrane during various temperature programs using different sensors. XEN-39392 (cf. Figure 3.9a) are standard SiN whereas XEN-39399 (cf. Figure 3.9b) are also SiN membrane sensors but with a polycoating layer to improve thermal gradients across the membrane.

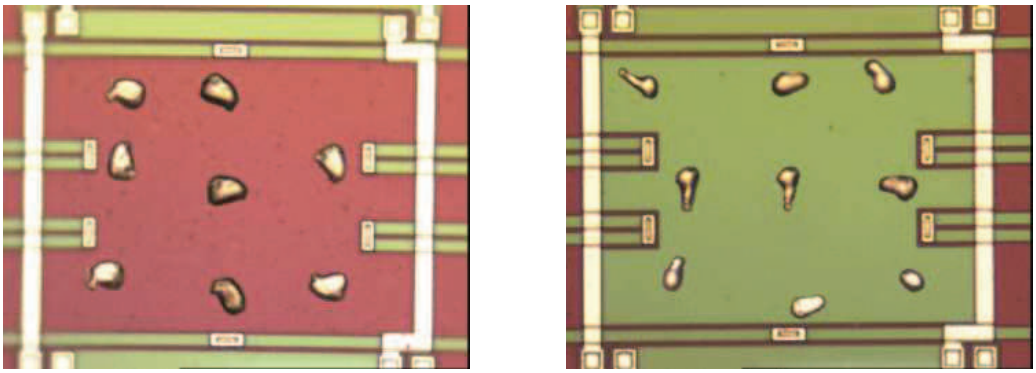

(a) XEN-39392 sensor. (b) XEN-39399 sensor.

Figure 3.9 – Indium particle positions used for thermal gradient experiments.

In our heating experiments with explosives particles, sensors showed differences in the melting onset of 20-25 °C, depending on where exactly the particles were placed. Following the method described in Ref. [10], we evaluated the gradients by measuring the melting point onset of a micro-particle of In placed at different positions within the active area. Figure 3.9 displays a composition for the different positions where the same indium particle was

placed. what it is said on the Xensor website, using XEN-39399 sensors do not improve significantly the thermal gradient.

The described experiment is rather laborious because the same particle had to be placed at different positions, which is not an easy task when the working area is only 100 µm in size. Thus, in order to have more points, we supposed that the sensors are both horizontally and vertically symmetrical (cf. Figure 3.10).

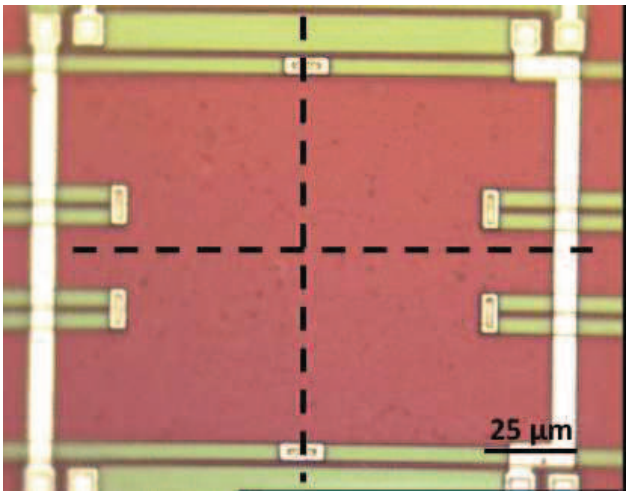

Figure 3.10 – Supposition of symmetry for studies of the thermal gradients.

temperature difference between the theoretical melting point of Indium and the experimental one through the whole sensor surface. As it can be seen, close to the heaters indium melts at lower temperatures because these two zones are hotter than other zones. The gradient is consistent with the idea given by Minakov et al [11] where they stated this type of distribution on smaller sensors. Figure 3.13, it is clear why there is an increase on the melting onset temperature on some regions of the membrane. The reason is that the heat flux spread radially from the finite stripes.

The resulting 2D temperature maps are shown in Figure 3.11 and in Figure 3.12. These results correspond to the XEN-39392 sensors, although practically same results were obtained using XEN-39399 sensors. The isotherm lines show the temperature difference between the theoretical melting point of Indium and the experimental one through the whole sensor surface. It can

be seen that in the AC mode at 20 °C min^{-1} (cf. Figure 3.11) the temperature in the center of the active area is relatively uniform, increasing only in the vicinity of the heating stripes, i.e. at the top and bottom of the figure. By contrast, during a fast DC ramp (1000 °C s^{-1}), the temperature non-uniformity is more noticeable even in the center of the active area. Therefore, it is crucial to control the sample position when such large-area sensors (XEN-39392 are 100×100 μm^2) are used in the experiments. The gradient maps will be used further in this work to correct the temperature discrepancies for the thermal events studied.

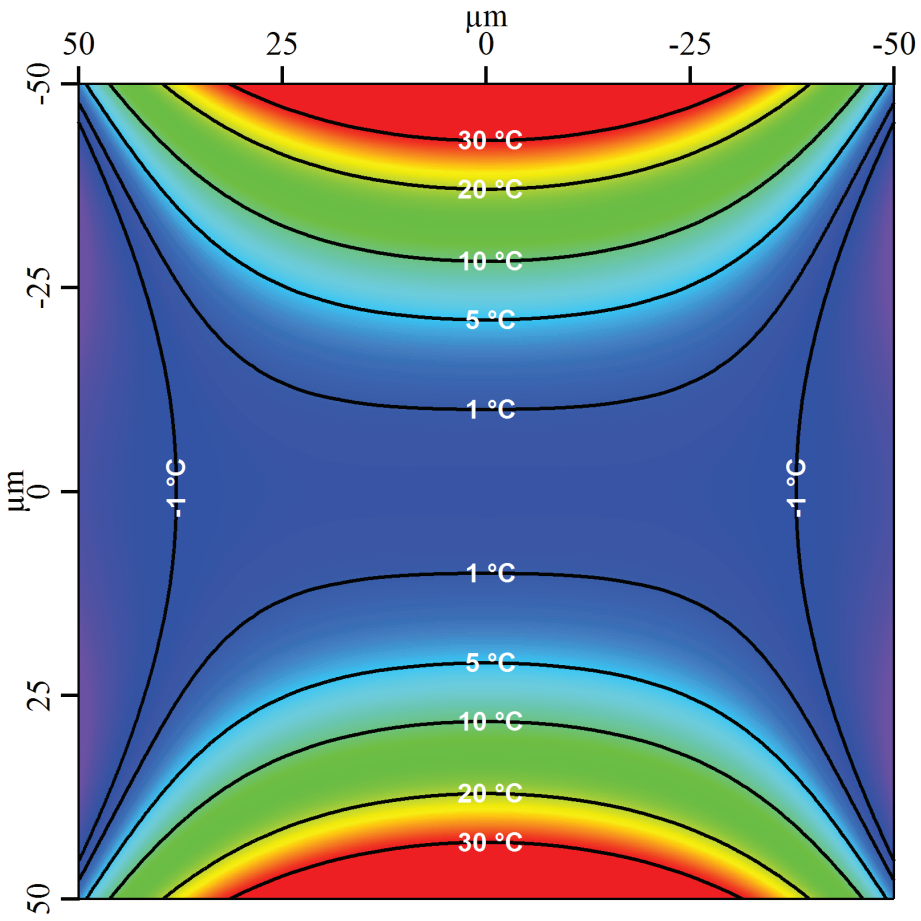

Figure 3.11 – Temperature-gradient map corresponding to heating in the AC mode.

Those gradients are consistent with the idea given by Minakov et al. [11]

where they stated this type of distribution on smaller sensors. If one considers that the two heating stripes of the sensor form a sphere of heated air as it is depicted in Figure 3.13, it is clear why there is an increase on the melting onset temperature in some regions of the membrane. The reason is that the heat flux spreads radially from the finite stripes.

In Appendix A, there are different thermal maps performed on XEN-39392 sensors using different heating rates ranging from 125 to 4000 °C s^{-1}.

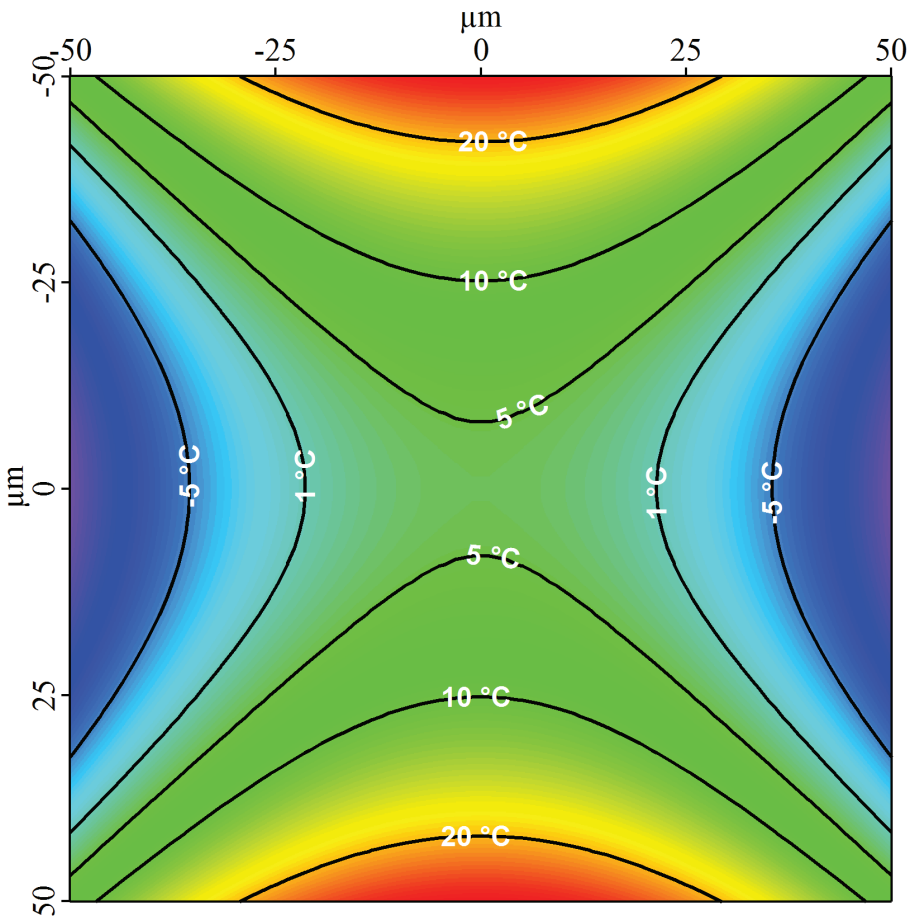

Figure 3.12 – Temperature-gradient map in the DC mode at 1000 °C s^{-1}.

3.4 High-resolution thermal imaging with a combination of nano-focus X-ray diffraction and ultra-fast chip calorimetry

Published in Journal of Synchrotron Radiation, **2013**, *21*, 1, 223-228

Abstract

A microelectromechanical-systems-based calorimeter designed for use on a synchrotron nano-focused X-ray beamline is described. This instrument allows quantitative DC and AC calorimetric measurements over a broad range of heating/cooling rates ($\leqslant$ 100000 Ks^{-1}) and temperature modulation frequencies ($\leqslant$ 1 kHz). The calorimeter was used for high-resolution thermal imaging of nanogram-sized samples subjected to X-ray-induced heating. For a 46 ng indium particle, the measured temperature rise reaches $\sim$ 0.2 K, and is directly correlated to the X-ray absorption. Thermal imaging can be useful for studies of heterogeneous materials exhibiting physical and/or chemical transformations. Moreover, the technique can be extended to three-dimensional thermal nanotomography.

Introduction

The generation of heat during X-ray beam materials irradiation has found applications ranging from single-photon detection for X-ray spectroscopy [12] to non-invasive thermal imaging for identification of beam damage [13]. X-ray-induced heating has also been used for creation and diagnosis of a solid-density plasma [14] and for controlled decomposition of the energetic materials [15]. Generally, it is clear that the evaluation of the X-ray-induced heat can provide material-specific information because the interaction cross sections of the X-ray photons, such as those due to photoelectric, Rayleigh and Compton contributions, depend on the atomic number and sample mass density. Previously, several studies [cf. [13], and references therein] focused

on the quantitative evaluation of beam-induced temperature rise. In particular, computations were performed for the case of a typical biocrystal sample exposed to fluxes of third-generation synchrotron radiation sources operated at photon energies typical for the crystallographic work (12 keV). It was found that the temperature rise in samples generally stays small, varying from a fraction of a degree to a couple of degrees, which is explained by the low total X-ray beam power (1–4 mW) and low density of organic materials. Because of the small rise in the temperature of such samples, measurement of X-ray-beam-induced heating employing conventional non-invasive thermal imaging is challenging. Here, we show that the use of advanced microelectromechanical systems (MEMS)-based nanocalorimeters in combination with nano-focused X-ray beams [16] helps to alleviate this problem and allows thermal mapping of extremely small samples (1–100 ng in weight) with micrometre spatial resolution. It is noteworthy that nano-focused X-ray beams have recently proved to be very helpful in elucidating the local-scale structure of semicrystalline polymers [17, 18].

MEMS-based calorimetric sensors capable of performing quantitative thermo-analytical measurements on extremely small samples were first introduced in the 1990s by L. Allen [1]. One of the first commercially available MEMS sensors produced by the Xensor company (TCG 3880) reached a sensitivity of 1 nJK^{-1} and a time resolution of 5 ms [2]. The approaches toward quantitative nanocalorimetric experiments were developed further by M. Merzlyakov [19] and C. Schick [7]. In our group, an electronic interface for a nanocalorimeter was built which is compatible with different types of commercial calorimetric sensors and allows operation in both DC and AC modes [20]. The instrument is capable of conducting quantitative DC and AC calorimetric measurements over a broad range of heating/cooling rates ($\leqslant$ 100000 Ks^{-1}) and temperature modulation frequencies ($\leqslant$ 1 kHz). Despite the existence of commercial chip calorimeters such as Flash DSC from Mettler Toledo, our own nanocalorimeter was specially designed to simplify synchrotron measurements; the measuring cell of the Flash DSC instrument is fixed directly on top of the electronic interface which prevents any *in situ* combination of calorimetric measurements with X-ray diffraction in transmission. Moreover, commercial instruments do

not support AC calorimetric measurements, which is crucial for compatibility with a relatively slow technique like X-ray diffraction. In general, the open design of our nanocalorimeter makes the combination of our system with other physical characterization techniques rather straightforward [9].

Experimental

A schematic of the experimental set-up used in this study is shown in Fig. 3.13. The *in situ* calorimetric measurements were performed with the help of a MEMS-type sensor consisting of a thin suspended silicon nitride membrane with assembled electric heaters and thermopiles (*cf.* Fig. 3.13, top). The guard heater was used for linear heating and cooling ramps, whereas the modulation heater allowed for temperature modulation experiments. In the course of the measurements, the heaters generate a small sphere of heated air around them, which facilitates heat exchange with the sample deposited on the membrane. The calorimetric experiments are enabled by an electronic interface, which applies the programmed voltage pulses to the heaters and allows for fast thermopile readout.

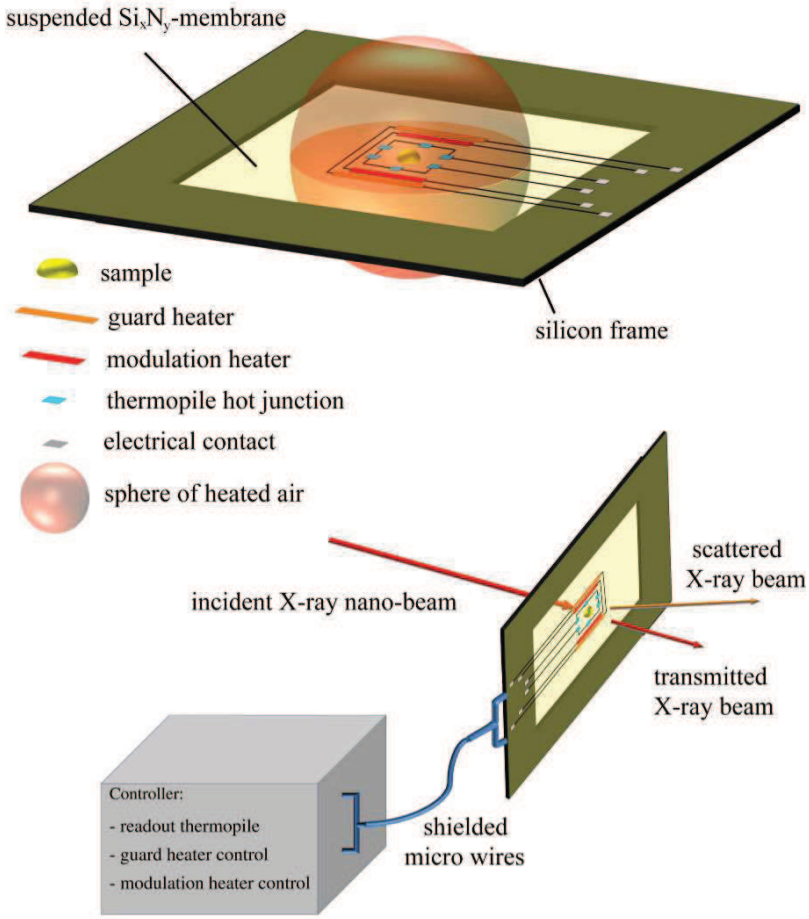

Figure 3.13 – Schematics of the nanocalorimeter set-up used for in situ nano-focus X-ray beam measurements. The nanocalorimeter sensor (top) consists of a silicon frame with a thin suspended silicon nitride membrane on which are assembled two pairs of electric heaters (the so-called modulator and guard heaters) as well as six thermopiles connected in series. The calorimetric experiments are realised with the help of a custom-built electronic controller.

The nano-beam X-ray diffraction measurements were carried out at the ID13 beamline [cf. Fig. 3.13, bottom and Fig. 3.14a] of the European Synchrotron Radiation Facility (ESRF; Grenoble, France). A flat Si-based nanocalorimetric MEMS-type sensor is mounted on a perforated flat ceramic plate (Fig. 3.14b) allowing for X-ray measurements in transmission. The Si_xN_y membrane of the XEN-39392/XEN-40014 sensor employed has a lat-

eral size of 900×900 µm^2 and is only 1 µm thick; it is therefore practically transparent for the X-ray beam. Two pairs of resistive heating elements and six differential thermopiles connected in series constitute the active area of 100×100 µm^2 (Fig. 3.14c).

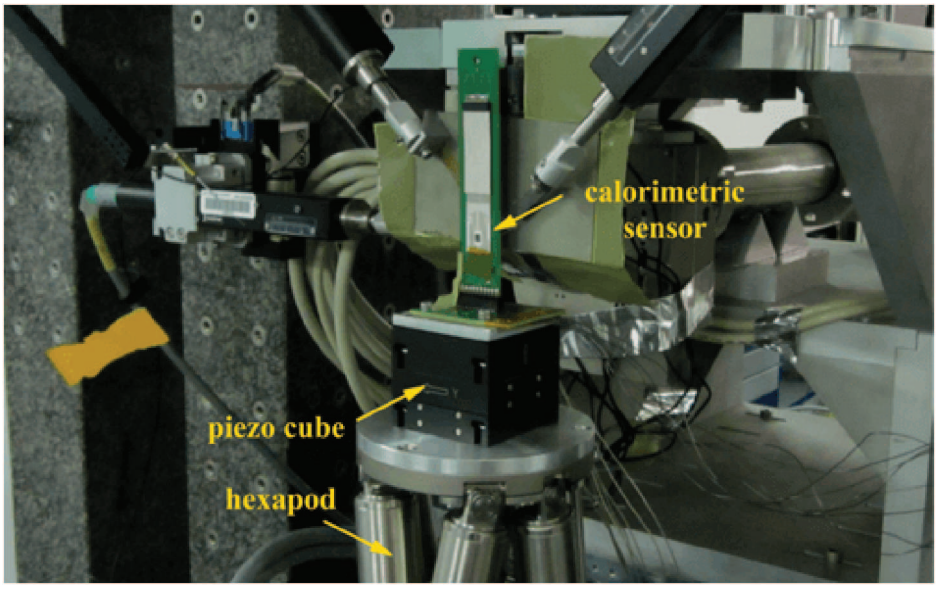

(a) View of the sample stage at the ID13 nano-hutch facility at the ESRF with the nanocalorimetric sensor holder installed. The sensor is positioned vertically on top of a piezo-actuator (black cube) to allow the scanning of the region of interest with nanometre resolution.

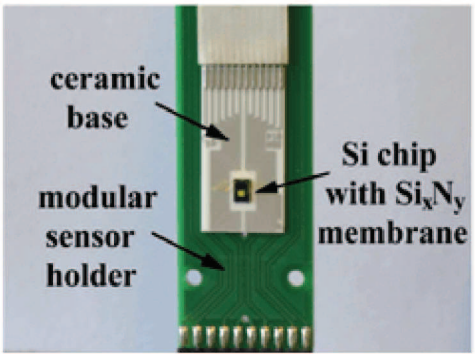

(b) Closer view of the custom-made modular sensor holder. The nanocalorimetric sensor is mounted onto a flat ceramic base compatible with X-ray diffraction in transmission.

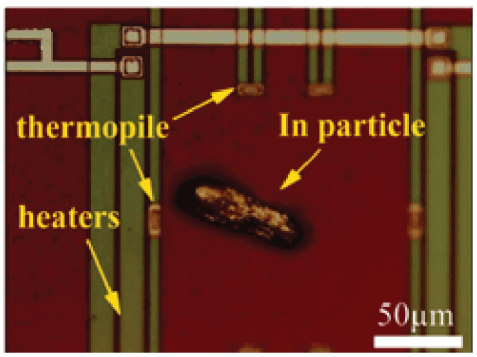

(c) A micron-sized In particle placed on the active area of the nanocalorimetric sensor. The heating elements and hot junctions of the thermopile are in close vicinity of the particle.

Figure 3.14 – Nanocalorimeter set-up on ID13 beamline at ESRF.

The low heat conductivity and low heat capacity of the Si_xN_y membrane are crucial in reaching the required sensitivity to nanogram-sized samples. For the X-ray absorption and nano-diffraction experiments, X-ray photons with an energy of 14.92 keV were used. The final footprint of the beam on the sample of about 150×150 nm^2 was achieved using nano-focusing refractive X-ray lenses with a focal distance of 14 mm [21]. The size of the beam is the main parameter defining the spatial resolution of the nano-beam X-ray diffraction measurement. The two-dimensional diffraction patterns were collected using a two-dimensional Frelon N4 camera with 50 µm × 50 µm pixels. The norm of the scattering vector s $[s = 2sin(\theta)/\lambda]$ was calibrated using several reflections of corundum. The X-ray absorption data were recorded using an X-ray-sensitive diode placed 60 cm downstream of the sample. The absorption data signal was corrected for absorption of the X-ray beam in the air and in the bare silicon nitride membrane.

In this study, *in situ* nano-focus X-ray diffraction combined with MEMS-based nanocalorimetry was performed on a single micrometre-sized indium particle (Strem Chemicals, purity 99.999%). This material was selected for thermal imaging due to its high absorption (mass attenuation coefficient μ/ρ of $\sim$ 44.45 cm^2g^{-1} at 15 keV) and its well known thermodynamic parameters; it is conventionally used as a thermal calibrant for differential scanning calorimetry (DSC). During the measurements, the sensor was operated exclusively in the AC mode, where a small current (current amplitude 0.1 mA, current offset 0.3 mA) oscillating at a frequency of $\sim$ 40 Hz is applied to the heating elements while performing experiments at constant heating rates or in quasi-isothermal conditions [16]. This operation mode is similar to the conventional modulated DSC technique [22]. In this mode, the sample is subjected to heating power oscillations while its temperature response is measured. In our case, by passing a small oscillating current through the heating elements we generate thermal power, which results in small periodic temperature oscillations making it possible to measure the sample heat capacity [23].

Discussion

For the thermal imaging, a microparticle of In was positioned within the active area of the calorimetric sensor with the help of a micromanipulator (Fig. 3.14c). During the experiment it was visualized with a slide-in on-axis optical microscope in reflection. The particle was exposed to either 2 s or 20 s of pulsed incident X-ray radiation (Fig. 3.15, top).

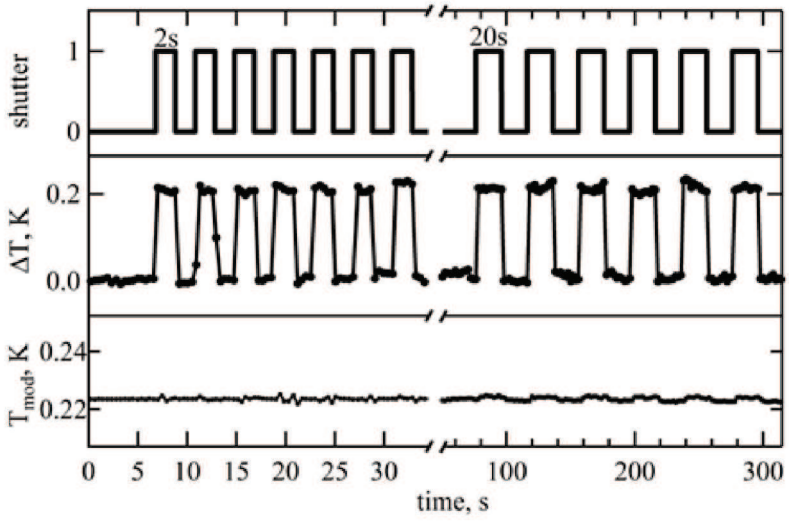

Figure 3.15 – Room-temperature experiment showing the heating effect of a nano-focused X-ray beam modulated by a sequence of fast-shutter openings (top). Variation of the In particle temperature (middle) and temperature modulation amplitude (bottom).

The calorimeter measured an increase of about 0.2 K, closely following the sequence of the X-ray beam exposures (Fig. 3.15, middle). Importantly, the measured temperature increase is independent of the X-ray pulse length. In this case, the power provided by the X-ray beam exposure becomes very rapidly compensated by the heat losses through the atmosphere, as will be described later in the text. The rate at which the thermal equilibrium is reached is comparable with the characteristic time of the calorimetric sensor, which equals approximately 4 ms. Therefore the temperature rise (cf. Fig. 3.16) rarely shows any middle points; the latter can appear only accidentally, due to a slightly asynchronized data acquisition. For both temperature

values (i.e. with and without the X-ray beam switched on) the noise levels are comparable; thus, for the sequence of 20 s pulses they equal 7.8 and 8.3 mK, respectively. Importantly, the amplitude of the temperature modulation (T_{mod}) exhibits no visible change in these conditions (Fig. 3.15, bottom).

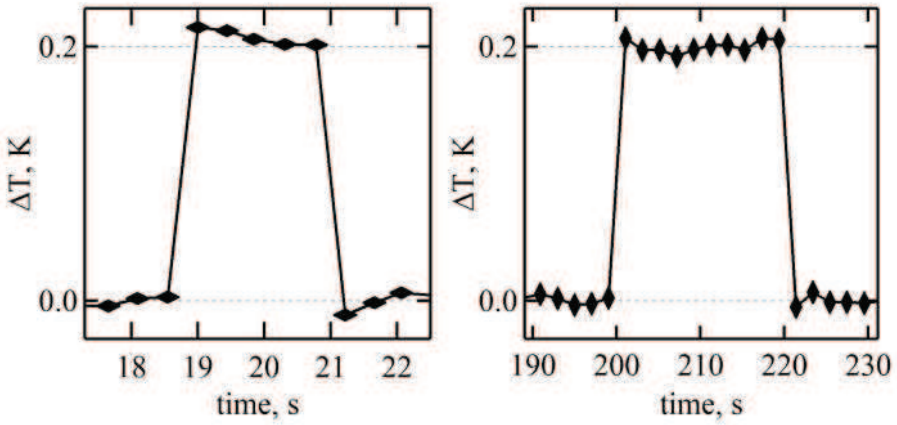

Figure 3.16 – Zoomed segments of the temperature profile due to individual X-ray pulses of 2 and 20 s (left and right, respectively).

The analysis of the T_{mod} values can be performed with a simple model employed for interpretation of the modulated DSC data (Jiang et al., 2002; Kraftmakher, 2002). It is assumed that the oscillating power with amplitude P is consumed heating the sensor with a loaded sample having the total heat capacity at constant pressure $C_{p,sample} + C_{p,membrane}$, as well as for the heat exchange with the atmosphere characterized by the power exchange coefficient Q [20, 23],

$$T_{mod} = \frac{P}{\sqrt{\left[(C_{p,sample} + C_{p,membrane})\omega\right]^2 + Q^2}} \tag{3.4.1}$$

where Q is the proportionality coefficient between the applied power and the temperature rise of the sensor. The constancy of T_{mod} during the experiment shows that, under these conditions, i.e. far away from the phase transitions, the sample heat capacity is not affected by the incident X-ray beam. Moreover, by comparing the T_{mod} values measured for the unloaded

and loaded sensor and by using the experimental heat exchange coefficient Q (59.0 mW K^{-1}), $C_{p,sample}$ was calculated to be 12.9 nJ K^{-1}. This corresponds to a sample weight of 56 ng.

In Fig. 3.17 top-left, a two-dimensional map of the In particle was generated with a 2 mm lateral resolution using the scattered intensity of a single 110 crystalline reflection of In (cf. inset of Fig. 3.17 top-left). The spatial distribution of the scattering intensity nicely reproduces the particle shape, as observed optically (cf. Fig. 3.14c). This unambiguously shows that the particle has a single-crystalline nature. Fig. 3.17 bottom-left shows the spatially resolved X-ray absorption for the same particle.

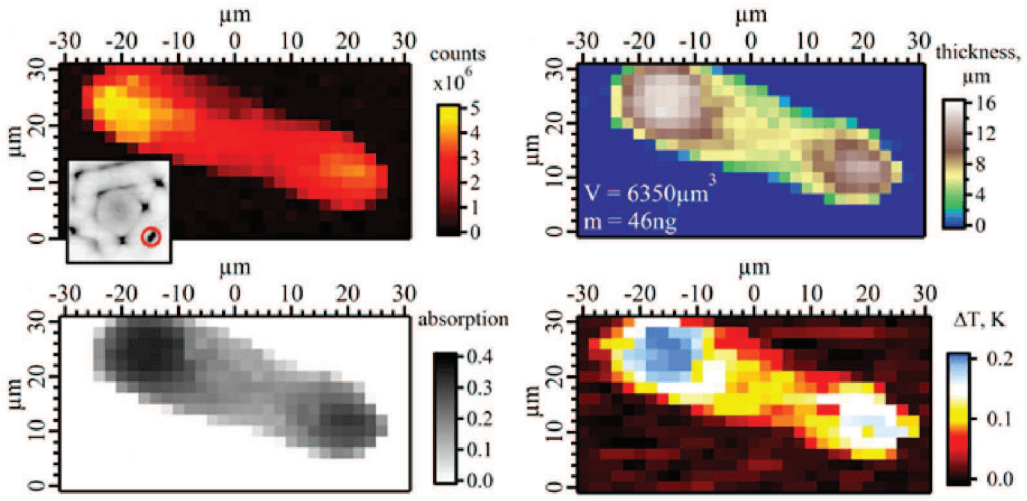

Figure 3.17 – (top-left) Image of the same In particle as in Fig. 3.14c obtained by mapping the intensity of a selected 110 reflection of In (encircled on the two-dimensional WAXS pattern in the inset). The pixel size is 2×2 µm^2. (bottom-left) Image of the particle obtained using absorption of the incident X-ray beam. (top-right) Topographical map of the particle recalculated from the absorption image given in the bottom-left image. (bottom-right) Rise of the particle temperature due to the incident X-ray beam plotted as a function of the spatial position.

The classical expression for the intensity of transmitted light is

$$I_x = I_0 \exp[-(\mu/\rho)\rho x] \tag{3.4.2}$$

where I_0 is the incident beam intensity, I_x is the intensity of the transmitted beam after passing through a slab of material of thickness x, ρ is the mass density of the material and μ/ρ is the mass attenuation coefficient. When the absorption $A = (I_0/I_x)/I_0$ is known, the local thickness of the particle can be derived from equation 3.4.2 (cf. Fig. 3.17 top-right). The resulting thickness map permits the calculation of the total volume and mass of the particle, which equal 6350 μm^3 and 46 ng, respectively. The latter value is in reasonable agreement with the one computed previously from equation 3.4.1.

By measuring the sample temperature rise (ΔT) due to absorption of the nano-focused X-ray beam, the temperature distribution map of the particle was generated (cf. Fig. 3.17 bottom-right). It can be seen that the thermal image reproduces the shape of the particle. If one assumes full conversion of the absorbed photon energy to heat followed by rapid thermal equilibration, the ΔT value can be expressed as follows,

$$\Delta T = \frac{(I_0/I_x)U}{Q\Delta t} \qquad \text{or} \qquad \Delta T = \frac{W_{beam}}{Q}A \tag{3.4.3}$$

In equation 3.4.3, U is the energy of one photon, Δt is the beam exposure time excluding the detector read-out time and W_{beam} is the X-ray beam power (29.2 μW).

To validate the hypothesis underlying equation 3.4.3, the ΔT values were correlated to the local X-ray absorption. For the sake of clarity, the comparison is firstly given for one cross section of the respective maps in Fig. 3.18a, showing good correspondence between them. Then, the statistic correlation is displayed for all data points in Fig. 3.18b. From the last figure, it can be concluded that there is indeed a linear correlation of the sample temperature rise to the spatially resolved absorption. Moreover, the slope of the linear fit shown on the graph (0.53) is reasonably close to the expected value of 0.49 [cf. equation 3.4.3]. The standard deviation of the temperature residual gives the upper bound for the temperature noise (15 mK), which after conversion to power gives the instrument power sensitivity of 900 nW.

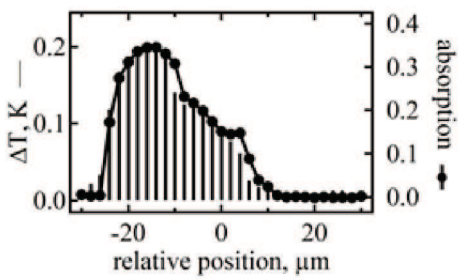

(a) The horizontal cross section of the temperature map in Fig. 3.17 bottom-right is given as vertical sticks and that of the X-ray absorption in Fig. 3.17 bottom-left shown as filled circles.

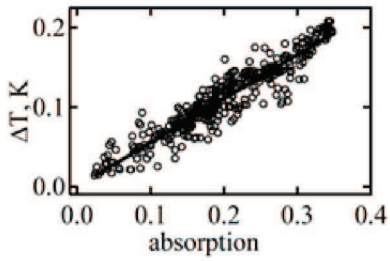

(b) Increase of the In particle temperature as a function of the X-ray beam absorption for the whole scanned area. The solid line is the linear fit to the data. Both cross sections correspond to the line y = 25 µm.

Figure 3.18 – Local X-ray absorption of the In particle shown in Fig 3.17.

Fig. 3.19 displays the results of simultaneous nanocalorimetric and X-ray diffraction experiments performed on the same In particle either during heating and cooling ramps at a constant heating rate or during quasi-isothermal measurements. Thus, the one-dimensional-reduced WAXS diffractograms recorded as a function of temperature distinctly show the onset of melting/crystallization transitions occurring at 430.0 ± 0.75 and 429 ± 0.75 K, respectively (see Fig. 3.19a). This shows that the developed nanocalorimetric accessory can be conveniently used as a normal heating stage for nano-focus X-ray diffraction. Moreover, the melting transition of In is clearly visible on the calorimetric temperature-modulation curve in Fig. 3.19b, where it is identified as a negative peak. The decrease of T_{mod} in this region corresponds to an increase in the complex heat capacity of the sample in the melting region [cf. equation 3.4.1], which is a typical observation in the modulated DSC experiments [22].

After the sample is completely molten, the modulation amplitude increases again. The selected two-dimensional WAXS diffractograms given on the same figure panel show that the initially highly crystalline sample (T = 420 K) starts to display a mixture of crystalline reflections and amorphous halo at 430 K, before becoming completely molten at 433 K. The observed co-existence

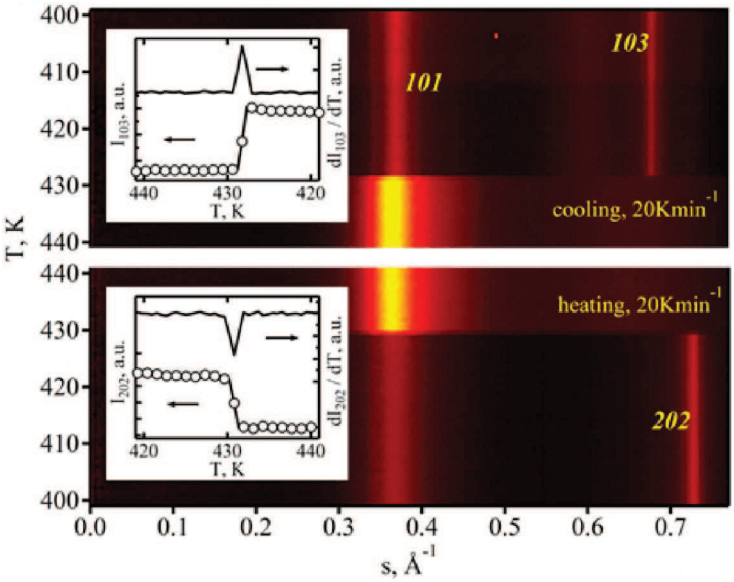

(a) 1D-reduced WAXS curves measured in the temperature range from 400 to 440 K at a rate of 20 K min^{-1}. The insets show diffraction intensities and their first derivatives for the 202 reflection (heating ramp) and 103 reflection (cooling ramp).

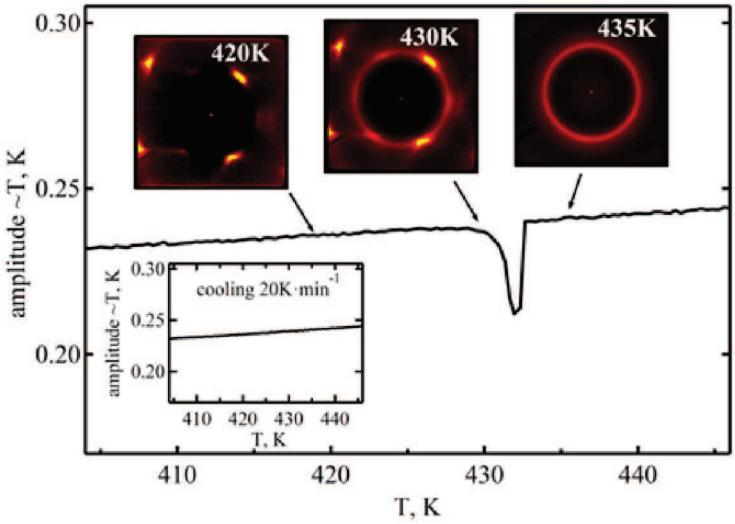

(b) Amplitude of the temperature modulation recorded simultaneously with X-ray diffraction for the heating ramp. The inset gives the curve corresponding to cooling and two-dimensional WAXS patterns measured at different temperatures.

Figure 3.19 – Simultaneous nanocalorimetric and X-ray diffraction experiments on an In particle.

of crystalline and amorphous fractions in the diffractograms of In recorded over a finite temperature range is not usual since this material melts and crystallizes very rapidly. Such co-existence can only be accounted for by repeated melting/recrystallization events occurring during thermal modulation cycles whose peak-to- peak amplitude is, in this case, approximately 0.4 K. Since the rate of the WAXS detector recording is much slower than the modulation frequency applied, the CCD camera receives a time-averaged view of the sample state. Interestingly, the modulated cooling curve does not reveal the crystallization transition, although it is safely detected by X-rays. The latter fact can be explained by the high rate of this process, whose characteristic time is much smaller than the duration of one cycle.

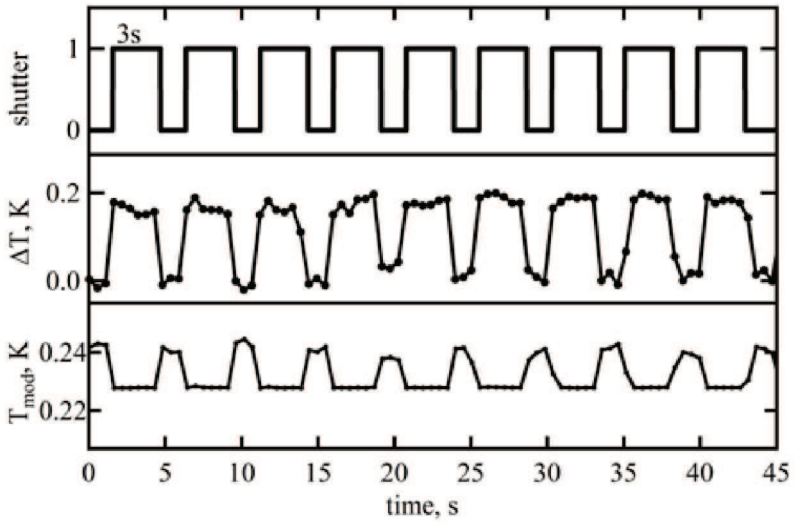

Figure 3.20 – Quasi-isothermal experiment at 430 K showing the heating effect of a fast-shutter-modulated X-ray beam (top). The resulting variation of the particle temperature and modulation amplitude is shown in the middle and bottom panels, respectively.

The heating effect of the X-ray beam measured at the verge of melting (Fig. 3.20) is similar to the one at room temperature (cf. Fig. 3.15). However, the amplitude modulation signal shows a qualitatively different behaviour. Thus, in this case the fast-shutter openings are accompanied by a noticeable decrease of T_{mod}. This can be explained by the fact that heating of the

sample with the X-ray beam brings it further into the melting region, where T_{mod} is reduced for the reasons explained before. Thus, the dynamic thermal response of the sample (i.e. T_{mod}) measured in quasi-isothermal conditions during X-ray beam exposures can provide additional information on the phase transitions occurring in the sample.

Conclusions

In summary, we report on a newly designed ultra-fast MEMS-based calorimeter accessory for synchrotron nano-focused X-ray diffraction. The instrument allows quantitative DC and AC calorimetric measurements in a broad range of heating/cooling rates ($\leqslant$ 100000 Ks^{-1}) and temperature modulation frequencies ($\leqslant$ 1 kHz). Here we performed quantitative thermal imaging of a nanogram-sized metal sample exposed to an X-ray beam. We show that the resulting temperature rise is correlated with spatially resolved X-ray absorption. In the future, similar thermal imaging can be extended to organic materials such as single bio-crystals, which also show temperature rise upon irradiation with X-rays. However, in this case, special care will be required to minimize beam-induced degradation.

For the case of inert homogeneous materials such as microparticles of In, the thermal mapping provides information similar to thickness images. However, the thermal imaging at elevated temperature, which combines measurements of the static temperature rise and temperature modulation amplitude, can provide information on the sample thermal behaviour. One can imagine that the temperature signal can be collected simultaneously with X-ray absorption during the standard nanotomography experiments. We expect that thermal imaging in three dimensions (thermal nanotomography) can help guide studies of heterogeneous materials exhibiting physical (e.g. phase transitions) and chemical (e.g. curing reactions) transformations at different temperatures.

3.5 Chapter conclusions

This chapter is focused on describing the Nanocalorimetry technique.

Although the originality of the calibration procedure remains the same, the modification done to the procedure permits an improvement in both accuracy and overall speed. A particular issue related with the sensors is addressed in the chapter and the followed strategy to overcome it. Sensors must be annealed before use in order to gain reproducibility in the experiments. Measurements of thermal gradients across the active area of XEN-39392 and XEN-39399, both with an active area of 100×100 μm^2, are performed using an indium particle as a probe. We observe that the melting temperature of an indium particle measured using our nanocalorimeter is depending on the position where the particle is placed.

An accessory for simultaneous in-situ nanocalorimetric measurements and synchrotron nano-focused X-ray diffraction is described. The uniqueness of this accessory is that the sensor holder is physically separated from the controller allowing to make X-ray scattering experiments in transmission. The setup meets the requirements imposed by the sample environment of the beamlines in terms of spatial constraints, rigidity of electrical connections and weight.

[1] L. Allen, G. Ramanath, S. Lai, Z. Ma, S. Lee, D. Allman, K. Fuchs, *Applied physics letters* **1994**, *64*, 417–419.
[2] A. Minakov, S. Adamovsky, C. Schick, *Thermochimica Acta* **2005**, *432*, 177–185.
[3] S. Lai, J. Guo, V. Petrova, G. Ramanath, L. Allen, *Physical Review Letters* **1996**, *77*, 99.
[4] H. Jiang, K.-s. Moon, H. Dong, F. Hua, C. Wong, *Chemical Physics Letters* **2006**, *429*, 492–496.
[5] F. De Santis, S. Adamovsky, G. Titomanlio, C. Schick, *Macromolecules* **2006**, *39*, 2562–2567.
[6] A. Minakov, A. Van Herwaarden, W. Wien, A. Wurm, C. Schick, *Thermochimica Acta* **2007**, *461*, 96–106.
[7] A. Minakov, C. Schick, *Review of Scientific Instruments* **2007**, *78*, 073902–073902.
[8] E. Gmelin, S. Sarge, *Pure and applied chemistry* **1995**, *67*, 1789–1800.
[9] N. Piazzon, PhD thesis, Université de Haute Alsace, Mulhouse, **2010**.
[10] C. Simon, M. Peterlechner, G. Wilde, *Thermochimica Acta* **2015**, *603*, 39–45.
[11] A. Minakov, J. Morikawa, T. Hashimoto, H. Huth, C. Schick, *Measurement Science and Technology* **2006**, *17*, 199.
[12] D. McCammon, S. Moseley, J. Mather, R. Mushotzky, *Journal of applied physics* **1984**, *56*, 1263–1266.
[13] E. Snell, H. Bellamy, G. Rosenbaum, M. van der Woerd, *Journal of synchrotron radiation* **2006**, *14*, 109–115.
[14] S. Vinko, O. Ciricosta, B. Cho, K. Engelhorn, H.-K. Chung, C. Brown, T. Burian, J. Chalupský, R. Falcone, C. Graves, et al., *Nature* **2012**, *482*, 59–62.
[15] B. Beard, *Propellants explosives pyrotechnics* **1991**, *16*, 81–87.
[16] A. Minakov, S. Roy, Y. Bugoslavsky, L. Cohen, *Review of scientific instruments* **2005**, *76*, 043906–043906.
[17] M. Rosenthal, G. Bar, M. Burghammer, D. Ivanov, *Angewandte Chemie International Edition* **2011**, *50*, 8881–8885.
[18] M. Rosenthal, G. Portale, M. Burghammer, G. Bar, E. T. Samulski, D. Ivanov, *Macromolecules* **2012**, *45*, 7454–7460.
[19] M. Merzlyakov, *Thermochimica acta* **2006**, *442*, 52–60.
[20] N. Piazzon, M. Rosenthal, A. Bondar, D. Spitzer, D. Ivanov, *Journal of Physics and Chemistry of Solids* **2010**, *71*, 114–118.
[21] P. Boye, J. Feldkamp, J. Patommel, A. Schwab, S. Stephan, R. Hoppe, C. Schroer, M. Burghammer, C. Riekel, A. van der Hart, et al. in

Journal of Physics: Conference Series, *Vol. 186*, IOP Publishing, **2009**, p. 012063.

[22] Z. Jiang, C. Imrie, J. Hutchinson, *Thermochimica acta* **2002**, *387*, 75–93.

[23] Y. Kraftmakher, *Physics Reports* **2002**, *356*, 1–117.

Chapter 4

Study of energetic materials

In this chapter, we attempt to explore the potential of nanocalorimetry in the field of detection of energetic materials in the state of micro-particles. To this end, we describe the thermal behavior of single micron-sized particle of these materials (thermal signatures) at different heating rates. To complete the picture, we present the experiments where individual explosive micro-particles exhibit recrystallization. Thanks to the compatibility of our setup with the synchrotron-based diffractometers, the crystallization behavior of some of these materials was studied by coupling nanocalorimetry with nano-focus X-ray diffraction.

4.1 Conventional DSC analysis of standard explosives

In order to understand the behavior of the energetic materials described in Chapter 2, conventional DSC measurements performed at different heating rates were performed. The results of these experiments are given below.

Thermal behavior of HMX

In DSC experiments, high-pressure gold-plated crucibles have been used throughout. All the experiments were made from R.T. to 450 °C using different heating rates: 1, 2.5, 5, 10, 20 and 40 °C min^{-1}, respectively. Figure 4.1 shows the results obtained on the β-HMX samples. The curves presented below show only the decomposition event for the sake of clarity. There is also a small and barely visible endothermic event at ∼200 °C usually attributed to the $\beta \rightarrow \delta$ transition [1].

When looking carefully at the shape of the decomposition peaks in Figure 4.1, one can notice that the conversion corresponding to the maximum of the peak changes with the heating rate. At low heating rates, a shoulder is visible shortly before the decomposition. This behavior could be associated with two acceleratory processes as suggested by Minier et al. [2]. At higher heating rates a change in the shape of the curve is visible. The shoulder is shifted to higher temperatures and becomes masked by the decomposition. It is noteworthy that only at high heating rates signs of melting are detected using conventional DSC. All these results are in good agreement with the data found in the literature [3].

The results obtained are summarized in Table 4.1.

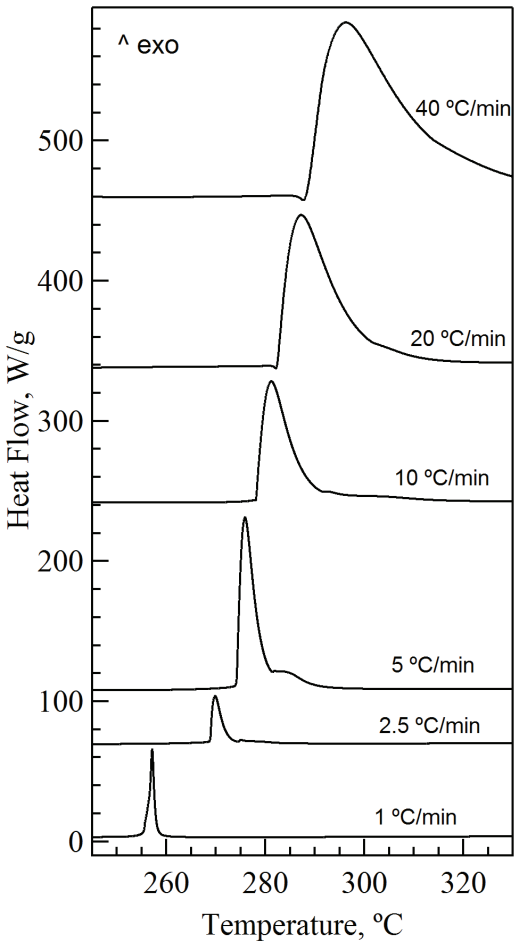

Figure 4.1 – DSC curves corresponding to heating of β-HMX.

Heating rate (°C/min)	Mass (mg)	$\beta \rightarrow \delta$ onset (°C)	$\beta \rightarrow \delta$ enthalpy change (J/g)	Decomposition peak max. (°C)	ΔH_{decomp} (J/g)
1	1.87	187.6	26.7	256.3	3117.6
2.5	0.77	192.4	26.0	272.6	3246.7
5	1.75	195.4	28.6	274.2	3754.3
10	1.25	199.1	24.0	278.1	3216.0
20	1.26	199.1	23.8	282.4	3380.9
40	1.29	200.6	7.8	288.6	3000.2

Table 4.1 – Thermodynamic data from DSC curves on HMX.

For all the conventional DSC experiments performed in this study, the

values obtained for decomposition enthalpies are considerably higher than the ones reported in literature [4–6]. The discrepancies can be atributed to the type of crucibles used to make the experiments. In the literature, the crucibles used are open Pt crucibles.

The activation energy has been calculated by linearly fitting the data of Table 4.1 using both Ozawa (cf. Figure 4.2) and Kissinger (cf. Figure 4.3) equations. These data are summarized in Table 4.7.

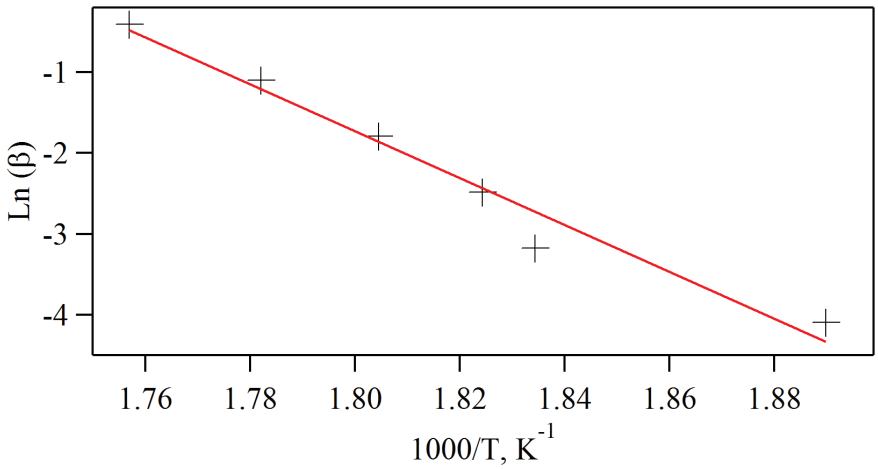

Figure 4.2 – Ozawa plot for heating ramps of HMX.

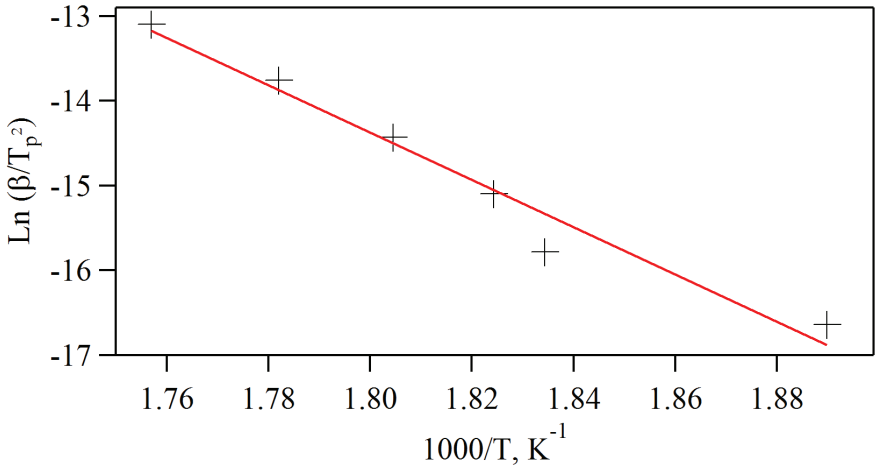

Figure 4.3 – Kissinger plot for heating ramps of HMX.

Although there are quite some discrepancies in the values reported in

literature [4], 197, 444 and 611 kJ mol^{-1}, respectively, the values obtained in our case are within the scatter of these values.

Thermal behavior of RDX

Below we present the curves performed on α-RDX (cf. Figure 4.4). The results obtained are summarized in Table 4.2.

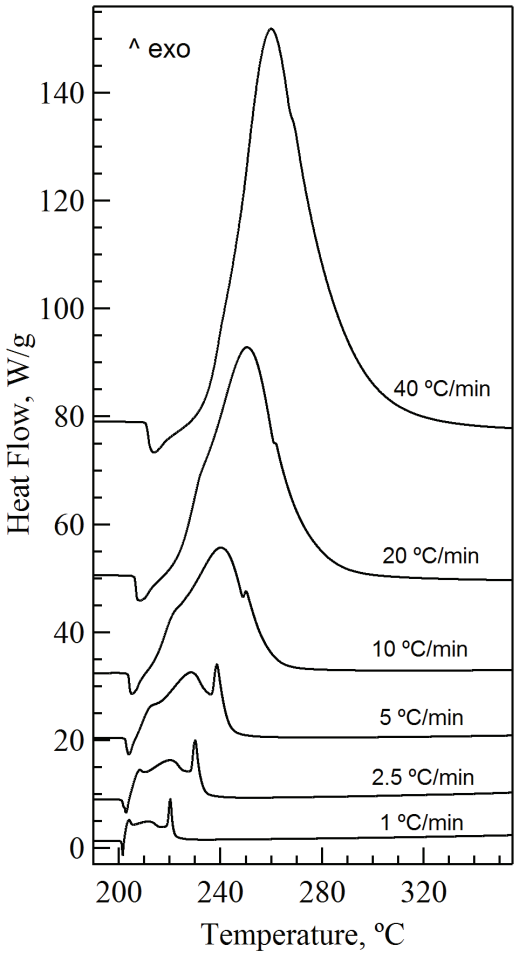

Figure 4.4 – DSC curves obtained on α-RDX.

It can be seen that at low heating rates the decomposition process is not a single-step reaction. Instead, there are clearly two decomposition processes occurring during heating. The second step of this reaction, which is sharper than the first one, is superposed with the first one when the heating rate

is increased. At the highest heating rate tested (40 °C min^{-1}), this second peak is barely visible and the decomposition process is visible as a unique exothermic peak.

Heating rate (°C/min)	Mass (mg)	Melting onset (°C)	Melting enthalpy change (J/g)	Decomposition onset (°C)	ΔH_{decomp} (J/g)
1	1.25	200.2	80.1	204.5	4080.1
2.5	1.25	201.9	96.1	206.3	4136.1
5	1.88	203.9	85.1	209.8	3590.4
10	1.31	203.8	83.9	213.5	3885.5
20	1.36	206.3	95.6	221.2	4066.2
40	2.19	210.7	82.2	238.6	3767.1

Table 4.2 – Thermodynamic data on RDX extracted from DSC curves.

The values obtained for the melting enthalpies are quite below those reported in the literature [7]. Our hypothesis is that due to the proximity with the decomposition process, it is difficult to trace a baseline in order to integrate the curves and to get those values. The decomposition enthalpy values are neither in agreement with the values found in the literature for the same reasons as explained in the case of HMX.

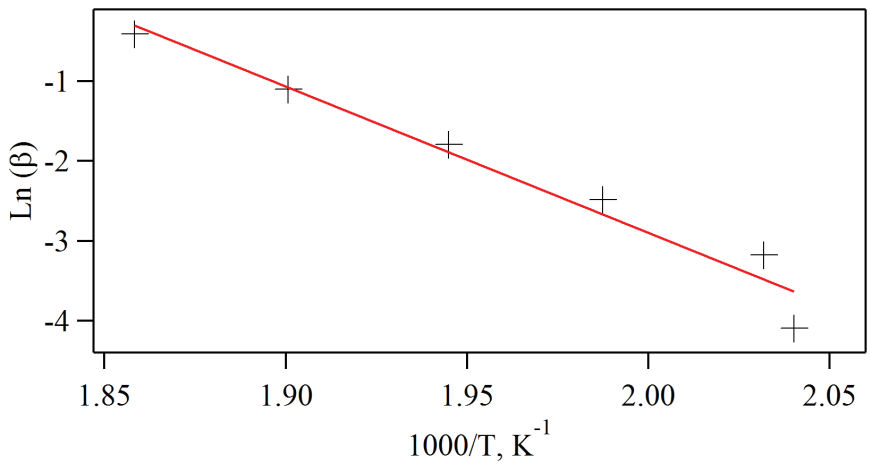

Figure 4.5 – Ozawa plot for heating ramps of RDX.

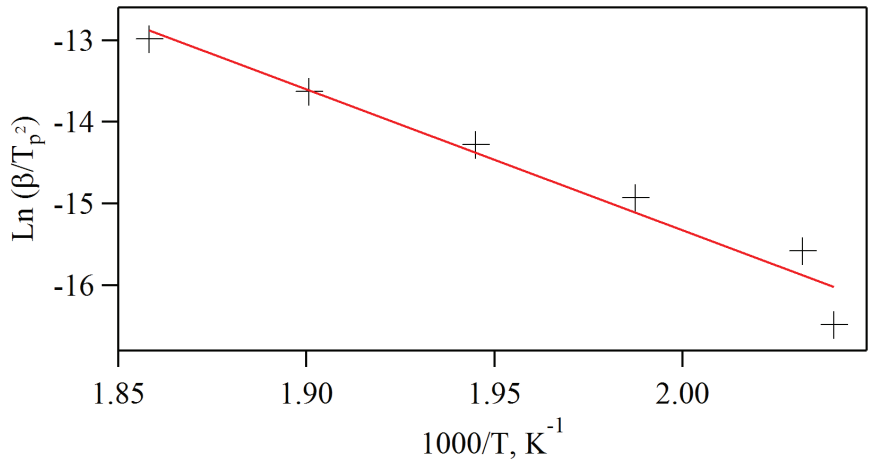

Figure 4.6 – Kissinger plot for heating ramps of RDX.

In the same manner as for HMX, the activation energy has been calculated by fitting linearly the data using both Ozawa (cf. Figure 4.5) and Kissinger (cf. Figure 4.6) plots. The values obtained with both methods, 144.6 and 143.6 kJ mol^{-1}, respectively, are very close to those reported in the literature [4].

Thermal behavior of CL-20

Figure 4.7 shows the heating curves obtained for ϵ-CL-20 samples. As it is stated by Nedelko and coworkers, the decomposition of ϵ-CL-20 is a solid-solid transition [8], so no melting process should be expected on the curves.

A single-stage exothermic decomposition is observed in the temperature range 223-260 °C for heating rates of 1-40 °C min^{-1}. The mentioned temperature range is in good agreement with the data reported in the literature [9].

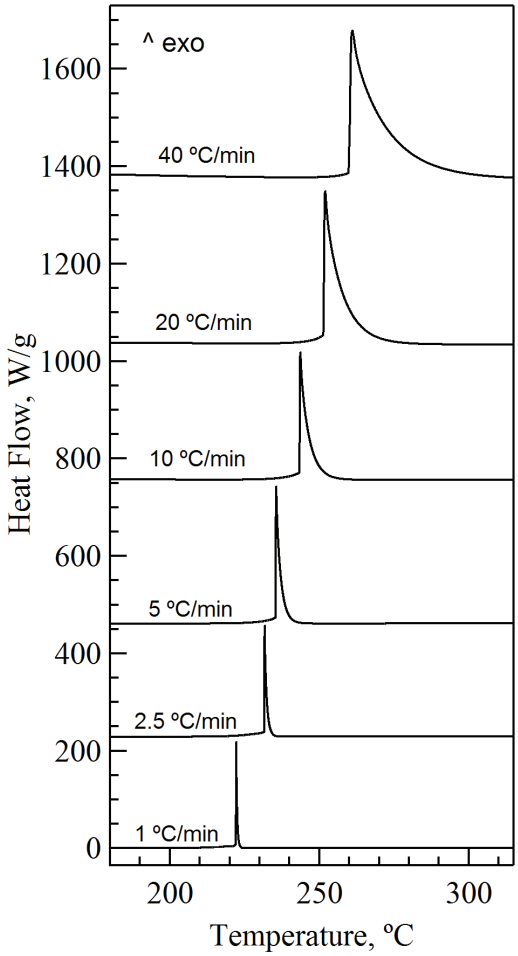

Figure 4.7 – DSC curves obtained for ϵ-CL-20 using high-pressure crucibles.

Heating rate (°C/min)	Mass (mg)	Decomposition peak (°C)	ΔH_{decomp} (J/g)
1	1.32	222.8	6886.4
2.5	0.98	231.7	5204.1
5	1.01	235.4	5990.1
10	0.52	243.4	5001.2
20	0.42	251.4	5642.9
40	0.46	259.9	5260.9

Table 4.3 – Thermodynamic data extracted from the DSC curves on CL-20 in high pressure crucibles.

As with the previously described energetic materials, the values of decomposition enthalpies obtained for the experiments are considerably higher than those reported in the literature [10].

Using aluminum crucibles, the curves obtained are shown in Figure 4.8. In these curves, the shape of the curves are not so rare as in the case of the high pressure crucibles (identical shape independently from the heating rate). The decomposition enthalpy values are almost twice smaller than in the previous case. But they are still higher than the one reported in literature (1980.3 J/g at 10 ℃/min). An explanation for this discrepancy can be attributed to the fact that the value reported by Shen et al. was obtained by using crimped aluminum pans, pierced to allow vapors to escape, and pressed to increase contact between the pan and the sample.

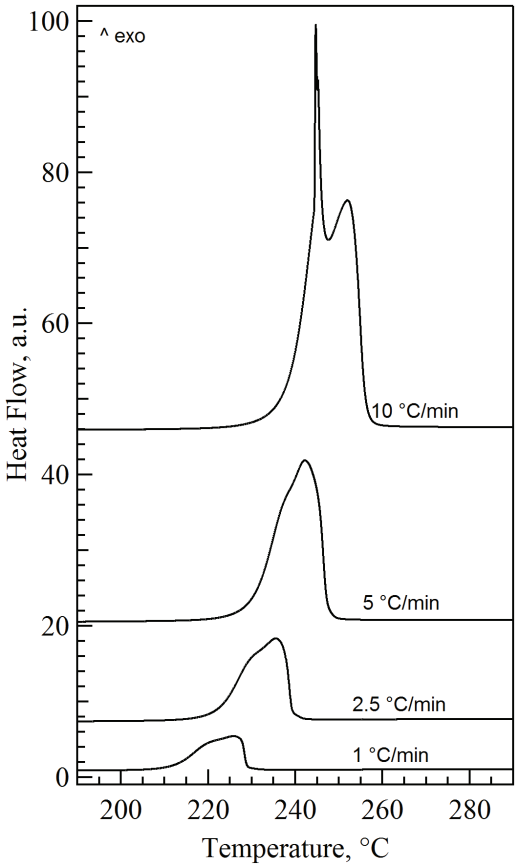

Figure 4.8 – DSC curves obtained for ϵ-CL-20 using Al crucibles.

Heating rate (°C/min)	Mass (mg)	Decomposition peak (°C)	ΔH_{decomp} (J/g)
1	1.28	225.8	3258.4
2.5	1.02	235.5	3078.5
5	0.90	242.1	2997.3
10	0.61	244.7	2660.4

Table 4.4 – Thermodynamic data extracted from the DSC curves on CL-20 in Al crucibles.

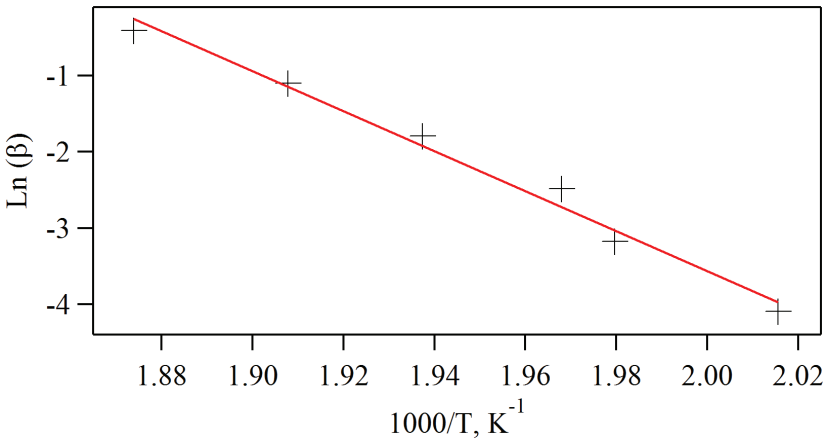

Figure 4.9 – Ozawa plot for heating ramps of CL-20.

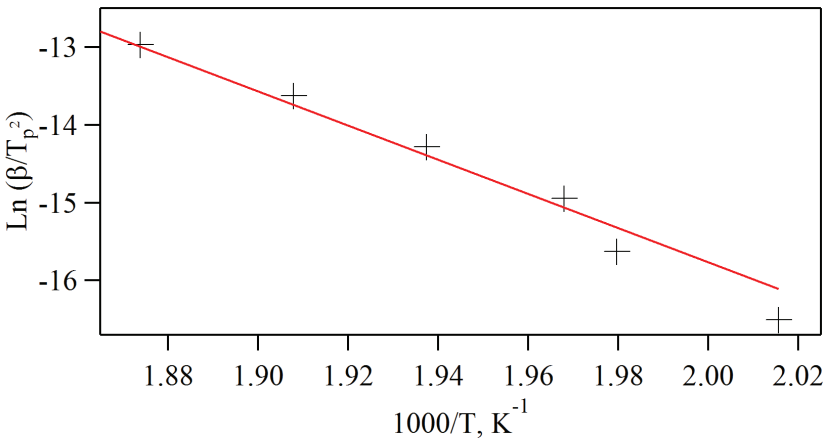

Figure 4.10 – Kissinger plot for heating ramps of CL-20.

In Figures 4.9 and 4.10 are shown both Ozawa and Kissinger plots for the data obtained from the conventional DSC curves. By fitting linearly these data, we obtained for the activation energy values (207.5 and 209.8 kJ mol^{-1}, respectively) which are close to the values given by Geetha and coworkers, 209.8 kJ mol^{-1} [9] and Nedelko and coworkers, 222 kJ mol^{-1} [8].

Thermal behavior of PETN

Conventional DSC curves corresponding to heating ramps of PETN are shown in Figure 4.11; the data extracted from the curves are summarized in Table 4.5.

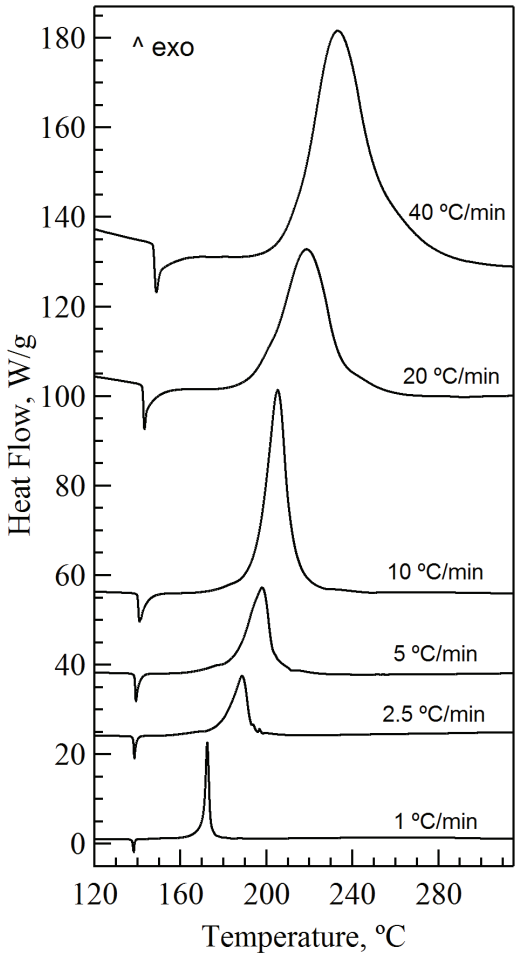

Figure 4.11 – DSC curves corresponding to heating ramps of PETN-I.

The curves show an endothermic transition in-between 138-149 ℃ corresponding to the melting process and an exothermic peak in-between 171-212 ℃ pertinent to the decomposition. The latter is described in the literature as a four-step process [11], which are enumerate below:

1. PETN → Condensed Phase Intermediates

2. PETN + Condensed Phase Intermediates → Gaseous Intermediates

3. Condensed Phase Intermediates → Gaseous Intermediates

4. Gaseous Intermediates → Final Products (CO_2, H_2O, N_2, CO, etc.)

The melting enthalpy values are very close to the values found in the literature, 152 kJ mol^{-1} [7], except for the highest heating rates due to the same reasons explained above for the case of RDX, i.e. the inaccuracy in tracing a good baseline. Unfortunately, the decomposition enthalpy values in comparison with the literature values follow the same trend as with the other materials described before: the use of different types of crucibles precludes quantitative comparison of the values.

Heating rate (℃/min)	Mass (mg)	Melting onset (℃)	Melting enthalpy change (J/g)	Decomposition onset (℃)	ΔH_{decomp} (J/g)
1	1.54	137.6	136.4	170.8	3980.1
2.5	0.84	138.1	142.9	179.5	3523.8
5	0.84	139.3	143.0	185.2	3380.9
10	1.57	140.9	127.4	195.0	3630.6
20	0.56	143.3	107.1	197.9	2625.2
40	0.72	148.8	69.4	211.9	2500.6

Table 4.5 – Thermodynamic data on PETN-I extracted from DSC curves.

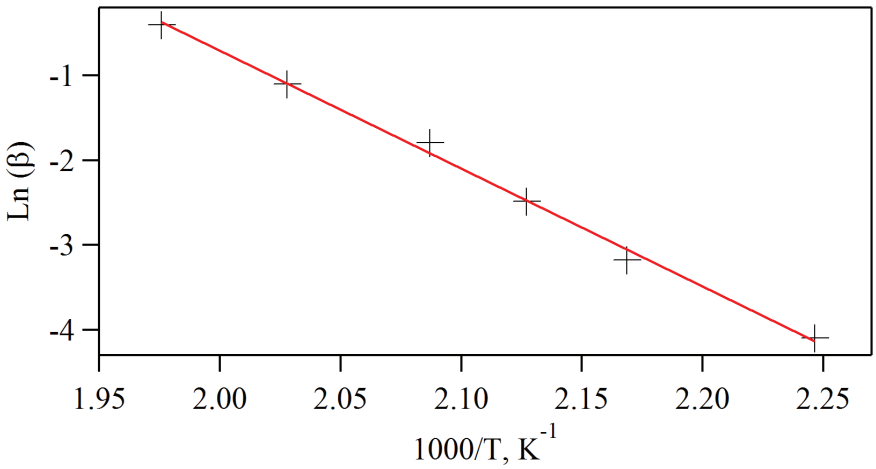

Figure 4.12 – Ozawa plot for PETN-I.

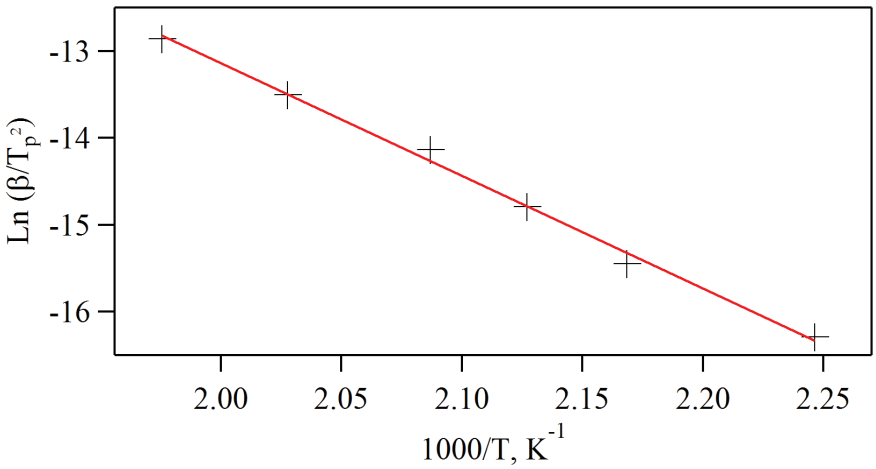

Figure 4.13 – Kissinger plot for PETN-I.

The activation energy has been calculated by fitting linearly the data using both Ozawa (cf. Figure 4.12) and Kissinger (cf. Figure 4.13) plots. The values obtained, 109.8 and 107.7 kJ mol^{-1} are a bit smaller to those reported in literature [4], although apparently different authors reported values with significant discrepancies (from 117 up to 337 kJ mol^{-1}).

Thermal behavior of TNT

Conventional DSC curves are shown in Figure 4.14 and the data extracted from them are summarized in Table 4.6.

The curves exhibit a two-stage process, as documented in the literature. The first endothermic transition in-between 78-89 °C corresponds to the melting process, while a two-stages exothermic decomposition occurs in-between 278-355 °C. The first stage of the decomposition process is a very sharp peak, but there is also a weak second stage which can involve about 20 % of mass loss, as it is reported by Makashir and Kurian [12].

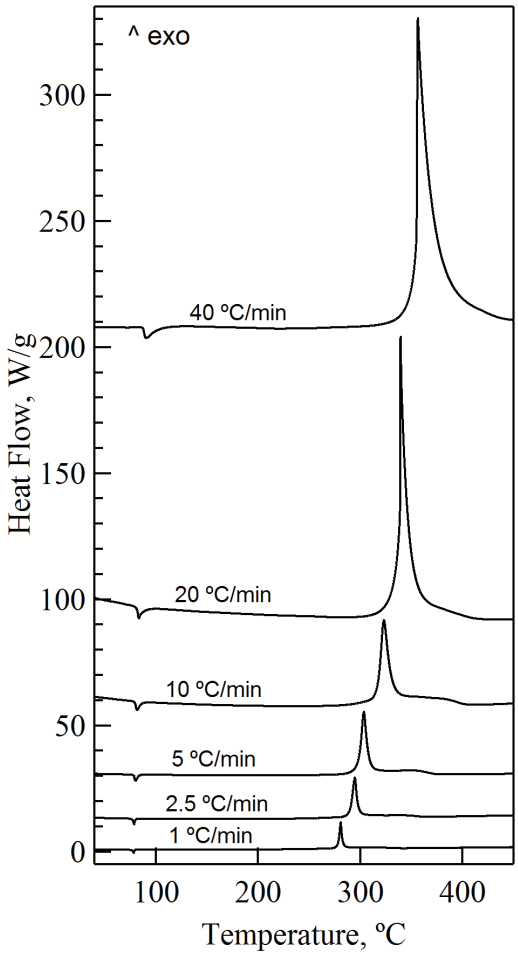

Figure 4.14 – DSC curves obtained for TNT.

Heating rate (°C/min)	Mass (mg)	Melting onset (°C)	Melting enthalpy change (J/g)	Decomposition onset (°C)	ΔH_{decomp} (J/g)
1	2.12	78.0	108.5	278.0	3584.9
2.5	1.48	78.4	101.4	289.9	3486.5
5	2.86	79.0	87.4	298.5	3489.5
10	1.04	80.7	76.9	316.8	3663.5
20	1.05	85.6	66.7	338.7	3819.1
40	0.99	89.2	50.5	355.0	2949.5

Table 4.6 – Thermodynamic data from DSC curves on TNT.

The melting enthalpy values are in a relatively good agreement (108–77 versus 96 KJ mol^{-1}) with those reported in literature [7] except for the highest heating rates. Our guess is that the discrepancies can be accounted for by the same reasons as for PETN. The decomposition enthalpy values are again exhibiting discrepancy with the values reported in the literature, but this time the discrepancies are not as big as for the the rest of the materials studied, ∼3500 versus ∼2500 kJ mol^{-1} [6]. The reason is that in this particular case, the authors use high-pressure crucibles, which makes our comparison quantitative.

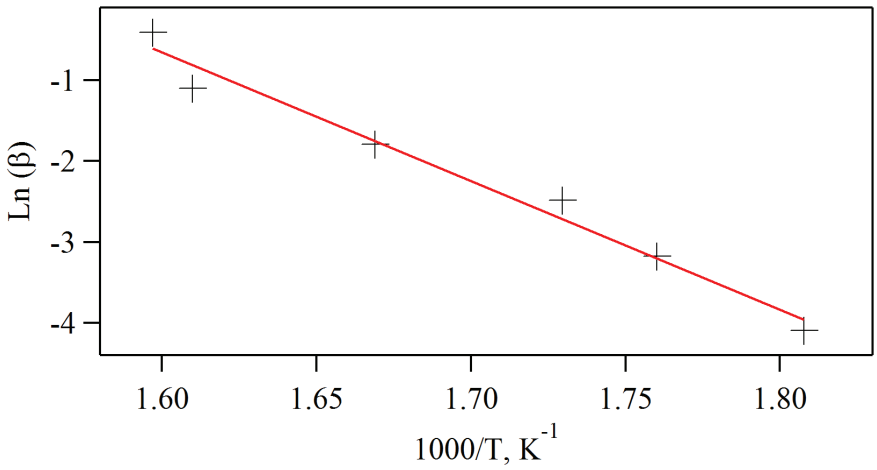

Figure 4.15 – Ozawa plot for TNT.

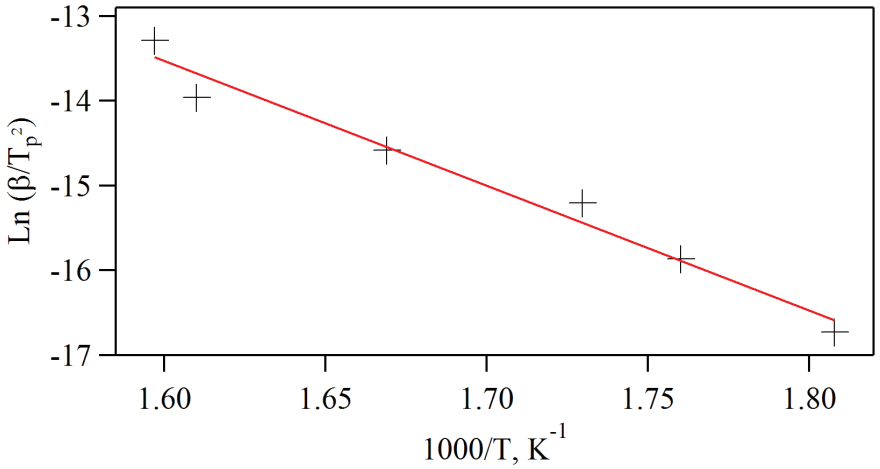

Figure 4.16 – Kissinger plot for TNT.

The activation energy has been calculated using a linear fit by both Ozawa (cf. Figure 4.15) and Kissinger (cf. Figure 4.16) methods. The values obtained are within the limits of the values reported in the literature by Long and coworkers (∼136 kJ mol^{-1}) for sealed high-pressure crucibles [6].

Below are summarized the data for the activation energy of the energetic materials studied in this work.

Material	Ozawa (kJ/mol)	Kissinger (kJ/mol)
HMX	229.16	231.96
RDX	144.56	143.56
CL-20	207.53	209.76
PETN	109.84	107.66
TNT	125.65	122.38

Table 4.7 – Activation energies for the different explosives studied in this work.

4.2 Nanocalorimetry analysis of standard explosives

Once the experiments with the conventional DSC completed, we continue this study with nanocalorimetry. The reason to use nanocalorimetry is mainly to extend the range of heating rates and to bring the explosives to the conditions closer to the decomposition. As in the case of conventional DSC, different heating rates will be employed. It is noteworthy that these rates are several orders of magnitude higher than the ones used by DSC.

The experiments at extremely fast heating rates may allow us to discriminate the energetic materials, based on their thermal behavior (e.g., melting, evaporation, decomposition, etc.) thereby generating a thermal signature of a given explosive on the basis of a single micron-sized particle.

The mass of the particles studied by nanocalorimetry has been measured by dividing the enthalpy change values obtained after integration of the melting peaks by the specific heat of fusion reported in the literature [5, 7].

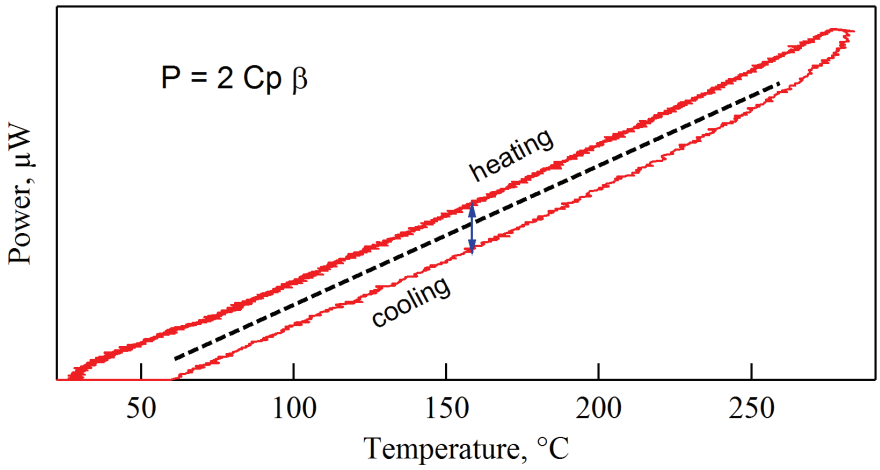

Figure 4.17 – Alternative way for calculating the mass of a particle from the heat capacity at constant pressure.

The approach used when the particle does not undergo melting (e.g., CL-20) is the following. The mass was measured from the corresponding heat capacity values by doing a short heating/cooling cycle from R.T. to 70 °C.

From the corresponding nanocalorimetric curves, the C_p was extracted and, consequently the mass was computed, as shown in Figure 4.17.

Although this is a perfectly valid method to calculate the mass of a single particle [13], it is not sufficiently accurate in the case of other energetic materials because they sublimate during heating, as will be shown later.

HMX

The nanocalorimetry experiments were performed on micron-sized particles of β-HMX. In the curves, we observe an endothermic process corresponding to melting (cf. Figure 4.19). During conventional DSC experiments, the melting process is masked by the proximity of the decomposition. But since the decomposition is not observed in the nanocalorimetric experiments, the melting process becomes perfectly visible. The melting onset temperatures are somewhat lower than the ones that are supposedly measured by DSC [4]. However, there is no clear melting event shown by the authors, which may put some doubt on the precision of the melting point determination by the conventional DSC. In our case, some scattering in the melting onset temperatures can be attributed to the movement of the particle with respect to its original position on the membrane and to the temperature gradient built up on the sensor surface, as discussed in the previous chapter.

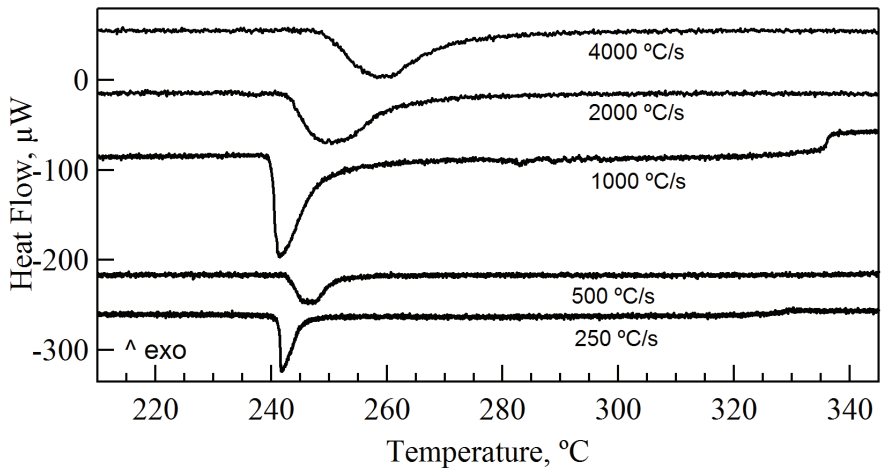

Figure 4.18 – Fast heating experiments performed on HMX particles.

Table 4.8 summarizes the data extracted from the nanocalorimetric curves. In contrast to the melting onsets, the melting enthalpy values agree well with the values reported in the literature [5].

Heating rate (°C/s)	Mass (ng)	Melting onset (°C)	Melting enthalpy (J)
250	7.9	240.4	5.99E-7
500	4.3	248.2	3.23E-7
1000	8.3	234.2	6.33E-7
2000	4.5	250.7	3.42E-7
4000	2.5	245.1	1.92E-7

Table 4.8 – Thermodynamic data extracted from the nanocalorimetric curves of HMX.

RDX

The nanocalorimetric experiments were also performed on micron-sized particles of α-RDX. There are some differences between the conventional DSC and Nanocalorimetry, especially concerning the experimental conditions of both techniques. Conventional DSC experiments are performed in sealed crucibles, whereby the vapors generated during heating can not escape. On the contrary, nanocalorimetric experiments use sensors placed at ambient pressure. The minuscule amount of vapors generated by a micron-sized particle is immediately taken away by the air which surrounds the sensor bringing the conditions far from the saturation vapour pressure.

Also, the amount of material analyzed by Nanocalorimetry is 6-7 orders of magnitude smaller. As a consequence of this, the heating rates applied by Nanocalorimetry can be up to 4-5 orders of magnitude faster than with a conventional DSC.

In Figure 4.19 the melting process is visible as an endothermic sharp peak which becomes broader when the heating rate increases. As in the case of HMX, the decomposition process is not visible. Instead, one can

observe evaporation, as it was confirmed by fast CCD camera videos recorded during the experiments. The reason for these changes is related with the activation energies needed to evaporate or to decompose the material. A branching ratio of decomposition to vaporization of 1 to 4 is estimated in open environment, so even for an exothermic process like decomposition, RDX occurs via vaporization [14].

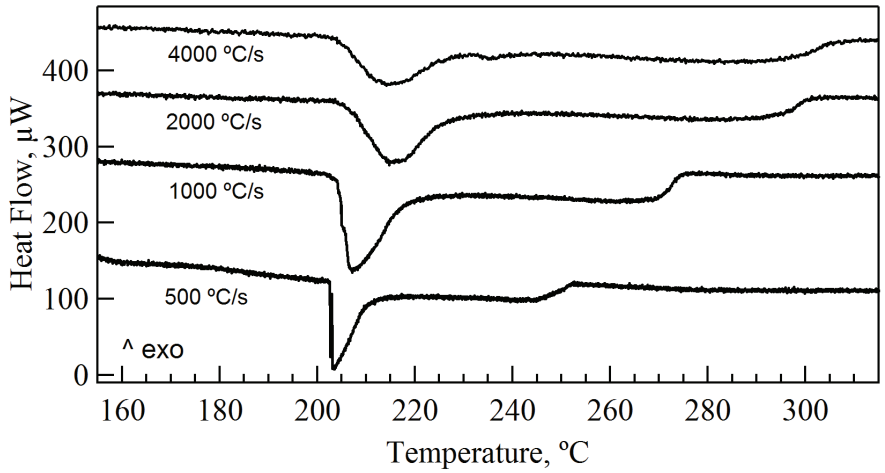

Figure 4.19 – Fast heating experiments performed on RDX particles.

Heating rate (°C/s)	Mass (ng)	Melting onset (°C)	Melting enthalpy (J)
500	12.9	197.5	1.04E-6
1000	13.2	199.1	1.07E-6
2000	6.0	206.0	4.84E-7
4000	3.1	205.4	2.42E-7

Table 4.9 – Thermodynamic data extracted from the nanocalorimetric curves of RDX.

Table 4.9, summarizes the data obtained from the nanocalorimetric curves. As in all the described cases, the melting enthalpy changes were calculated using a custom-made procedure in Igor Pro, which takes into account the

applied heating rate and the different slopes of the baseline before and after the melting process.

CL-20

It is known that the cage structure of CL-20 slows down the diffusion of the decomposition products to the surroundings. These can be recombined via radicals with the backbone of the CL-20 molecule leading to a dark and non-soluble carbonaceous residue (cf. Figure 4.20) on the sensor surface after the fast heating experiments, unlike other explosives with two dimensional cyclic, or branched, structures [15].

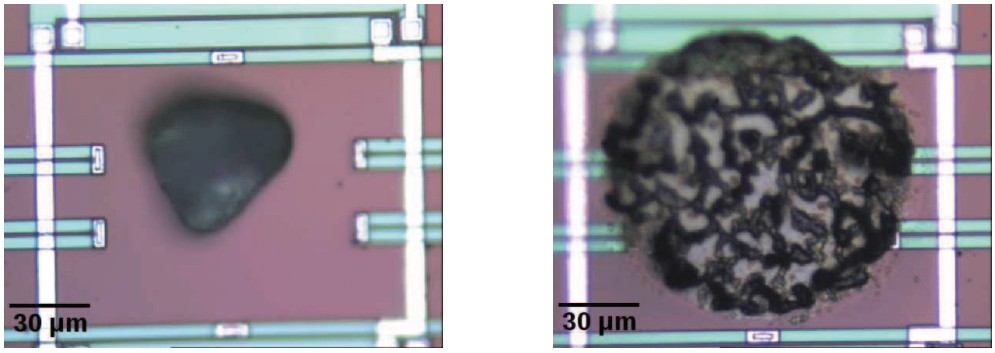

(a) CL-20 particle before heating. (b) CL-20 particle after heating.

Figure 4.20 – CL-20 particle before and after a fast heating experiment.

The nanocalorimetric curves given in Figure 4.21 show a weak broad endothermic peak corresponding to the solid-solid transition from ϵ-phase to γ-phase at ~195–205 °C. Compared with conventional DSC and with the literature data, the decomposition peak is shifted upwards in temperature [8] due to the high heating rates applied.

Interestingly, the curves at higher heating rates reveal the signs of a melting process just before the decomposition. This partial melting can also be observed in the fast camera videos recorded during the experiments. In this case, the nature of the process can be confirmed by the loss of birefringence of the particle when it is heated up in steps and subsequently quenched to R.T. (cf. Figures 4.23 and 4.24). The heating profiles are shown in Figure 4.22.

This result contradicts the view of some of the authors stating that thermal decomposition of CL-20 is a purely solid-state process [8].

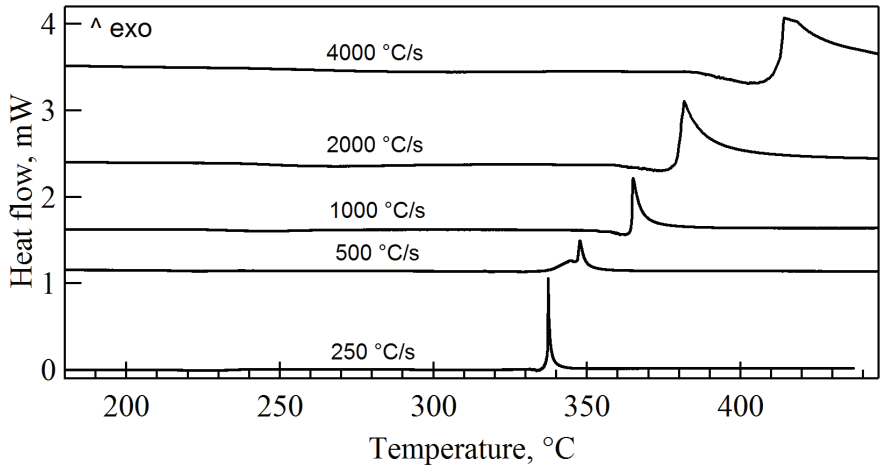

Figure 4.21 – Fast heating experiments performed on CL-20 particles.

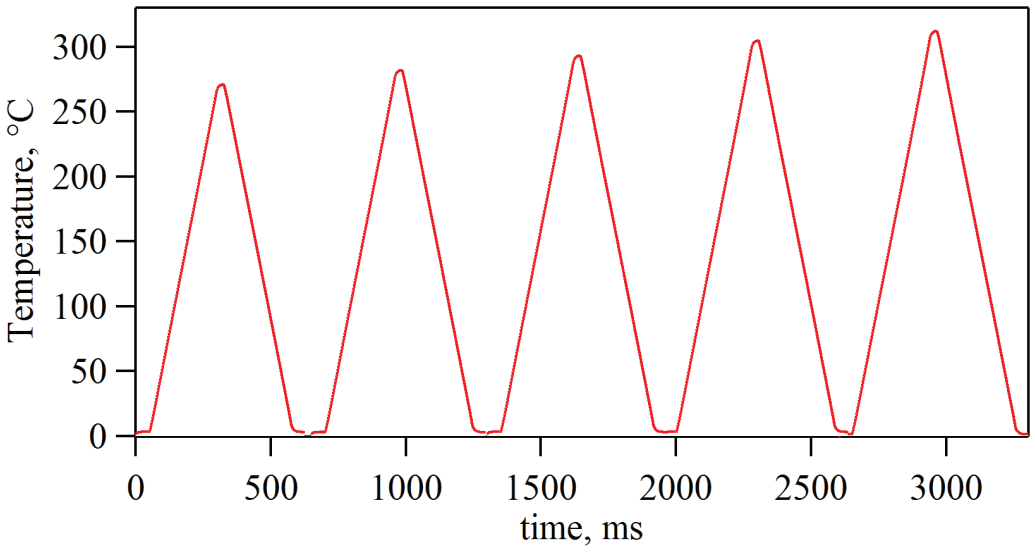

Figure 4.22 – Heat profiles applied to the same CL-20 particle.

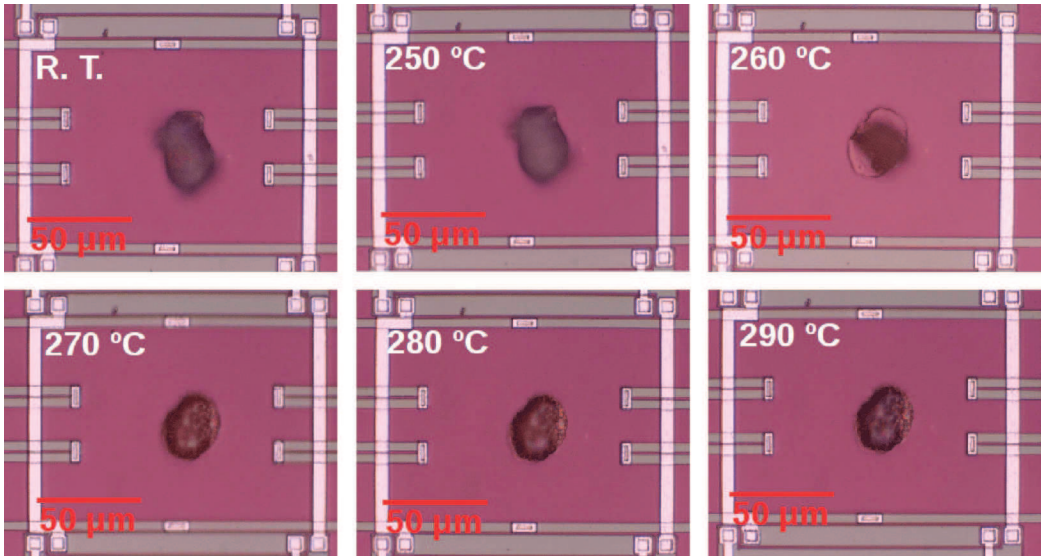

Figure 4.23 – Micrographs recorded during a stage-wise heating of a CL-20 particle.

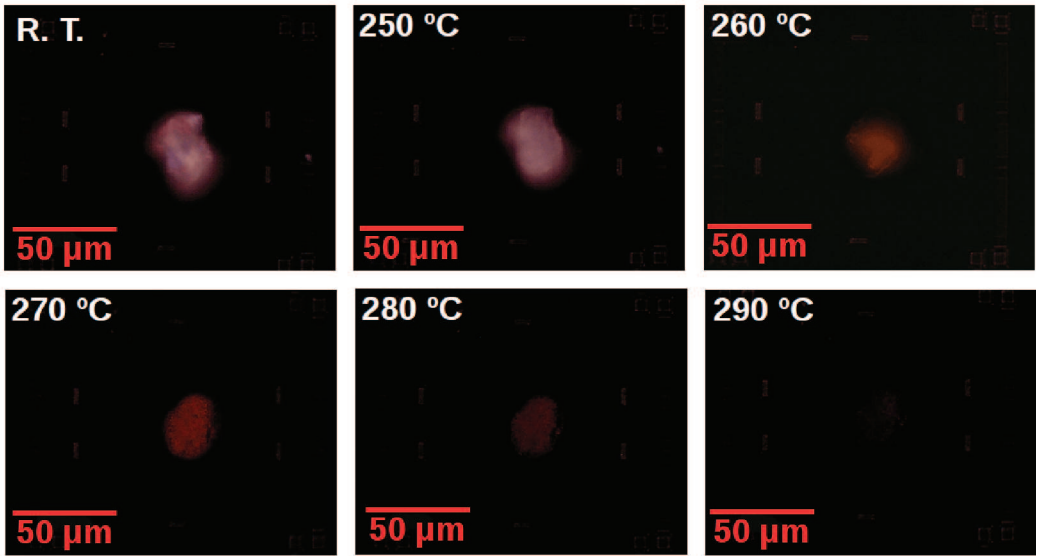

Figure 4.24 – Loss of birefringence upon a stage-wise heating of a CL-20 particle.

The data extracted from the nanocalorimetric curves are summarized in Table 4.10.

Heating rate (°C/s)	Mass (ng)	Decomposition peak (°C)	Decomposition enthalpy (J)
250	23.4	337.4	4.64E-6
500	18.9	347.7	2.87E-6
1000	22.1	365.0	3.91E-6
2000	24.5	381.7	7.15E-6
4000	23.1	414.2	–

Table 4.10 – Thermodynamic data extracted from nanocalorimetric curves of CL-20.

As the decomposition of CL-20 is detected in the nanocalorimetric curves, it becomes possible to analyze the data using either Kissinger or Ozawa approaches. Figure 4.25 presents this nanocalorimetric data together with the data obtained using conventional DSC. Note that the activation energy is in good agreement with the value obtained with conventional DSC data (E_a = 188.89 kJ/mol).

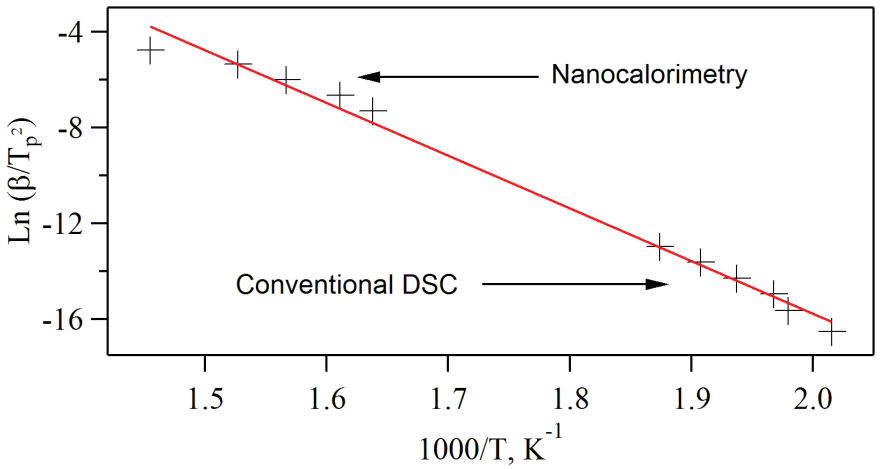

Figure 4.25 – Kissinger plot for CL-20 combining Nanocalorimetry and conventional DSC.

PETN

Figure 4.26 shows the experiments made with PETN micron-sized particles. As with the other explosives, decomposition is not registered in the nanocalorimetric curves. The videos recorded with the fast camera clearly show the melting process followed by a continuous shrinking in size of the formed drop until its disappearance by evaporation. The evaporation process is finished when the step in the curves reaches the baseline. As all the kinetic processes, evaporation is shifted upwards in temperature as soon as the heating rates increases.

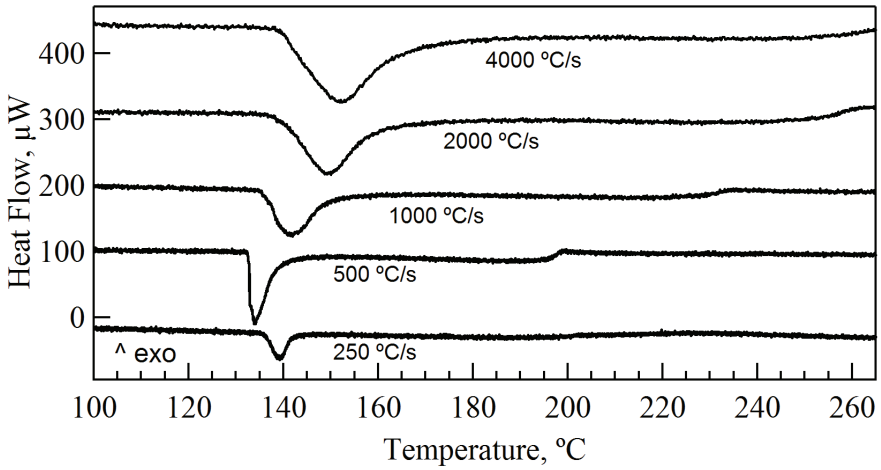

Figure 4.26 – Fast heating experiments performed on PETN particles.

Once again, since the particles are unconfined in the nanocalorimetric experiments, the intermediate product, gases all of them as described before, escape as they are formed, so the final products can not be formed producing the exothermic gas phase reaction, which will lead to the decomposition as it is stated by Tarver et al. [11]. In conventional DSC experiments, the use of high-pressure sealed crucibles where the samples are close off make the experimental conditions quite different from the experiments performed with the nanocalorimeter, where the particles are just placed on a sensor and they are heated up at ambient conditions. The interesting point is that even if the decomposition process can not be reached, the melting behavior is quite similar in both conventional DSC and Nanocalorimetry.

In Table 4.11, data from the nanocalorimetric curves are summarized. Values obtained for the melting enthalpy are in agreement with the data reported in literature [4, 7].

Heating rate (°C/s)	Mass (ng)	Melting onset (°C)	Melting enthalpy (J)
250	3.76	137.0	5.71E-7
500	6.01	132.7	9.14E-7
1000	4.34	137.3	6.59E-7
2000	4.25	141.2	6.46E-7
4000	4.07	142.4	6.19E-7

Table 4.11 – Thermodynamic data from nanocalorimetric curves on PETN.

TNT

Figure 4.27 show experiments made on TNT micron-sized particles at different heating rates. Decomposition process is neither detected in this case. Videos recorded with the fast camera show clearly the melting process followed by a continuous shrinking in size of the formed drop until its disappearance by evaporation. This latter process is finished when the step in the curves ends.

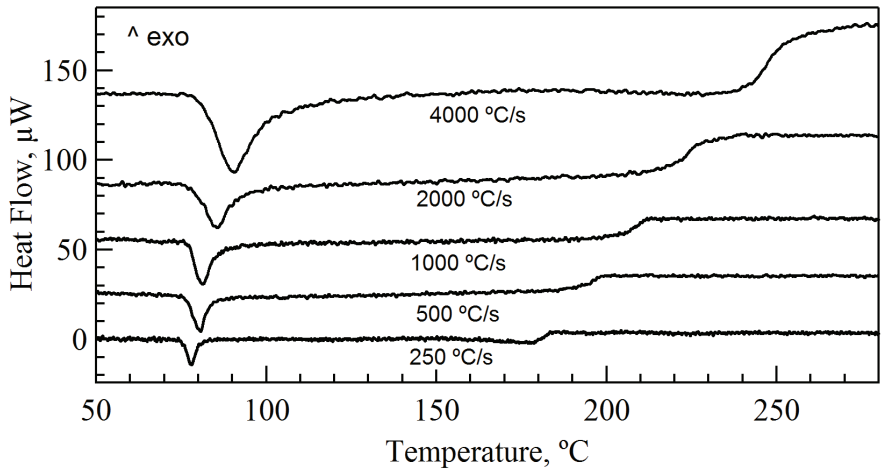

Figure 4.27 – Fast heating experiments performed on TNT particles.

In Table 4.12, data from the nanocalorimetric curves are summarized. Values obtained for the melting enthalpy are similar to those reported in literature [6, 7].

Heating rate (°C/s)	Mass (ng)	Melting onset (°C)	Melting enthalpy (J)
500	1.71	78.1	1.65E-7
1000	1.14	79.9	1.10E-7
2000	1.09	80.4	1.05E-7
4000	1.62	81.5	1.57E-7

Table 4.12 – Thermodynamic data from nanocalorimetric curves on TNT.

4.3 AC Nanocalorimetry Experiments

Temperature-modulated heating ramps were performed on micron-sized particles of explosives. The results are shown in Figure 4.28. During the AC measurements, a small current (current amplitude 0.1 mA, current offset 0.3 mA) oscillating at a frequency of 37.5 Hz was applied to the heating elements while performing the experiments at a constant heating rate of 20 °C min^{-1} [16]. This operation mode is similar to the conventional temperature-modulated DSC technique [17]. During the experiment, the sample is subjected to heating power oscillations while its temperature response is measured. In the curves one can see a general increase of the temperature modulation amplitude, whch results from a corresponding increase of the electrical resistance with temperature. Technically, the modulation is realized with a current source, so the modulation power is proportional to the resistance of the modulator heaters. The curves have not been corrected for this effect. However, clearly, on top of the slowly increasing amplitude, one can see a step-wise variation, which corresponds to a decrease in the sample heat capacity (C_p).

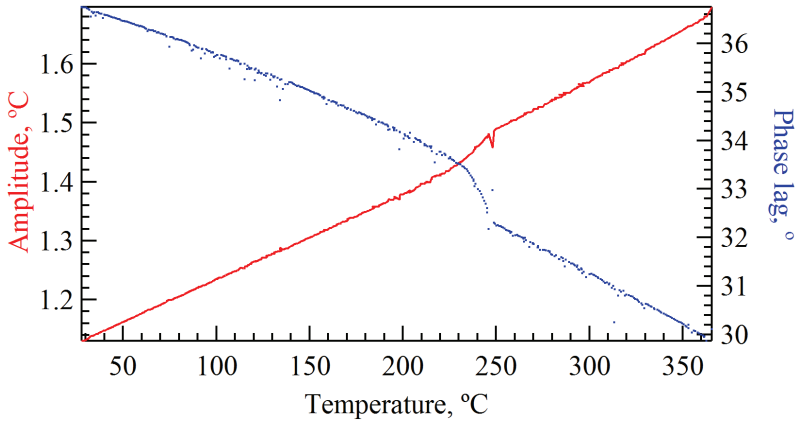

(a) HMX

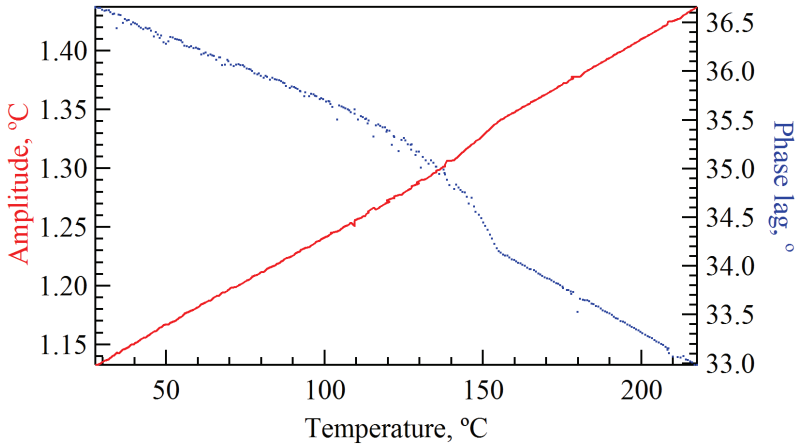

(b) RDX

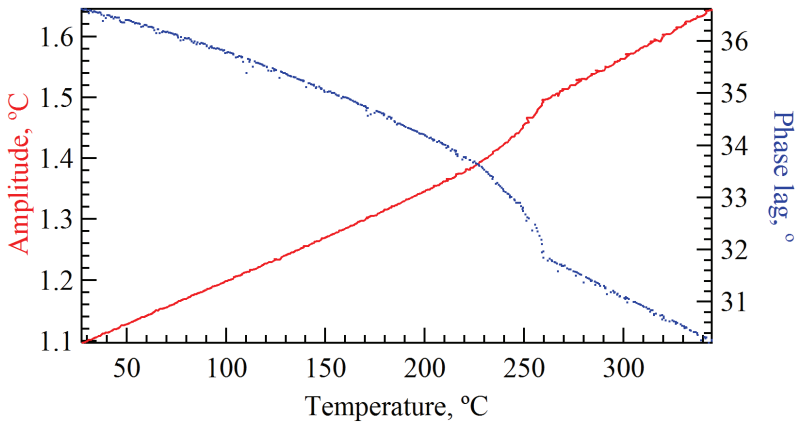

(c) CL-20

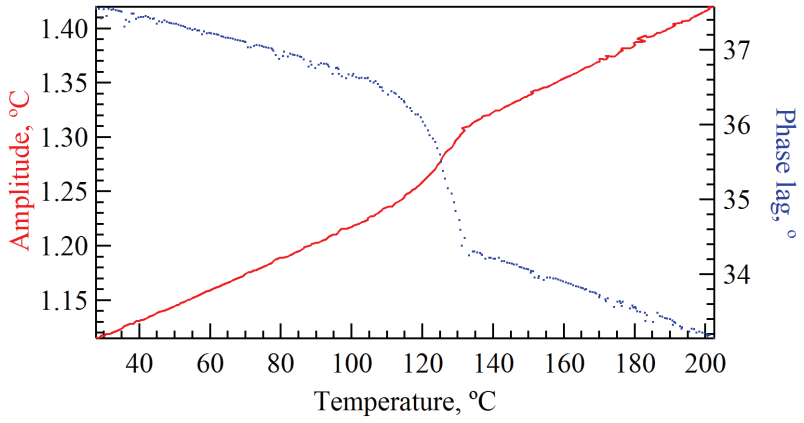

(d) PETN

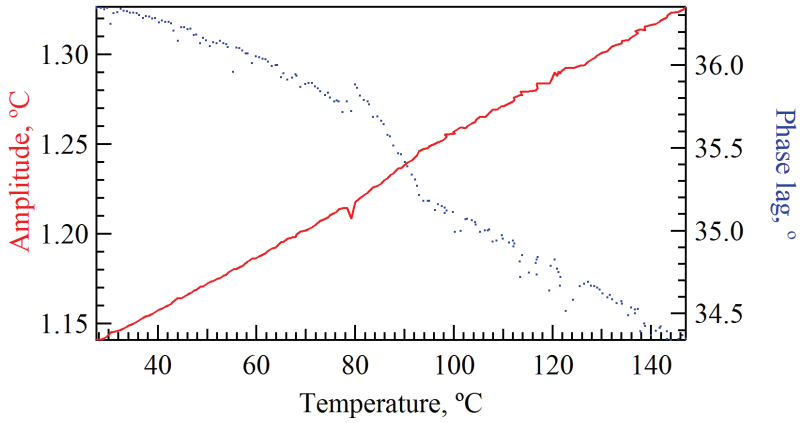

(e) TNT

Figure 4.28 – Temperature-modulated heating curves for explosives' microparticles. The general increasing trend of the curves explains by the fact that the modulation has been performed with a current source, and the resistance values increase with temperature.

Following the heating process under an optical microscope, it can be seen that the materials sublimate easily during heating ramps. The sublimation process is clearly visible on the graphs. It corresponds to a fast decay of the phase signal and to an increase of the amplitude signal due to a decrease of the particle mass.

Only in the case of TNT, having a low melting point, a sharp event is seen on the curve. This event, according to its onset temperature, corresponds to

the melting process. In Table 4.13 values of the vapor pressure of the pure explosives used in this work are summarized. It can be seen that the vapor pressure is the highest for TNT and the lowest for CL-20. The latter can be the reason why the decomposition of CL-20 was observed in fast heatings in contrast to the other explosive materials studied in this work.

Explosive	Vapor pressure (Pa)
HMX	10^{-10}
RDX	10^{-6}
CL-20	10^{-14}
PETN	10^{-5}
TNT	10^{-4}

Table 4.13 – Vapor pressure at 25 °C for different explosives [18, 19].

In all cases but TNT, sublimation products crystallize in the cold areas of the sensor as it is shown in Figure 4.29 for different particles.

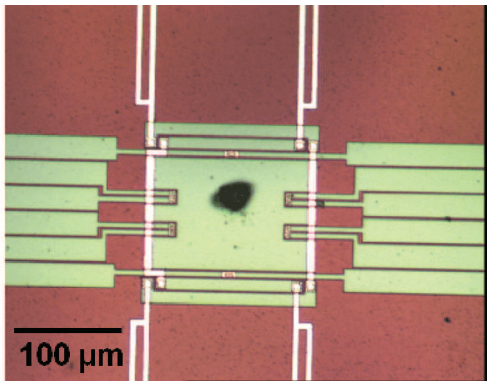

(a) HMX particle before.

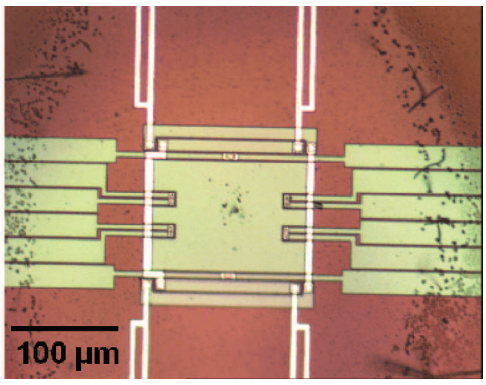

(b) HMX crystals after.

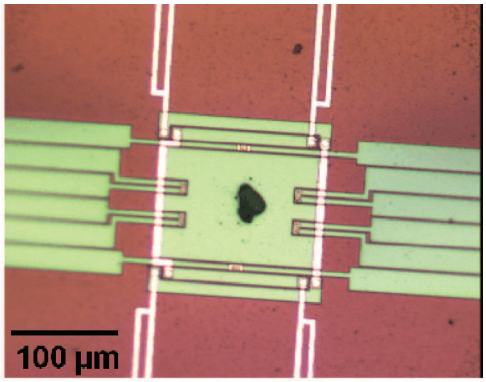

(c) RDX particle before.

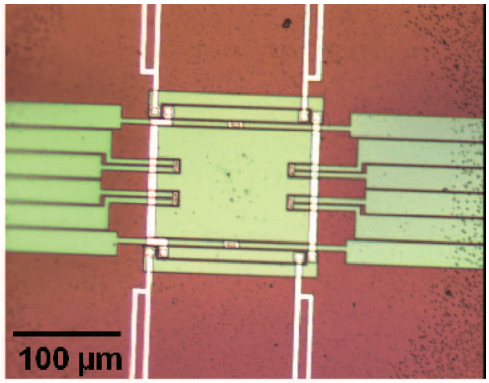

(d) RDX crystals after.

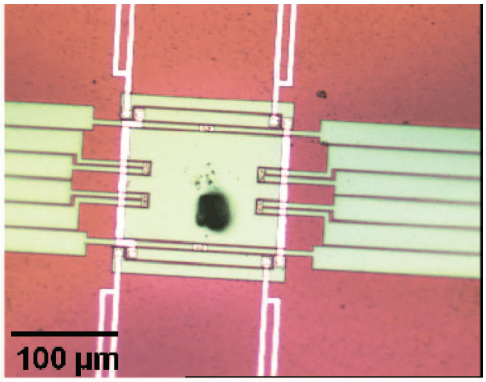

(e) CL-20 particle before.

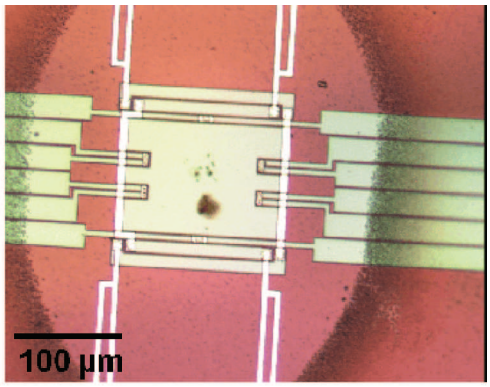

(f) CL-20 crystals after.

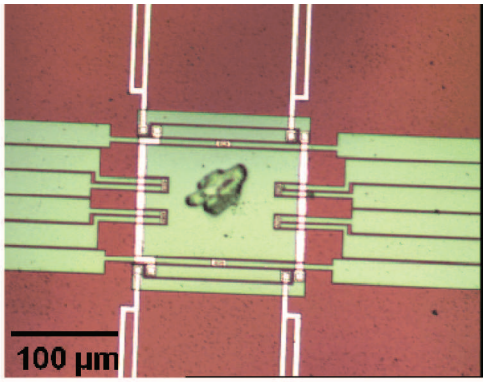

(g) PETN particle before.

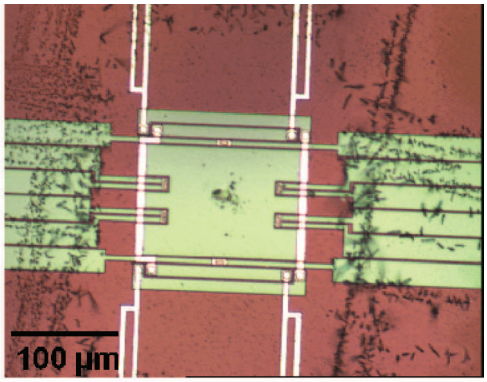

(h) PETN crystals after.

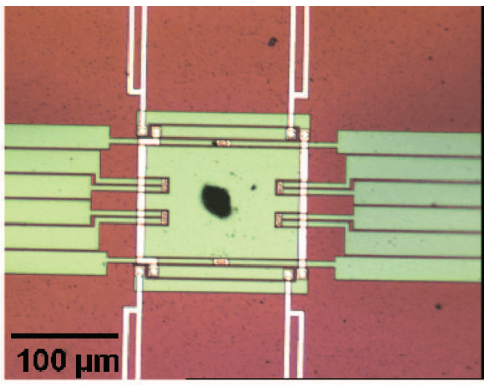

(i) TNT particle before.

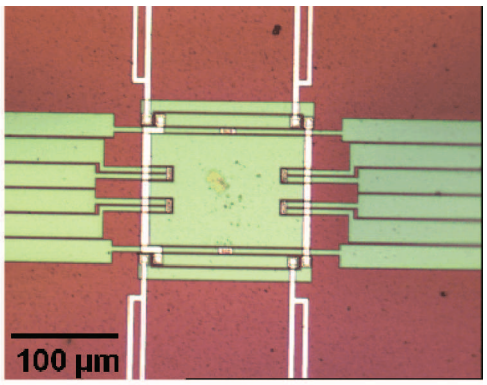

(j) TNT particle after.

Figure 4.29 – Micrographs of the particles of explosives used in modulation experiments.

To confirm that the recrystallized material have the same nature as the initial explosives, Raman spectroscopy was performed on the micro-particles before the experiments and on the crystals formed on the cold areas of the sensor after the experiments. The results are exemplified for the case of PETN on Figure 4.30. It can be seen that the peaks are indeed identical for both cases.

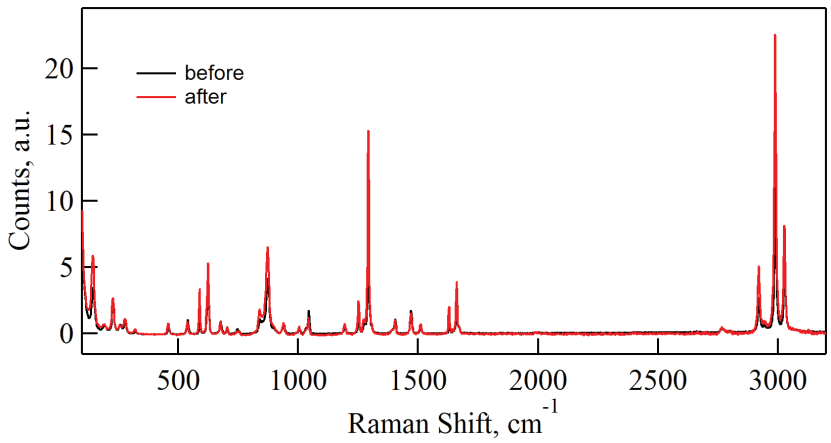

Figure 4.30 – Raman spectra of PETN before and after AC experiments.

4.4 Melting and recrystallizations experiments

One of the advantages of Nanocalorimetry is that extremely high heating/cooling rates that can be employed, can allow separation between different thermal transitions such as for example melting, evaporation and decomposition. Given that the sublimation/evaporation processes for such small objects are very fast, high heating/cooling rates make it possible to study how a single particle can be repeatedly recrystallized from the molten state. Additional information on the structure can be obtained by combining nanocalorimetry and X-ray diffraction.

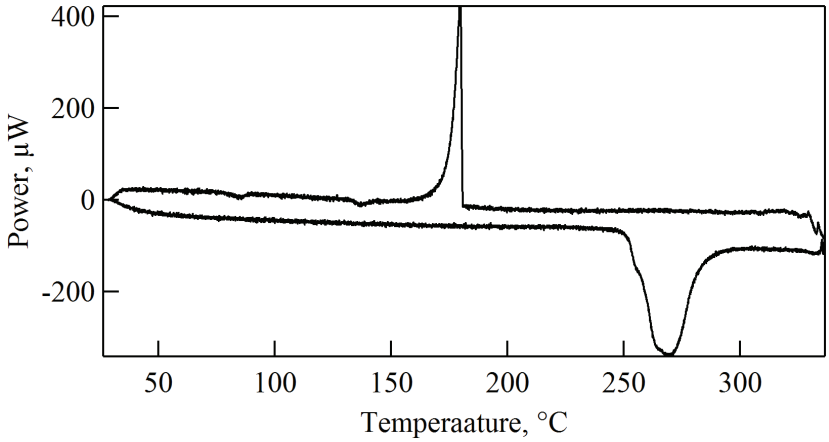

Figure 4.31 – Melting and recrystallization of an HMX micro-particle.

In Figure 4.31 a nanocalorimetric curve with both melting and recrystallization processes is shown. The heating and cooling ramps applied were 1000 °C s^{-1}.

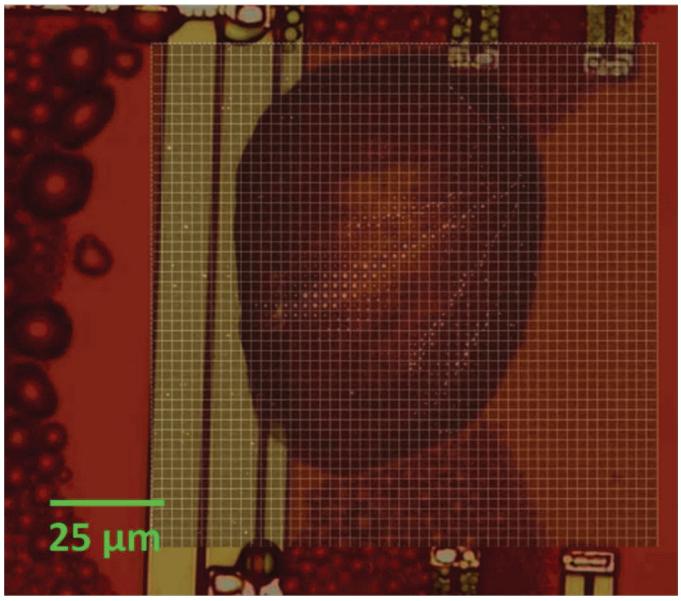

Figure 4.32 – HMX particle recrystallized from the melt. Mapping of the X-ray intensity allows visualizing the radially oriented domains from which a spherulitic texture can be inferred.

Figure 5.3 presents a composite image of an HMX particle on a XEN-39392 sensor (before being heated) with an image of the same particle obtained by mapping the diffracted intensity of a single 120 crystalline reflection of β-HMX. The mesh scan was performed with a lateral resolution of 2 µm using nano-focus X-ray scattering at the ESRF. As it can be seen, before the nanocalorimetric experiment the particle unambiguously shows a typical texture of a single crystal.

After quenching, the recrystallization process was explored by mapping the intensity of the same reflection as the one in Chapter 5. Figure 4.32 clearly shows the presence of radially oriented domains having the same crystal orientation. This is reminiscent of the spherulitic morphology. Therefore, the particle texture after the experiment is not single-crystalline anymore. The presence of small drop-like particles of HMX at the borders of the active area proves that during the heating process, the particle partially evaporates and recrystallizes in the coldest area of the sensor, as it is shown in Figure 4.32.

As far as RDX is concerned, it was found that it behaves similarly to HMX, meaning that a recrystallization process appears after quenching at

high cooling rates. The same heating/cooling conditions as for the case of HMX were applied to RDX (cf. Figure 4.33). The resulting nanocalorimetric curve reveals both melting and recrystallization peaks.

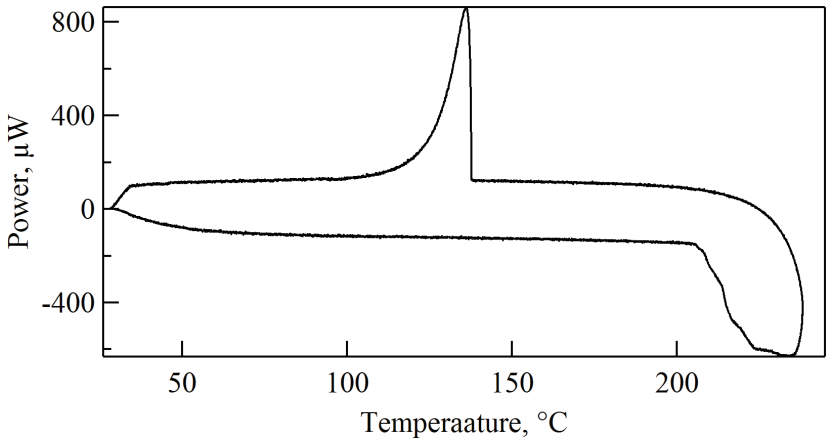

Figure 4.33 – Melting and recrystallization of an RDX particle at 1000 °C s^{-1}.

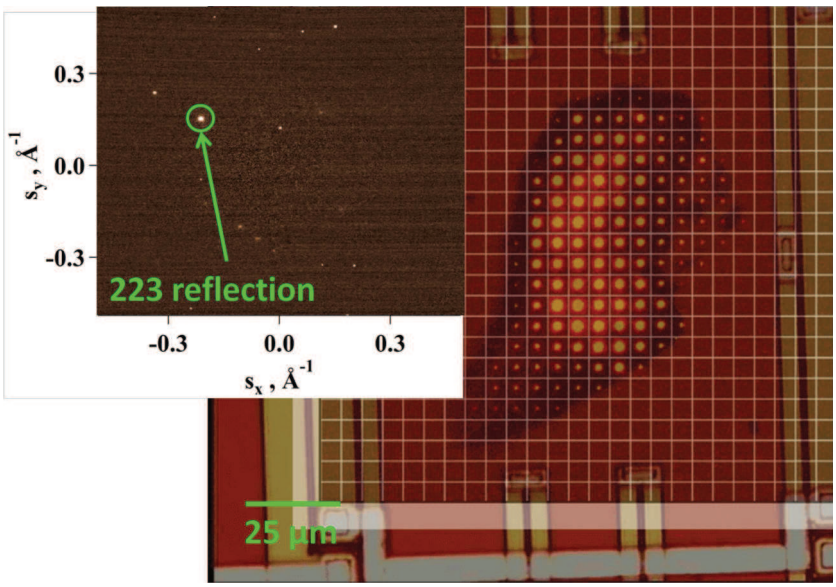

Figure 4.34 – α-RDX particle before heating showing a single-crystal structure.

Figure 4.34 shows a composite image of an RDX particle superposed with the image of the same particle obtained by mapping the scattered intensity

of a single 223 crystalline reflection of α-RDX. The mesh scan was performed with a lateral resolution of 2 µm using nano-focus X-ray scattering at ESRF. As it is shown, before starting the experiment the particle was a single crystal because the spatial distribution of the scattering intensity nicely reproduces the particle shape, as observed optically.

As it can be seen in Figures 4.35 and 4.36, by changing the cooling rates, 2500 °C s^{-1} for Figure 4.35 and 25000 °C s^{-1} for Figure 4.36, the poly-crystalline character of the material enhances.

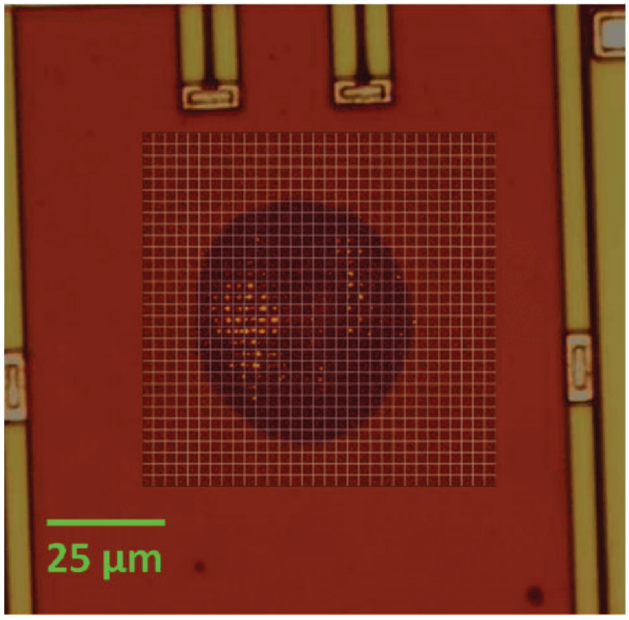

Figure 4.35 – RDX particle after heating/cooling at 2500 °C s^{-1} showing a polycrystalline texture.

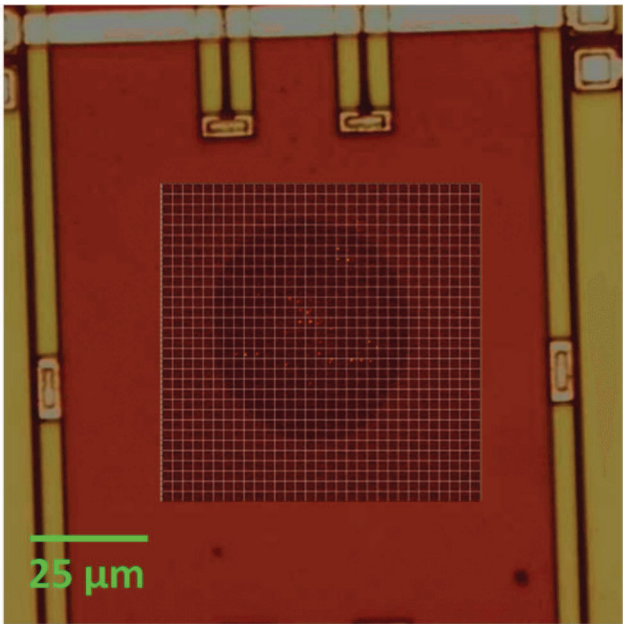

Figure 4.36 – RDX particle after heating at 25000 °C s^{-1} showing an enhanced polycrystalline structure.

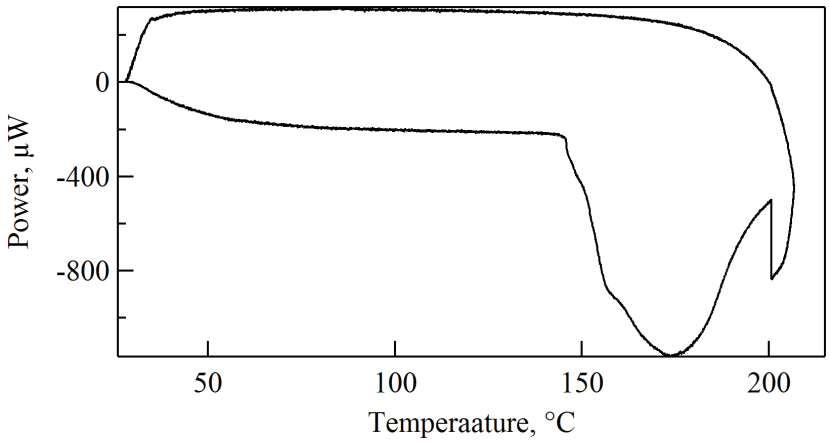

Figure 4.37 – Heating/cooling cycle of a PETN particle performed at a rate of 1000 °C s^{-1}.

On the other hand, PETN does not crystallizes on cooling. As it is shown in Figure 4.37, after performing the same heating/cooling profile described above for HMX and RDX, the PETN particle melts during the heating but there is no evidence of recrystallization during the cooling segment.

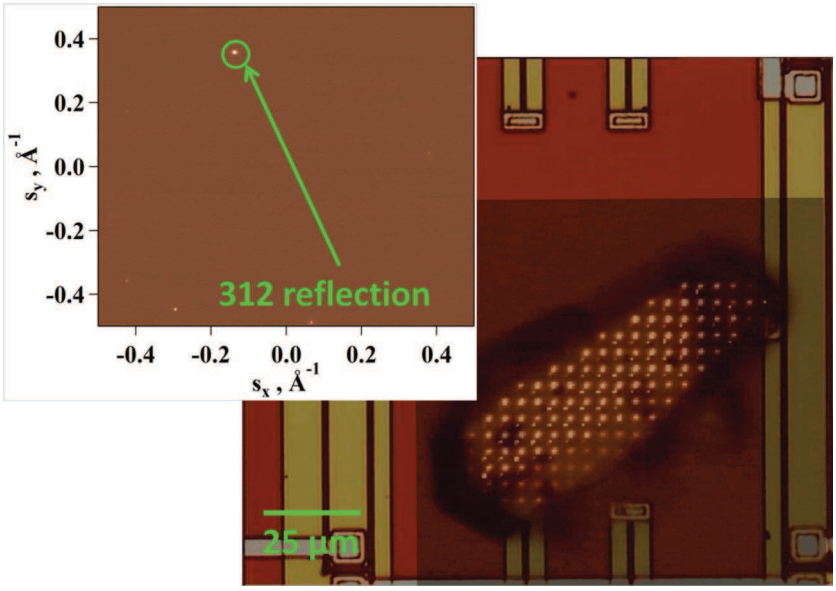

Figure 4.38 – PETN-I particle before heating showing a single-crystal structure.

Nano-focus X-ray scattering performed in a PETN particle (cf. Figure 4.38) shows the initial state of the sample. As it can be seen by mapping the scattered intensity of a single 312 crystalline reflection, the mesh scan shows a single-crystalline nature of the particle before the nanocalorimetric experiment.

After quenching, the drop-like particle remains amorphous, as it is shown in Figure 4.39 by mapping the same single reflection as before. This is the confirmation of the results obtained in the nanocalorimetric experiments, where no recrystallization occurs. In fact, the drop-like particle could stay in such amorphous state for a very long period (e.g., several days) if there is no external perturbation (cf. Figure 4.40). However, even a small perturbation can induce a change in the phase structure. Thus, by touching such a micro-drop with an eyelash, one can induce an immediate crystallization, as it is shown on Figure 4.41.

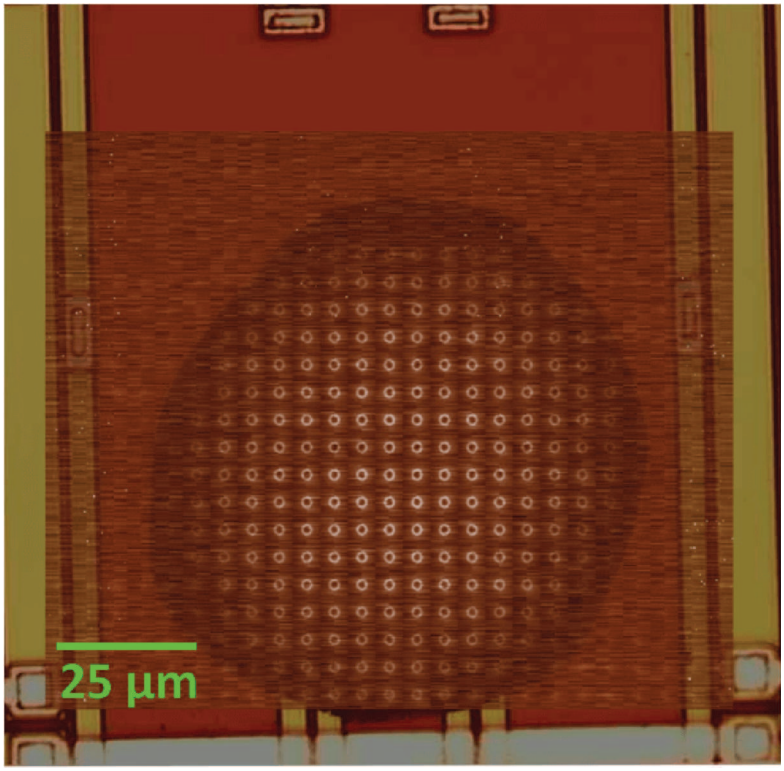

Figure 4.39 – PETN after heating/cooling cycle as an amorphous drop.

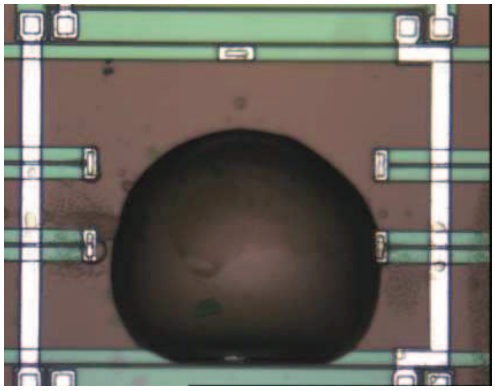

(a) A micro-drop of PETN on a nanocalorimetric sensor.

(b) The same sample under polarized light.

Figure 4.40 – PETN drop-like particle showing no evidence of crystallinity after 3 days exposure at room temperature.

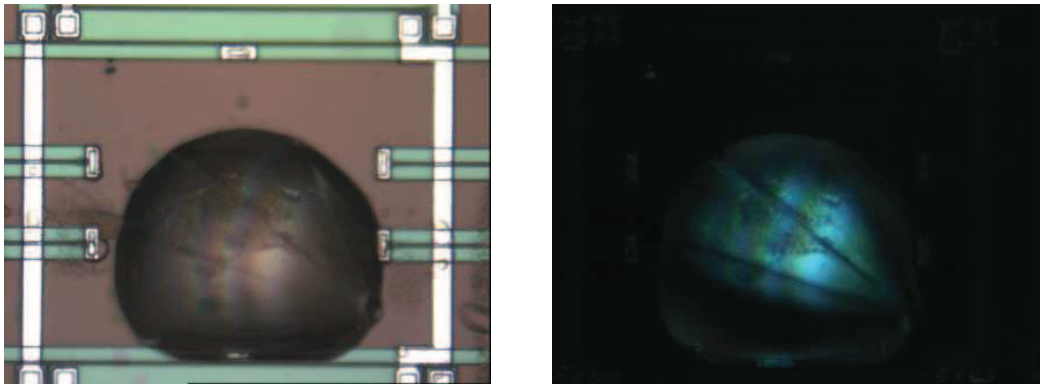

(a) PETN drop-like particle. (b) Same particle under polarized light.

Figure 4.41 – PETN drop-like particle after a touch with an eyelesh.

As far as TNT is concerned, we observed that this material behaves very similar to PETN, meaning that no crystallization process occurs during quenching and it to room temperature and that it can stay in a drop-like amorphous state until an external perturbation modifies its state.

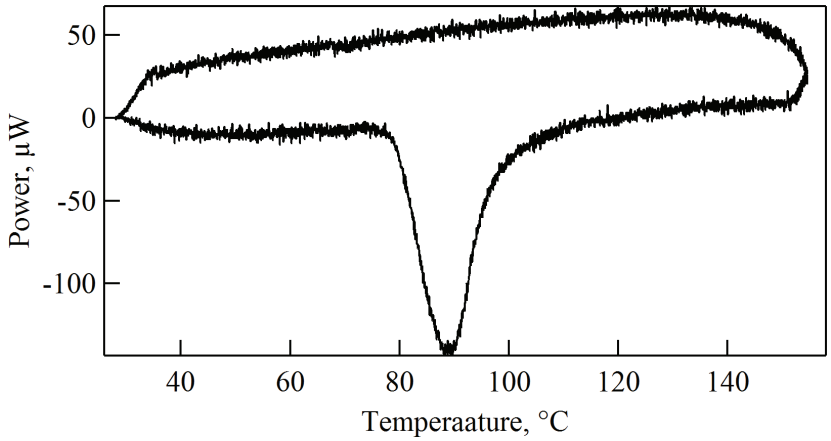

Figure 4.42 – Melting of a TNT single micro-sized particle during heating and no recrystallization observed in cooling.

4.5 Conclusions

This chapter is focused on a family of energetic materials previously tackled in Chapter 2.

The first part of the chapter shows the conventional DSC experiments and different methods to calculate the activation energy of the decomposition process.

To extend the range of the heating rates available, the nanocalorimetric experiments have been conducted at a series of different heating rates. Interestingly, most of the energetic materials studied in this work, with the exception of CL-20, are not undergoing decomposition during heating on the nanocalorimetric sensors whereas the same materials are well decomposing during conventional DSC heating ramps. One interesting feature observed for CL-20, which contradicts the statements proposed in the literature, is the fact of its melting before the decomposition. The melting event was evidenced also from the polarized light microscopy experiments. For the case of CL-20, a direct comparison of the conventional DSC and nanocalorimetric data becomes possible.

The temperature modulation experiments have been also performed on these materials. These measurements reveal the main transitions on heating as observed in fast heatings. However, the micron-sized particles sublimate before the temperature reaches the melting point. Therefore the only feature that can be used to distinguish the materials is the sublimation step on the modulation amplitude signal.

The last part of the chapter is dedicated to recrystallization studies. The setup combining nanocalorimetry and nano-focus X-ray scattering is helpful for understanding how the process of crystallization occurs in these materials.

[1] W. McCrone, *Analytical Chemistry* **1950**, *22*, 1225–1226.
[2] L. Minier, R. Behrens in, *Vol. 13*, 32nd JANNAF Comb. Subcommittee, **1995**.
[3] G. Pinheiro, V. Lourenco, K. Iha, *Journal of thermal analysis and calorimetry* **2002**, *67*, 445–452.
[4] J. Lee, C. Hsu, C. Chang, *Thermochimica Acta* **2002**, *392*, 173–176.
[5] V. Boddu, P. Redner, *Energetic Materials: Thermophysical Properties, Predictions, and Experimental Measurements*, CRC Press, **2010**.
[6] G. Long, B. Brems, C. Wight, *Thermochimica acta* **2002**, *388*, 175–181.
[7] R. Meyer, A. Homburg, *Explosives*, John Wiley & Sons, **2007**.
[8] V. Nedelko, N. Chukanov, A. Raevskii, B. Korsounskii, T. Larikova, O. Kolesova, F. Volk, *Propellants Explosives Pyrotechnics* **2000**, *25*, 255–259.
[9] M. Geetha, U. Nair, D. Sarwade, G. Gore, S. Asthana, H. Singh, *Journal of thermal analysis and calorimetry* **2003**, *73*, 913–922.
[10] J. Shen, W. Shi, J. Wang, B. Gao, Z. Qiao, H. Huang, F. Nie, R. Li, Z. Li, Y. Liu, et al., *Physical Chemistry Chemical Physics* **2014**, *16*, 23540–23543.
[11] C. Tarver, T. Tran, R. Whipple, *Propellants Explosives Pyrotechnics* **2003**, *28*, 189–193.
[12] P. Makashir, E. Kurian, *Journal of thermal analysis and calorimetry* **1999**, *55*, 173–185.
[13] M. Rosenthal, D. Doblas, J. Hernandez, Y. Odarchenko, M. Burghammer, E. Di Cola, D. Spitzer, A. Antipov, L. Aldoshin, D. Ivanov, *Journal of synchrotron radiation* **2013**, *21*, 223–228.
[14] G. Long, S. Vyazovkin, B. Brems, C. Wight, *The Journal of Physical Chemistry B* **2000**, *104*, 2570–2574.
[15] D. Patil, T. Brill, *Combustion and flame* **1993**, *92*, 456–458.
[16] A. Minakov, S. Roy, Y. Bugoslavsky, L. Cohen, *Review of scientific instruments* **2005**, *76*, 043906–043906.
[17] Z. Jiang, C. Imrie, J. Hutchinson, *Thermochimica acta* **2002**, *387*, 75–93.
[18] D. Moore, *Review of Scientific Instruments* **2004**, *75*, 2499–2512.
[19] V. Sinditskii, V. Y. Egorshev, V. Serushkin, A. Levshenkov, M. Berezin, S. Filatov, S. Smirnov, *Thermochimica Acta* **2009**, *496*, 1–12.

Chapter 5

Co-crystals of CL-20/TNT and CL-20/HMX

In this chapter a study on the crystallization and decomposition processes of two energetic co-crystals is presented. The main idea was to address how the structure formation takes place in the materials prepared using the Spray Flash Evaporation technique by using a combination of different techniques, such as conventional DSC, high-resolution X-ray powder diffraction, ultra-fast chip calorimetry and nano-focus X-ray diffraction.

Addressing fast structure formation and decomposition processes in smart energetic nano-sized co-crystals

Submitted to Advanced Functional Materials

Abstract

The interest toward co-crystals of energetic materials explains by the fact that they can offer better thermodynamic stability, lower and tunable sensitivity and detonation performance. In the present work, a combination of DSC, high-resolution X-ray powder diffraction, ultra-fast chip calorimetry and nano-focus was employed to address the thermal behavior and structure formation in the nano-sized co-crystals of CL-20 with HMX and TNT prepared using Spray Flash Evaporation (SFE). In the case of CL-20/TNT, the harsh preparation conditions of SFE result in deformation of the crystalline lattice as compared to crystallization from solution. Also, a small fraction of ϵ-CL-20 phase is detected, which can result from rapid crystallization of the superheated jets. The CL-20/HMX co-crystal does not reveal any thermal transitions up to the thermal decomposition. In contrast, CL-20/TNT exhibits an irreversible melting transition. Upon melting, it can crystallize at room temperature to form homo-crystals of CL-20. The first stage of the crystallization process happens within the first milliseconds after melting and results in generation of γ-CL-20 modification stable at high temperature. The solid-liquid phase separation occurring during heating of CL-20/TNT may explain its complex thermal decomposition process, the main exothermic peak of which can be assigned to that of a pure CL-20.

5.1 Introduction

In the last years, there has been a continuously growing interest toward co-crystallization [1], which has become a hot topic in many fields ranging

from pharmaceutics [2] to non-linear optics [3] and from ferroelectrics [4] to organic electronics [5]. In addition, co-crystallization has proven to have a significant potential for defence applications where development of insensitive high-energy explosives for modern weapon applications is targeted [6]. In this latter field, co-crystallization appears to be a particularly promising approach, as reported in a large number of papers published over the last years [7–14]. It allows tuning the key properties of the materials including density, sensitivity, and detonation performance [15]. Also, the co-crystallization can offer materials with higher thermodynamic stability than the pristine compounds [16]. The development of energetic co-crystals can also significantly contribute to other research fields such as photonics and quantum dot applications, where there is a need for novel materials such as nanodiamonds [17]. As the latter are produced by detonation, they could take advantage of the intimate molecular mixtures of energetic materials in the nano-sized co-crystals to open new lines of applications.

Recently, Spitzer et al. have employed the Spray Flash Evaporation (SFE) process to generate nano-co-crystals of explosive materials [18], the approach which was initially designed to elaborate nanoexplosives [19]. With the help of this method, different types of mixtures such as entirely crystalline composites, semi-crystalline mixtures and sub-micron and nano-sized co-crystals have been produced, depending on the type of molecular interaction between the initial compounds. In this work, we will focus on binary energetic co-crystals based on 2,4,6,8,10,12-hexanitro-2,4,6,8,10,12-hexaazaisowurtzitane (CL-20). These materials were shown to have a high potential for lowering sensitivity and thereby enhancing safety of the resulting energetic materials [13]. In particular, we will address an equimolar co-crystal of 2,4,6- trinitrotoluene (TNT) with CL-20, CL-20/TNT, and another with 1,3,5,7-tetranitro-1,3,5,7-tetraazacyclooctane (HMX), CL-20/HMX, at a molar ratio of 1:2. A combination of advanced methods of physical characterization such as in-situ nanocalorimetry and synchrotron-based nano-focus X-ray diffraction will be used among others to explore the fast structure formation processes in the co-crystals under conditions close to those of detonation, which can shed light on the decomposition mechanisms in these materials.

5.2 Results and Discussion

Morphological and structural characterization of the energetic materials

The samples of ϵ-CL-20, TNT and β-HMX were firstly characterized with a solid-state NMR and Raman spectroscopy. The acquired spectra confirmed the expected structure and purity of the materials; they are given in Chapter 2. The morphology of the energetic materials was further examined with SEM (Figure 5.1).

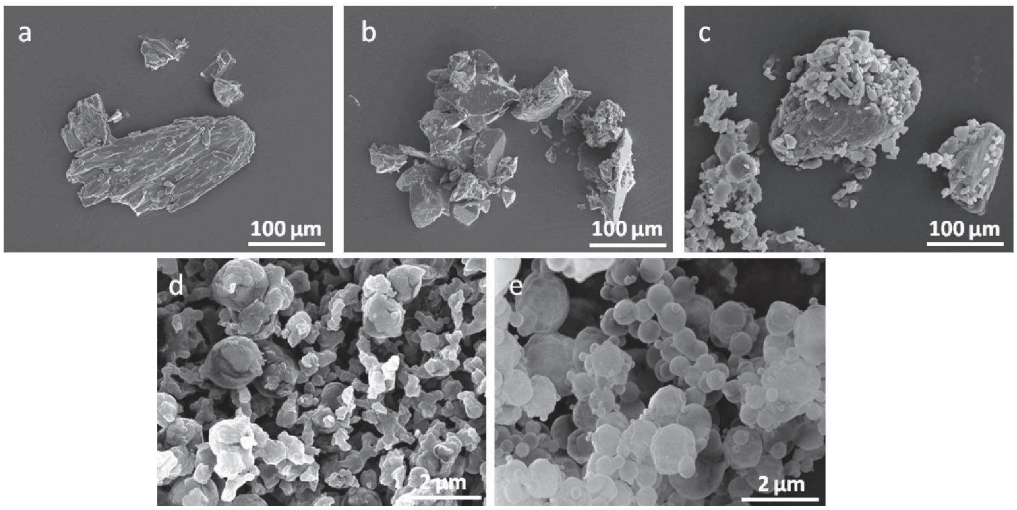

Figure 5.1 – SEM micrographs of pure explosives and co-crystals, (a) TNT, (b) ϵ-CL-20, (c) β-HMX, (d) CL-20/TNT and (e) CL-20/HMX.

The micro-particles of TNT and ϵ-CL-20 clearly reveal the facets characteristic of single crystals whereas the ones of β-HMX seem more heterogeneous in shape and size. However, it is clear that the shape of crystals *per se* is not always sufficient to conclude on their texture. Therefore, additional analyses have been performed on the synthesized micro-crystals using nano-focus X-ray diffraction. The supports used to deposit the particles are the nanocalorimetric sensors that will be used further to explore fast structure formation processes in the co-crystals with nanocalorimetry and nano-focus X-ray diffraction. The home-built setup for performing combined

nanocalorimetry / nano-focus X-ray scattering (cf. Figure 5.2a) developed in our group [20, 21] allows obtaining simultaneously the thermodynamic and structural information on nano-gram-sized samples such as micro-crystals of explosives. To make the home-built nanocalorimeter compatible with the environment of the nano-focus X-ray beamline, several severe constraints had to be met (cf. Figure 5.2b). More technical details on the combined measuring set-up can be found in the experimental section of the paper.

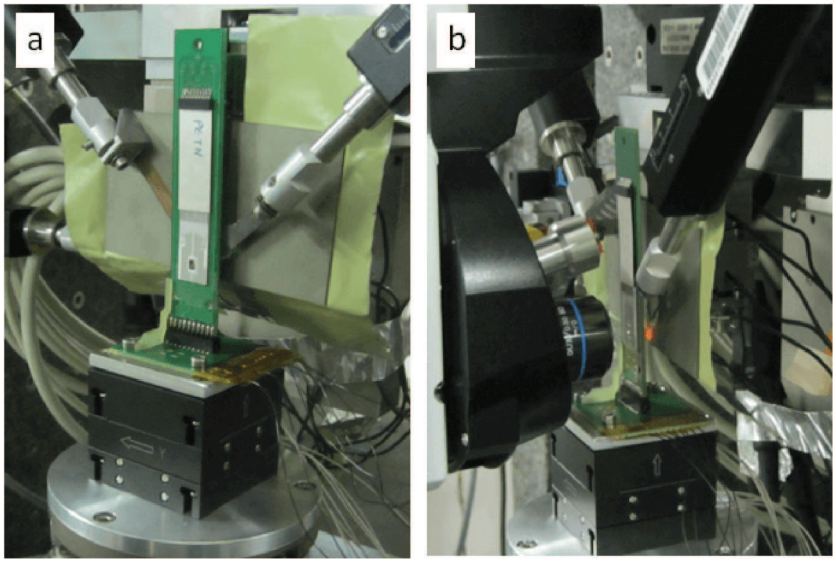

Figure 5.2 – (a) Front view of the experimental set-up for combined Nanocalorimetry and nano-focus X-ray scattering. (b) Side view of the nanocalorimetric sensor holder positioned at the working distance with an on-axis optical microscope and illuminated aperture shield put in place. The photo shows the geometrical constraints imposed on the nanocalorimetric sensor holder by the beamline environment

Figure 5.3 shows the so-called mesh scans that were obtained by scanning micro-particles of the pristine explosive materials in 2D with a nano-focus X-ray beam. To appreciate the crystal texture, selected regions of the diffractograms containing only one strong peak have been stripped out of the patterns and overlaid with the micrograph of the sample. It can be seen that the selected reflection exhibits invariable intensity over a significant fraction of the particle surface. This testifies that the studied particles have a pronounced

single-crystalline texture.

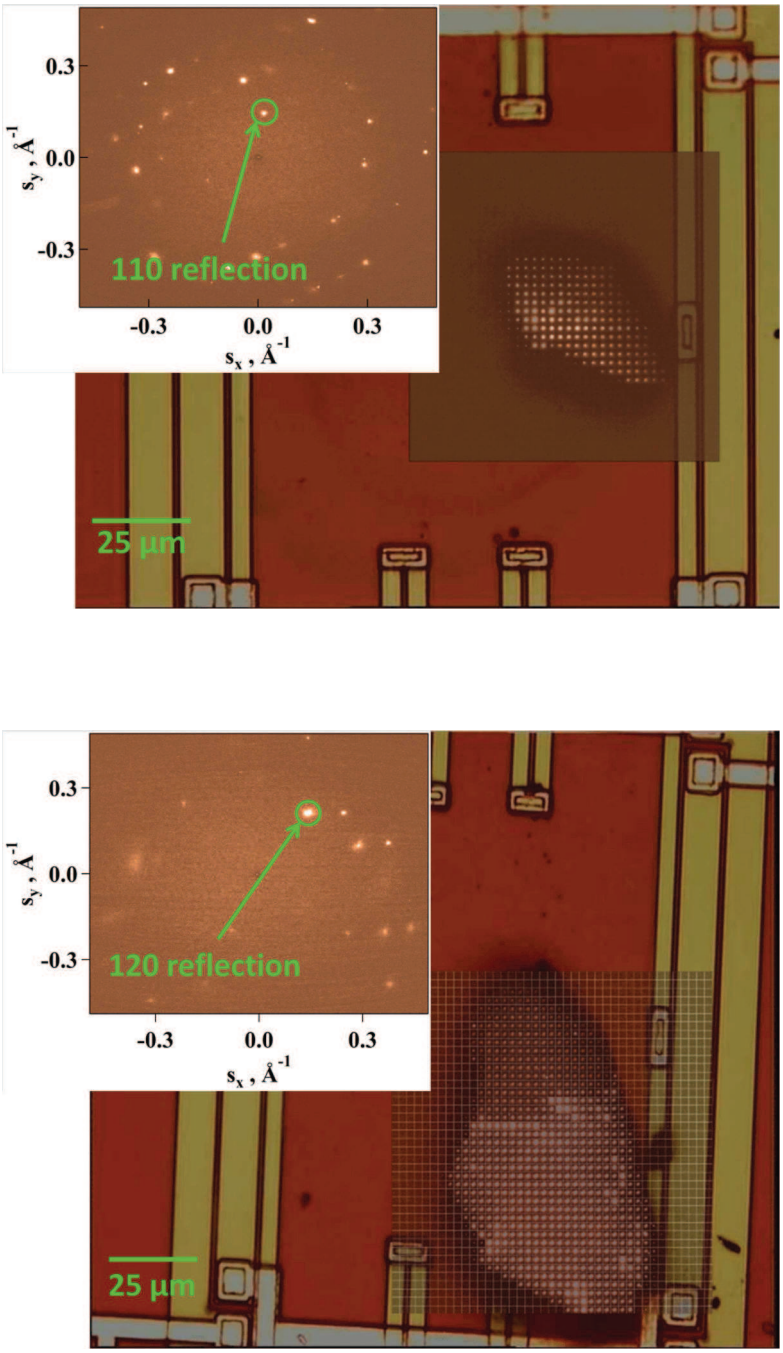

Figure 5.3 – 2D scans performed with a nano-focus X-ray beam on micro-particles of ϵ-CL-20 (top) and β-HMX (bottom).

To create these images, the diffraction intensity corresponding to a selected reflection of the sample such as 110 peak of the ϵ-CL-20 phase and 120 reflection of the β-HMX phase was chosen (cf. the insets of the top and bottom panels, respectively). The zone of interest with the selected reflection was cut out of each of the 2D nano-focus diffractograms and plotted at the corresponding position of the sample, which was scanned with an X-ray beam with a step of 2 µm. The micrographs of the samples deposited on XEN-39392 nanocalorimetric sensors are overlaid with the corresponding X-ray mesh scans. The uniformity of the X-ray intensity reveals the single-crystalline nature of the particle under study.

The binary co-crystals prepared by the Spray Flash Evaporation technique are shown in Figure 5.1. They are much smaller in size than the particles of the pure energetic materials and do not reveal any crystal habit. The formation of such morphology can be accounted for by harsh conditions of the co-crystals preparation during SFE; these conditions are obviously very different from solution crystallization used to produce such materials previously [8, 9]. The co-crystals' size histograms shown in Figure 5.4 allow concluding that the particles are in the nanometer range and that the CL-20/TNT particles (the most probable particle size is 100 nm) are bigger than those of the CL-20/HMX (58 nm).

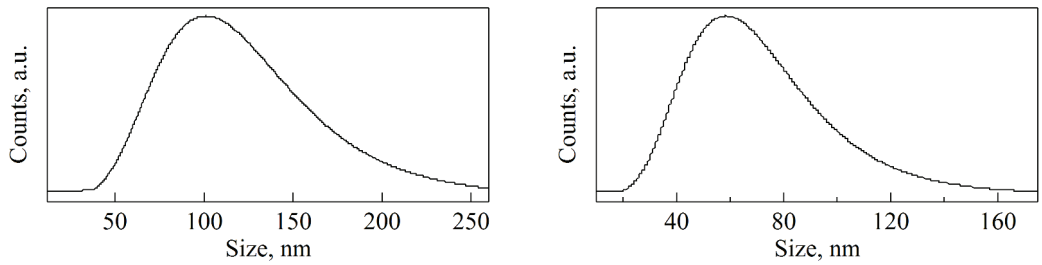

(a) CL-20/TNT. (b) CL-20/HMX.

Figure 5.4 – Particle size distribution of co-crystals (f) CL-20/TNT and (g) CL-20/HMX. Notice the different mean sizes of co-crystal particles (100 and 58 nm for CL-20/TNT and CL-20/HMX, respectively).

X-ray Powder Diffraction

The structure of the co-crystals synthesized by the Spray Flash Evaporation process was characterized by high-resolution X-ray powder diffraction.

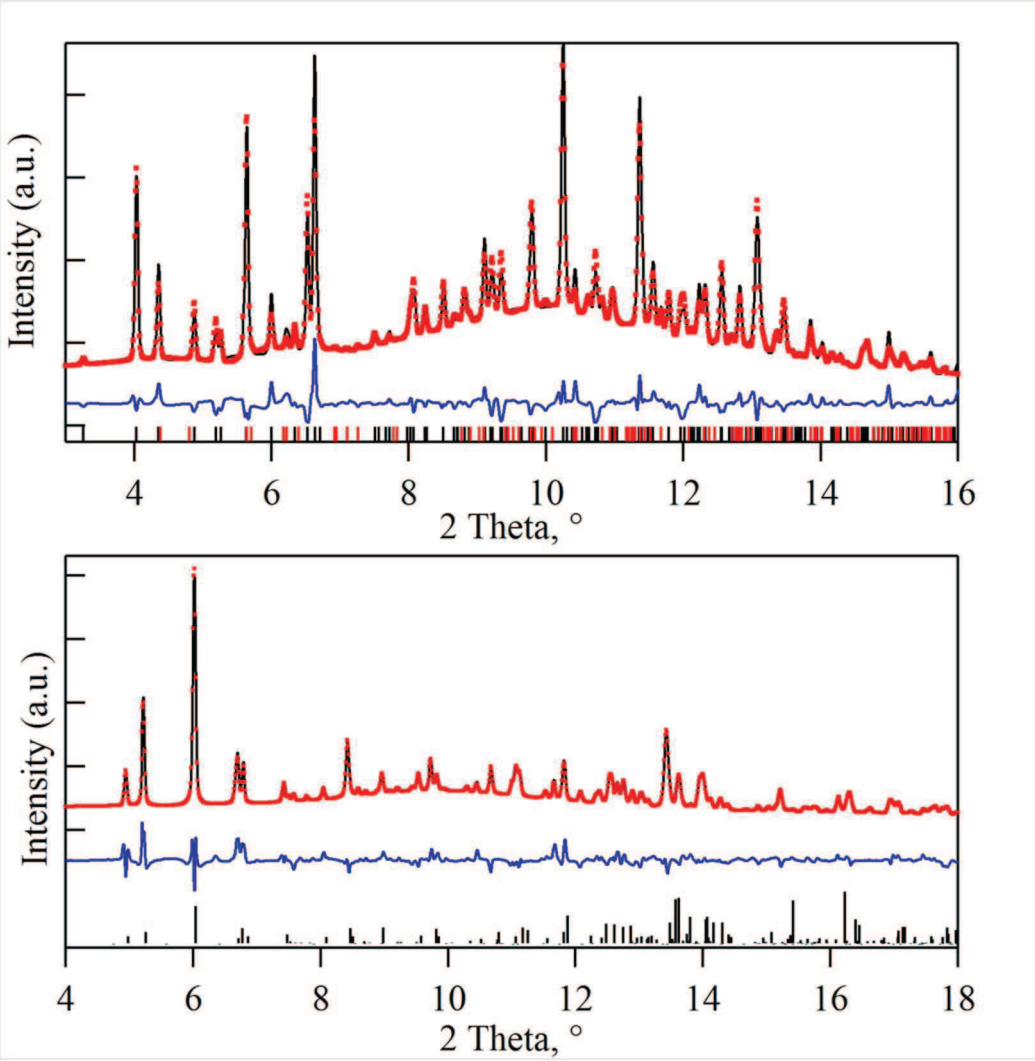

Figure 5.5 – X-Ray Powder Diffractograms of CL-20/TNT (top) and CL-20/HMX (bottom). In black solid lines are plotted the diffraction patterns described in the literature. Red solid lines show the experimental data measured at BM01A (ESRF). Blue solid lines show the difference between literature and experimental data. Black sticks represent the peak position of the pure compounds. In the case of CL-20/TNT, it is displayed (red sticks) also the peak position of ϵ-CL-20.

Figure 5.5 displays the experimental diffraction curves of the compounds together with the results of modeling. Interestingly, although for the case of CL-20/HMX the experimental diffraction data agrees very nicely with the literature report given in ref. [9], modeling the structure of CL-20/TNT posed more problems. Thus, it was found that in order to match the peak positions, the unit cell of the co-crystal has to be deformed essentially along the a- and c-directions. The resulting unit cell parameters are the following: a=9.6778±0.0007 Å, b=19.8053±0.0015 Å and c=24.5140±0.0019 Å. By comparing these parameters with the ones reported for a room-temperature measurement in ref. [8], it can be seen that in our case the a- and c-parameters are contracted by 0.9 and 0.8%, respectively, with the overall crystal density being higher than the literature value by about 2%. According to the interpretation given in ref. [8], packing along the b-parameter involves interactions between the molecules of CL-20 and TNT while interactions along the c-direction occur essentially between the adjacent CL-20 molecules. Therefore, it can be deduced that the Spray Flash Evaporation technique results in a structure distortion involving both the interactions between CL-20 and TNT molecules and those between the neighboring CL-20 molecules.The temperature-dependent structural data provided in ref. [8] show that the b-parameter is the most labile as it exhibits the highest thermal expansion (2.53%) when one compares the measurement at the liquid-nitrogen and room temperatures. Therefore, the distortion of b due to the harsh preparation conditions would not be very surprising. However, the difference in the c-parameter is more striking as it proves to be the most stable with temperature variation. More experiments will be required to understand what could be the associated variation in the mutual orientation of the CL-20 molecules in the co-crystal. Moreover, the analysis of the diffraction curve shows that the co-crystal structure alone cannot account for all the diffracted intensity and addition of a small fraction of a pure ϵ-CL-20 (3.11 ± 0.82%) phase is required. We speculate that despite the rapid pressure drop, the fast crystallization of ϵ-CL-20 cannot be fully avoided in a superheated jet directed to the atomization chamber resulting in formation of a small fraction of CL-20 homo-crystals.

Thermal behavior of the co-crystals

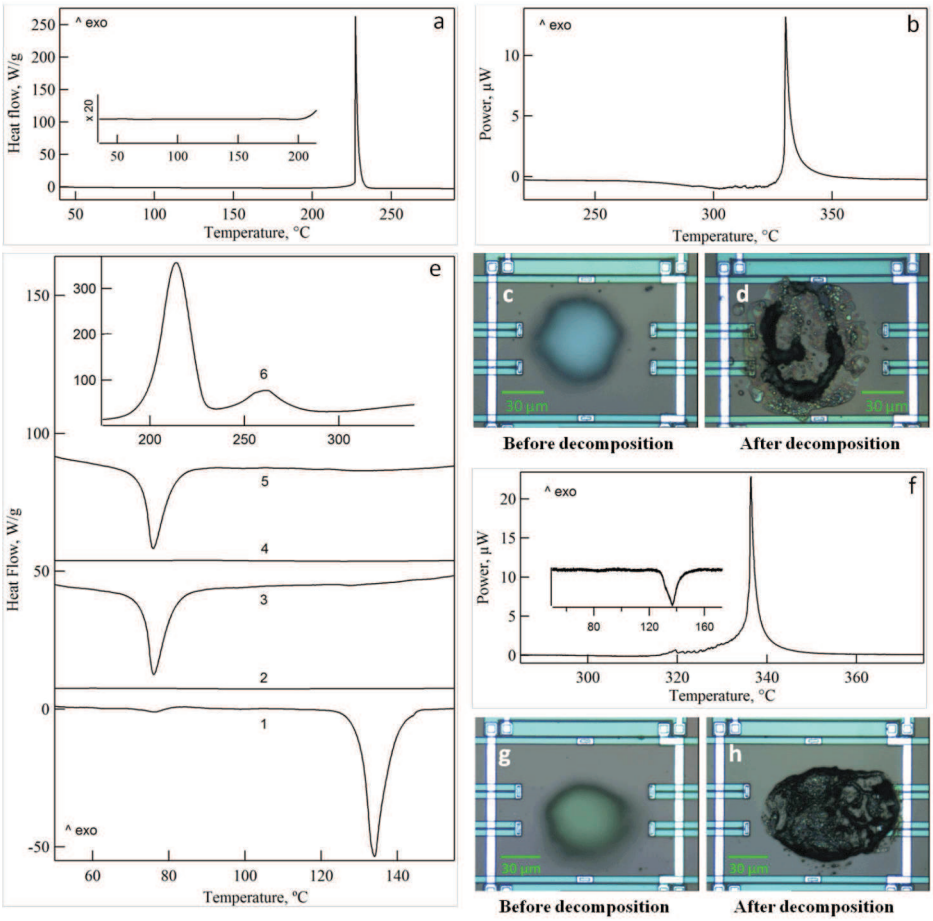

Figure 5.6 – (a) Conventional DSC heating ramp performed on CL-20/HMX. (b) Fast heating ramp of a CL-20/HMX micro-particle using fast chip calorimetry (c,d) State of the particle before and after the experiment performed in (b), (e) Conventional DSC heating and cooling curves performed in CL-20/TNT. (1) initial heating up to 160 °C shows melting of the co-crystal structure, (2) cooling from 160 °C to room temperature giving no evidence of crystallization. (3) Second heating to the same temperature showing melting of TNT and the absence of the co-crystal melting, (4) second cooling similar to the one in (2), (5) third heating up to 340 °C showing melting of TNT. The inset (6) shows the decomposition peaks corresponding to CL-20 and TNT. (right) (f) Nanocalorimetric curve of a CL-20/TNT co-crystal and the corresponding morphology of the particle before (g) and after (h) the experiment.

The thermal properties of the co-crystals were studied with conventional DSC and nanocalorimetry using the heating rates of 5 °C/min and 1000 °C/s, respectively.

The CL-20/HMX co-crystal reveals only one strong exothermic peak corresponding to the thermal decomposition (cf. Figure 5.6 a and b). A close-up of the conventional DSC curve up to the decomposition peak is given in the inset in panel a) to show the absence of any noticeable thermal transitions. In the nanocalorimetric measurement, the curve is qualitatively similar showing somehow a small instability of the baseline just before the decomposition. This can be explained by some wiggling of the micro-particle on the sensor due to the intensifying sample sublimation. The comparison of the conventional DSC and nanocalorimetric measurements reveals a displacement of the decomposition peak toward high temperatures, which can be accounted for by a difference of the heating rates by approximately 10,000 times. The absence of the melting point of the co-crystal before decomposition is in agreement with the data reported in ref. [9]. Such behavior is reminiscent of the pure CL-20 and therefore can be attributed to the composition of this co-crystal that is rich in CL-20. In addition, the structure can be further stabilized by strong hydrogen bonds reported previously [8]. The change of the particle morphology due to the thermal decomposition can be appreciated from the micrographs given in panels c) and d) of Figure 5.6. It can be seen that the decomposition is accompanied by a dramatic change of the micro-particle shape and that a solid carbonaceous residue stays on the sensor upon cooling to room temperature. The latter is typical of the CL-20 decomposition [22].

The CL-20/TNT co-crystal has a richer thermal behavior: it exhibits a melting transition with an onset at 130.0 °C (cf. curve 1 in panel e of Figure 5.6). However, once molten, the co-crystal does not recrystallize in the same form again upon cooling to 0 °C (not shown here) (cf. curve 2 in panel e). Instead, one can observe only the melting peak characteristic of the pure TNT crystal (cf. curve 3 in panel e). The subsequent cooling from 160 °C is also featureless (cf. curve 4 in panel e), and the third heating ramp (cf. curve 5 in panel e) exhibits again only the melting of TNT and decomposition peak. The latter exhibits a complex shape (cf. curve 6 in

panel e), which may be ascribed to the decomposition processes of pure CL-20 (stronger peak) and that of TNT (weaker peak). The melting transition of the co-crystal is also nicely visible in the nanocalorimetric curve (cf. panel f of Figure 5.6). The shape of the decomposition peak is however different in the nanocalorimetric curve, which is probably due to evaporation of TNT at these high temperatures. The absence of TNT at the moment of decomposition on the nanocalorimetric sensor can also be inferred from a more compact morphology of the carbonaceous residue (cf. panel h of Figure 5.6) and also from the comparison of the micro-RAMAN spectra measured on the residues left by decomposition of the co-crystal and pure ϵ-CL-20 (Figure S2).

Crystallization behavior of CL-20/TNT

The interesting thermal behavior of the co-crystal in question prompted us to investigate it in some more detail.

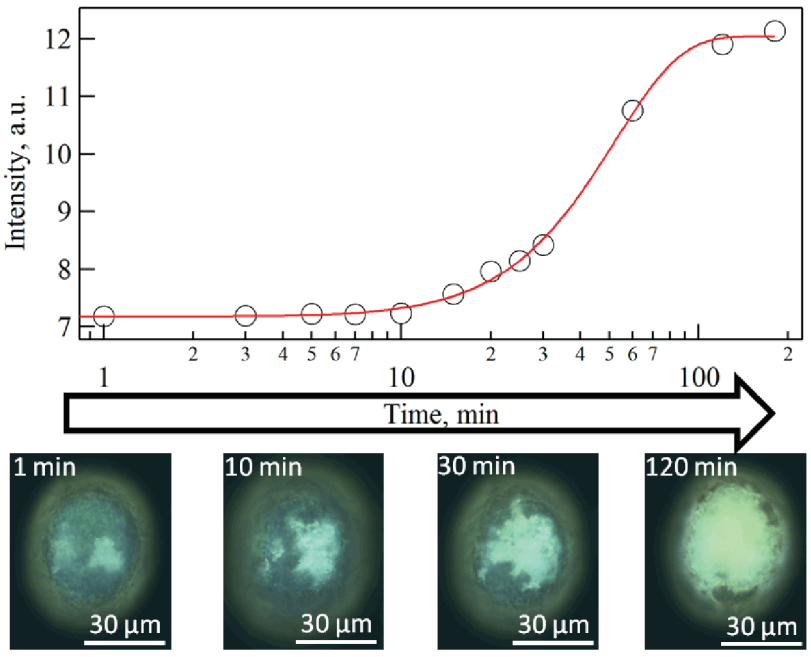

Figure 5.7 – (top) Kinetics of the crystallization process of a molten single particle of CL-20/TNT co-crystal after quenching from 150 °C to R.T. Experimental data have been fitted using Avrami equation. (bottom) POM micrographs at different states of the crystallization process.

Figure 5.7 displays the micrographs of a droplet of the co-crystal brought to room temperature after a short-term heating to 150 ℃, i.e. above the melting point. The images recorded in polarized light allow visualizing the increase of the sample birefringence with time, which is caused by room-temperature crystallization.

It can be seen that the crystallization is almost complete after about 2 hrs. The overall kinetics of crystallization can be quantified by modelling the integral light intensity with Avrami equation:

$$I(t) = I(t_0) + (I(t) - I(t_0))(1 - \exp(-K(t - t_0)^n)) \tag{5.2.1}$$

The results of the fit with Equation 1 give n=1.9 and K=$5.2{\cdot}10^{-4}$ (s^{-n}). The value of the Avrami coefficient, which is close to two, can be interpreted in the case of athermal nucleation as a 2D-confined growth, which may correspond to formation of flat lamellar-like crystals. Since it was found that the co-crystal does not recrystallize after melting and that TNT can crystallize only at much lower temperatures, the described kinetics should reflect exclusively the formation of CL-20 crystals. Interestingly, some birefringence is present in the droplet at the very beginning of the process and therefore cannot be studied with this method.

Study of the fast stage of the structure formation in CL-20/TNT

In order to understand what happens during the very early stage of the structure formation, a combination of nanocalorimetry and nano-focus X-ray diffraction has been employed. The methodology of the experiment and the results obtained are depicted in Figure 5.8.

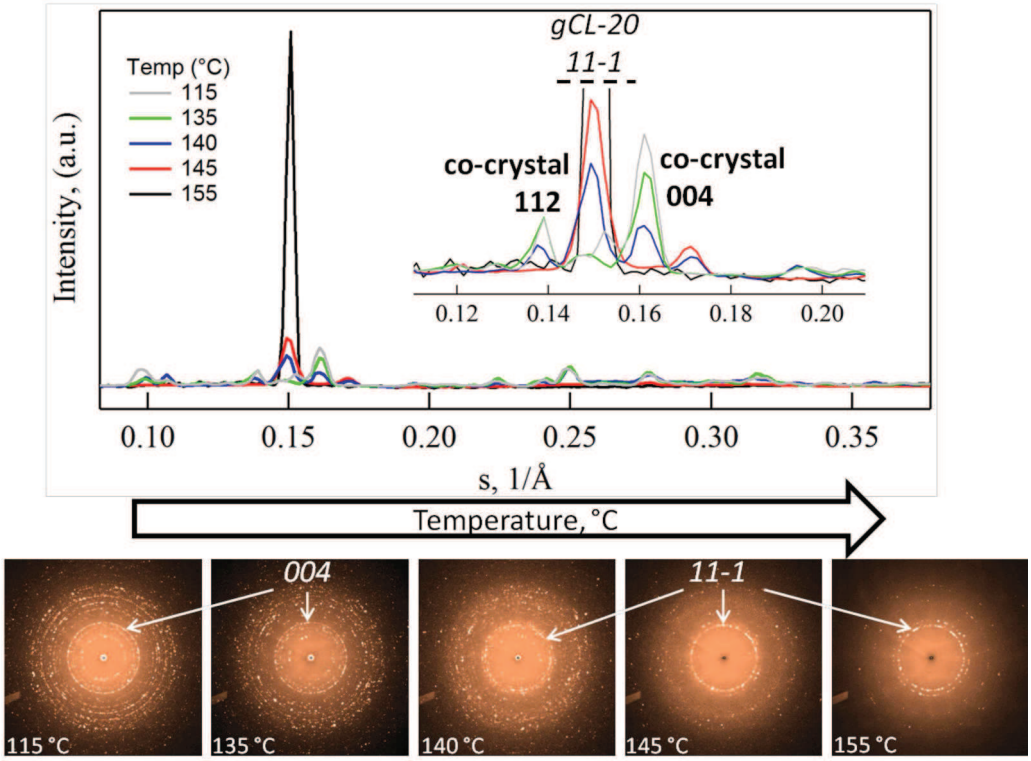

Figure 5.8 – (top) Selected 1D-reduced WAXS profiles probing the structure of the co-crystal and its morphological evolution upon melting. The two first patterns recorded after heating to 115 and 135 °C, respectively, show the characteristic crystalline phase of the co-crystal, while the others contain mainly crystals of γ-CL-20. (bottom) Selected 2D-WAXS patterns corresponding to the 1D-reduced profiles shown above. At lowest temperature, the patterns show a quasi-powder diffraction distribution which evolves during the corresponding experiments recorded at higher temperatures.

In this case, a small amount of co-crystal was heated from room temperature to an increasingly higher annealing temperature (T_{ann}) at a rate of 2000 °C/s. Upon dwelling for 10 milliseconds at Tann, the sample was cooled back to room temperature at the same rate and analyzed with nano-focus X-ray diffraction. The representative 2D X-ray patterns are given in the bottom row of Figure 5.8. It can be observed that for the annealing temperatures up to 140 °C the 112 and 004 peaks of the co-crystal located at s = 0.139 and 0.161 $Å^{-1}$, respectively, are visible in the diffractograms showing that the co-crystal is still present in the sample. However, when the annealing

temperature increased the co-crystal' peaks start to disappear while some new peaks grow up. The analysis of the peaks' position allows assigning the new peaks to the γ-phase of CL-20. In particular, in the chosen angular region one can see an increase in the amplitude of the 11-1 peak of the γ-phase, which is for example absent in ϵ-CL-20, the most stable polymorph at room temperature [23]. Also, another diffraction peak pertinent to γ-CL-20 is visible at the s-value of ca. 0.17 $Å^{-1}$ (i.e., 111 peak). Therefore, one can suggest that during annealing of the co-crystal melt, the nuclei of the γ-CL-20 are generated and that they give rise to the growth of this polymorph, the formation of which is unusual at room-temperature [24]. Importantly, if there would be ϵ-CL-20 crystals forming in the melt they will not be converted to the γ-CL-20 at the annealing temperatures used in the experiment [25] and will therefore be observable. This shows that even a very short dwelling time in the melt is sufficient to nucleate the γ-phase of CL-20 to the extent that overtakes the crystal growth at room temperature, as was shown above with the optical microscopy experiments.

The solid-liquid phase separation occurring during heating the melt of the CL-20/TNT co-crystal may explain its complex thermal decomposition process exhibiting two strong exothermic peaks (cf. curve 6 in panel e of Figure 5.6). The low-temperature peak is positioned rather close the decomposition peak of pure CL-20. Given that the weight fraction of CL-20 in the co-crystal is ca. 65.9%, the enthalpy of the first peak (3,500 J/g) is rather close to what is expected for the pure CL-20 decomposition. In contrast, the second peak of the decomposition process is somewhat lower in temperature than the decomposition peak of pure TNT, which means that CL-20 may trigger the decomposition process of TNT. The comparison of the decomposition processes in the two co-crystals studied in this work emphasizes the role of the solid-liquid phase separation occurring in the CL-20/TNT co-crystal melt on heating. This shows that in-situ exploration of the structure formation processes can be helpful in understanding the decomposition behavior of energetic materials.

5.3 Conclusions

In summary, the structure and thermal behavior of binary nano-sized co-crystals of CL-20 with HMX and TNT prepared using Spray Flash Evaporation (SFE) was investigated. For the CL-20/TNT co-crystal, the SFE fabrication technique results in deformation of the crystalline lattice of the compound when compared to the same material crystallized from solution. A small fraction of ϵ-CL-20 phase is found to be present in the sample, which can result from rapid crystallization of the superheated jets. As far as the thermal behavior is concerned, the CL-20/HMX co-crystal does not reveal any thermal transitions up to the thermal decomposition. In contrast, CL-20/TNT exhibits an irreversible melting transition. Upon melting, the material can undergo crystallization at room temperature to form homo-crystals of CL-20. It was observed that the first stage of the crystallization process is very rapid. To address the very onset of the crystallization process occurring within the first milliseconds after melting, a combination of in-situ nanocalorimetry and nano-focus X-ray diffraction was employed. It was observed that the rapidly-formed crystals correspond to the γ-CL-20 modification, which is stable at high temperature. This observation is probably the first study of crystallization of CL-20, which occurs not from solution. The solid-liquid phase separation occurring during heating of CL-20/TNT may explain its complex thermal decomposition process, the main exothermic peak of which can be assigned to that of a pure CL-20.

5.4 Experimental Section

Preparation of co-crystals: The co-crystals were prepared by means of the Spray Flash Evaporation technique [18, 19, 26]. The process makes use of a solution where the pristine compounds are dissolved. By applying an overpressure to the solution, the superheated liquids are directed to an atomization chamber where the pressure is much lower, causing the "flash evaporation" of the solvent which induce the crystallization of the solute. The pressure drop is accompanied also by a temperature drop, from the hot nozzle (160 °C) to the

cold spray outlet (-30 ℃) which prevents the growth of the nano-cocrystals. The final products are separated in a continuous way using a setup of parallel axial cyclones. The yield (%) of the process is 43.8 and 46.1 for CL-20/TNT and CL-20/HMX, respectively.

Combined Nanocalorimetry- Nano-focus X-ray scattering: The home-built nanocalorimetric accessory has been designed compatible with the sample environment at the synchrotron beamlines employing nano-focused X-ray beams. The nanocalorimetric experiments can be realized, thanks to the home-built controller capable of applying custom temperature programs to the heaters of the nanocalorimetric sensor and performing fast readout of the thermopile signal of the sensor. The controller is operational from a computer running under Windows. For experiments at a synchrotron, the controller operation can be performed distantly (e.g., via a Remote Desktop using an Ethernet connection). Importantly, in the setup, the sensor holder is physically separated from the controller. This feature allows making the X-ray scattering experiments in transmission with our setup. For the in-situ X-ray scattering measurements, the sensor holder with the nanocalorimetric sensor plugged in is precisely positioned with the help of a special sample stage, including a hexapod and an array of piezo-actuators (Cube). The sample position can be monitored using an on-axis optical microscope, exchangeable with an X-ray detector. Nano-beam X-ray scattering experiments have been carried out at the ID13 beamline of the European Synchrotron Radiation Facility (ESRF). Focusing of the X-ray beam down to below 100 nm is achieved with a Fresnel zone plate placed 98 m downstream the undulator source. Sample positioning and rastering is achieved with a miniature hexapod for coarse sample positioning and alignment, while the high-resolution scanning of the sample was performed with the Cube. The nanobeam experiments were carried out using X-ray photons with an energy of 14.9 keV. During high-resolution mapping in the nanobeam X-ray experiments, the 2D diffraction data were collected using a large-area integrating FreLon CCD detector. Several diffrac-

tion peaks of silver behenate and corundum were used to calibrate the norm of the scattering vector s ($|s| = 2\sin(\theta)/\lambda$, where θ is the Bragg angle and λ the wavelength) in the small and wide angle regions. The acquired data were reduced and corrected using protocols provided by the beamline. The data analysis including two dimensional integration and visualization was done using home build routines developed in the Igor Pro software package.

X-ray powder diffraction: Single-crystal diffraction was measured at the Swiss-Norwegian Beamlines of the ESRF. The X-ray patterns were collected with a PILATUS 2M pixel area detector using a monochromatic beam at a wavelength of $\lambda = 0.69411$ Å, which was slit-collimated down to 100×100 µm^2. The sample-to-detector distance and parameters of the detector were calibrated using a LaB6 NIST standard. The detector images were recorded by phi-scans in shutter-free mode with a 0.1 deg angular step. The data were preprocessed by SNBL Tool Box and then by CrysAlis Pro (Agilent Technologies, version 171.36.24). The data was refined with SHELX.

DSC measurements: A heat-flux DSC, Mettler-Toledo DSC 1, was used to characterize the energetic materials used in this paper. Heating rates employed were 5 K min^{-1}. The power resolution of the device is 0.4 µW while the temperature accuracy is 0.2 K. High-pressure crucibles DSC-M20 gold-plated crucibles of 20 microliters from Swissi were used due to the high pressure generated during the decomposition of the materials. The crucibles can stand up to 217 bars.

Polarized Optical Microscopy: The observations have been carried out using a Leica DM2500M microscope equipped with a Sony DXC-390P camera in

reflection geometry. The camera employs a 1/3" type DSP 3-chip charge-coupled device (CCD) sensor to display the images.

[1] A. Bond, *CrystEngComm* **2007**, *9*, 833–834.
[2] N. Qiao, M. Li, W. Schlindwein, N. Malek, A. Davies, G. Trappitt, *International Journal of pharmaceutics* **2011**, *419*, 1–11.
[3] E. Choi, M. Jazbinsek, S. Lee, P. Günter, H. Yun, S. Lee, O. Kwon, *CrystEngComm* **2012**, *14*, 4306–4311.
[4] A. S. Tayi, A. Shveyd, A.-H. Sue, J. Szarko, B. Rolczynski, D. Cao, T. Kennedy, A. Sarjeant, C. Stern, W. Paxton, et al., *Nature* **2012**, *488*, 485–489.
[5] L. Zhu, Y. Yi, Y. Li, E. Kim, V. Coropceanu, J. Brédas, *Journal of the American Chemical Society* **2012**, *134*, 2340–2347.
[6] A. Sikder, N. Sikder, *Journal of hazardous materials* **2004**, *112*, 1–15.
[7] K. Landenberger, A. Matzger, *Crystal Growth & Design* **2010**, *10*, 5341–5347.
[8] O. Bolton, A. Matzger, *Angewandte Chemie International Edition* **2011**, *50*, 8960–8963.
[9] O. Bolton, L. Simke, P. Pagoria, A. Matzger, *Crystal Growth & Design* **2012**, *12*, 4311–4314.
[10] H. Li, Y. Shu, S. Gao, L. Chen, Q. Ma, X. Ju, *Journal of molecular modeling* **2013**, *19*, 4909–4917.
[11] K. Landenberger, O. Bolton, A. Matzger, *Angewandte Chemie International Edition* **2013**, *52*, 6468–6471.
[12] D. Spitzer, B. Risse, F. Schnell, V. Pichot, M. Klaumünzer, M. Schaefer, *Scientific reports* **2014**, *4*.
[13] Z. Yang, Q. Zeng, X. Zhou, Q. Zhang, F. Nie, H. Huang, H. Li, *RSC Advances* **2014**, *4*, 65121–65126.
[14] Y. Wang, Z. Yang, H. Li, X. Zhou, Q. Zhang, J. Wang, Y. Liu, *Propellants Explosives Pyrotechnics* **2014**, *39*, 590–596.
[15] N. Schultheiss, A. Newman, *Crystal growth and design* **2009**, *9*, 2950–2967.
[16] Y. Gao, H. Zu, J. Zhang, *Journal of Pharmacy and Pharmacology* **2011**, *63*, 483–490.
[17] V. Pichot, B. Risse, F. Schnell, J. Mory, D. Spitzer, *Scientific reports* **2013**, *3*.
[18] B. Risse, D. Spitzer, D. Hassler, F. Schnell, M. Comet, V. Pichot, H. Muhr, *Chemical Engineering Journal* **2012**, *203*, 158–165.
[19] B. Risse, D. Hassler, D. Spitzer, Preparation of nanoparticles by flash evaporation, US Patent 20,150,000,846, **Jan. 2015**.

[20] M. Rosenthal, D. Doblas, J. Hernandez, Y. Odarchenko, M. Burghammer, E. Di Cola, D. Spitzer, A. Antipov, L. Aldoshin, D. Ivanov, *Journal of synchrotron radiation* **2013**, *21*, 223–228.

[21] C. Riekel, E. Di Cola, M. Reynolds, M. Burghammer, M. Rosenthal, D. Doblas, D. Ivanov, *Langmuir* **2015**.

[22] V. Nedelko, N. Chukanov, A. Raevskii, B. Korsounskii, T. Larikova, O. Kolesova, F. Volk, *Propellants Explosives Pyrotechnics* **2000**, *25*, 255–259.

[23] U. Nair, R. Sivabalan, G. Gore, M. Geetha, S. Asthana, H. Singh, *Combustion Explosion and Shock Waves* **2005**, *41*, 121–132.

[24] Y. T. Lapina, A. Savitskii, E. Motina, N. Bychin, A. Lobanova, N. Golovina, *Russian Journal of Applied Chemistry* **2009**, *82*, 1821–1828.

[25] M. Geetha, U. Nair, D. Sarwade, G. Gore, S. Asthana, H. Singh, *Journal of thermal analysis and calorimetry* **2003**, *73*, 913–922.

[26] B. Risse, D. Hassler, D. Spitzer, Preparation of nanoparticles by flash evaporation, WO Patent App. PCT/EP2013/052,478, **Aug. 2013**.

Chapter 6

Final conclusions

The aim of this work was to explore the potential of Nanocalorimetry in the field of detection of explosive materials. It is noteworthy that at the present moment, the problem of the explosives detection in public places is still unsolved. The existing detection devices do not meet all the criteria required to be considered as the "ultimate" detection device that can operate with satisfactory speed and sensitivity. One of the aspects of this problem is related to detection of solid particles of explosives, which can be in the state of traces.

If one thinks of using a nanocalorimeter for such purposes, it is important to propose the operation mode that would be optimized in terms of sensitivity and specificity. Generally, our home-built nanocalorimeter provides two different working modes that can be used for this purpose:

- DC calorimetry where the samples are heated in the same manner as in conventional calorimetry experiments, i.e. at constant heating rates, but several orders of magnitude faster.
- Modulated regimes (AC calorimetry) where reversing and non-reversing components of the heat capacity can be measured by using on-time Fourier analysis of the signal.

In the present work, we have tested the most common energetic materials

in both modes to understand whether the nanocalorimetric curve can in principle help to constitute a library of the thermal signatures of the explosive materials used in terrorist attacks.

It should be mentioned that detection of explosives in the solid state can be thought of as being more promising as compared to the vapor detection due to relatively low vapor pressures of the most common explosives at room temperature. This makes nanocalorimetry a candidate for one of the interesting detection techniques because, as it is shown in the present work, performing measurements on single micro-particles of these materials, which are in the range of a few nano-grams, is feasible. The melting points determined by nanocalorimetry are in agreement with the known characteristics of the materials under study, which unequivocally shows that they can be used as a first approach to establishing the thermal signatures library of the explosives. Last but not least, one has to mention the capacity of the nanocalorimeter to perform high throughput measurements. For example, a typical heating ramp in our case can be completed in just a few milliseconds.

Although there is still a lot of room for improvement. One of the remaining issues of using Nanocalorimetry is the precise sample positioning on the sensors used to perform the measurements and the heat profile to apply. These aspects have to be considered because, as it was shown, even for an area of 100×100 μm^2 the thermal gradients during fast heating ramps can be considerable.

It was observed that the AC calorimetric experiments performed on micro-particles of explosives do not always reveal the thermal transitions that can help identifying these materials. In particular, depending on the size of the micro-particles, one can observe for example exclusively the thermal events related to sample sublimation. In this case, the observed transition visible as a step in the heat capacity cannot constitute the thermal signature of an explosive material because it would not be specific to the sample chemical composition. By contrast, the use of linear heating rates, especially high heating rates, is much more convenient because it allows separating the thermodynamic events (e.g., melting) from kinetic events (e.g., decomposition).

Importantly, in most cases the high heating rates allow observing the sample melting before the micro-particle is sublimated completely. Observation of melting transitions is essential as it can help to acquire the required specificity in the analysis. Therefore the use of DC regimes is certainly preferable from the viewpoint of the explosives detection. This particular feature can make Nanocalorimetry a potentially interesting complementary technique for the explosives detection.

Nowadays, nanocalorimetry has become a very interesting technique not only for the thermal characterization of samples in the nano-gram range but also, and even more importantly, for its versatility allowing its combination with many other analytical techniques. Such combination can have a big potential for more complete characterization of the materials. Thus, thanks to the development of an accessory for synchrotron nano-focus X-ray diffraction, it has become possible to perform quantitative measurements for different samples such as metals, hybrid materials, polymers, etc. The study reported in this manuscript has been carried out on indium micro-particles. The thermal imaging data collected with the X-rays provides useful information about the sample behaviour. In the near future, such combination of the experimental techniques will hopefully provide more in-depth studies into the structural transformations occuring in the sample.

Another potentially interesting application of nanocalorimetry can consist in generating unstable polymorphs of different materials by rapid quenching the melts. For this task, it becomes fundamental to couple Nanocalorimetry not only with X-ray scattering, but also with Raman spectroscopy, optical microscopy, etc. One example of study in this direction is presented in the manuscript. The study is focused on the structure and thermal behavior of binary nano-sized co-crystals of CL-20 with HMX and TNT prepared using Spray Flash Evaporation (SFE). The combination of in-situ nanocalorimetry with nano-focus X-ray diffraction offers an elegant way to study the structure formation processes occurring in the very first milliseconds after melting.

To conclude, we believe that nanocalorimetry has an important potential not only in becoming one of the interesting tools for the explosive detection

but also in a much larger scope for in-depth studies and development of the novel energetic materials.

Chapter 7

Conclusions finales

Le but de ce travail était d'explorer le potentiel de la nanocalorimétrie dans le domaine de la détection des matières explosives. Il est à noter qu'à l'heure actuelle, le problème de la détection d'explosifs dans les lieux publics est encore non résolu. Les dispositifs de détection existantes ne répondent pas à tous les critères requis pour être considéré comme le dispositif «ultime» de détection qui peut fonctionner à une vitesse satisfaisante et avec une grande sensibilité. Un des aspects de ce problème est lié à la détection de particules solides d'explosifs qui peuvent être à l'état de traces.

Si l'on pense à l'utilisation d'un nanocalorimètre à une telle fin, il est important de proposer le mode de fonctionnement qui sera optimisée en termes de sensibilité et de spécificité. Notre nanocalorimètre fournit deux modes de fonctionnement différents qui peuvent être utilisés à cet effet:

- la calorimétrie DC, où les échantillons sont chauffés de la même manière que l'on procède lors des expériences de la calorimétrie classique, à savoir, à des vitesses de chauffe constantes, mais beaucoup plus rapides.
- les régimes modulés (la calorimétrie dite AC) où les deux composants de la capacité thermique a pression constante, c. a d. les composants réversible et non-réversible, peuvent être mesurées en utilisant l'analyse Fourier du signal en temps réel.

Dans le présent travail, nous avons testé les matériaux énergétiques les plus communs dans les deux modes afin de comprendre si les mesures nanocalorimetriques peuvent, en principe, aider à constituer une bibliothèque des signatures thermiques des matériaux explosifs utilisés dans les attaques terroristes.

Il convient de mentionner que la détection d'explosifs à l'état solide peut être considérée comme étant plus prometteuse comparée à la détection de la vapeur. Cela s'explique par le fait que les pressions des vapeurs d'explosifs les plus couramment utilisés sont relativement faibles à température ambiante. Le présent travail démontre que des mesures quantitatives sont réalisables sur des micro-particules de quelques nano-grammes de ces matériaux. Cela rend la nanocalorimétrie un candidat sérieux pour les fins de détection. Les points de fusion déterminés par nanocalorimétrie sont en accord avec les caractéristiques connues des matériaux lors de l'étude, ce qui montre sans équivoque qu'ils peuvent être utilisés comme une première approche pour établir la bibliothèque des signatures thermiques des explosifs. Enfin, il faut mentionner la capacité de la nanocalorimètre d'effectuer des mesures à haut débit. Par exemple, une rampe de température typique peut être achevée en quelques millisecondes.

Il est évident qu'à l'heure actuelle il reste encore beaucoup de place pour amélioration de la technique. Une des questions en suspens porte sur le positionnement précis de l'échantillon sur des capteurs utilisés afin d'effectuer les mesures et le profil de température à appliquer. Ces aspects doivent être pris en compte car même pour une superficie de 100×100 μm^2, les gradients thermiques au cours des rampes de température rapides peuvent être considérables.

Lors des expériences calorimétriques modulées effectuées sur des microparticules d'explosifs il a été trouvé que les transitions thermiques caractéristiques de ces matériaux ne sont pas observées. En particulier, en fonction de la taille des microparticules, on peut observer par exemple exclusivement les événements thermiques liés à la sublimation de l'échantillon. Dans ce cas, la transition visible comme une marche dans la courbe de la capacité calorifique, ne peut pas constituer la signature thermique de l'explosif, car elle ne serait

pas suffisamment spécifique. En revanche, l'utilisation des chauffes linéaires rapides est beaucoup plus pratique car il permet de séparer les événements thermodynamiques (par exemple, la fusion) et des événements cinétiques (par exemple, la décomposition). Notons que, dans la plupart des cas, les vitesses de chauffage élevées permettent d'observer la fusion de l'échantillon avant qu'il est sublimé complètement. L'observation de la fusion est essentielle car elle peut aider à acquérir la spécificité requise dans l'analyse. Par conséquent, l'utilisation des régimes DC est certainement préférable du point de vue de la détection des explosifs. Cette particularité peut faire de la nanocalorimétrie une technique potentiellement intéressante pour la détection des explosifs.

Récemment, la nanocalorimétrie a révélé son potentiel important non seulement pour la caractérisation thermique des échantillons de quelques nano-grammes, mais aussi, et plus important encore, pour sa flexibilité permettant sa combinaison avec d'autres techniques d'analyse. Une telle combinaison peut avoir un grand potentiel pour la caractérisation plus complète des matériaux. Ainsi, grâce à la mise au point d'un accessoire pour des expériences de diffraction synchrotron des rayons-X en utilisant des nano-faisceaux, il est devenu possible d'effectuer des mesures quantitatives pour des différents échantillons tels que les métaux, les matériaux hybrides, les polymères, etc. L'étude présentée dans ce manuscrit a été effectuée sur les micro-particules de l'indium. Les données d'imagerie thermique recueillies avec des rayons-X fournissent des informations utiles sur le comportement de l'échantillon. Dans un avenir proche, une telle combinaison des techniques expérimentales devrait permettre de mener des études plus approfondies sur les transformations structurales qui se produisent dans l'échantillon.

Une autre application potentiellement intéressante de la nanocalorimétrie consiste à générer des polymorphes instables de différents matériaux par trempe rapide à partir de l'état fondu. Pour cette tâche, il devient essentiel de coupler nanocalorimétrie non seulement avec la diffusion de rayons X, mais également avec la spectroscopie Raman, la microscopie optique, etc. Un exemple d'étude dans cette direction est présenté dans le manuscrit. L'étude se concentre sur la structure et le comportement thermique de taille nanométrique

binaires co-cristaux de CL-20 avec HMX et TNT préparé en utilisant vaporisateur évaporation flash (SFE). La combinaison de la nanocalorimétrie in situ avec des nano-focus diffraction des rayons X offre une manière élégante d'étudier les processus de formation de la structure qui se produisent dans les premières millisecondes après la fusion.

Pour conclure, nous considérons que la nanocalorimétrie a un potentiel important non seulement pour devenir l'un des outils intéressants pour la détection des explosifs, mais aussi dans le contexte de la recherche fondamentale pour le développement des nouveaux matériaux énergétiques.

Appendix A

Thermal gradients on XEN-39392 sensors

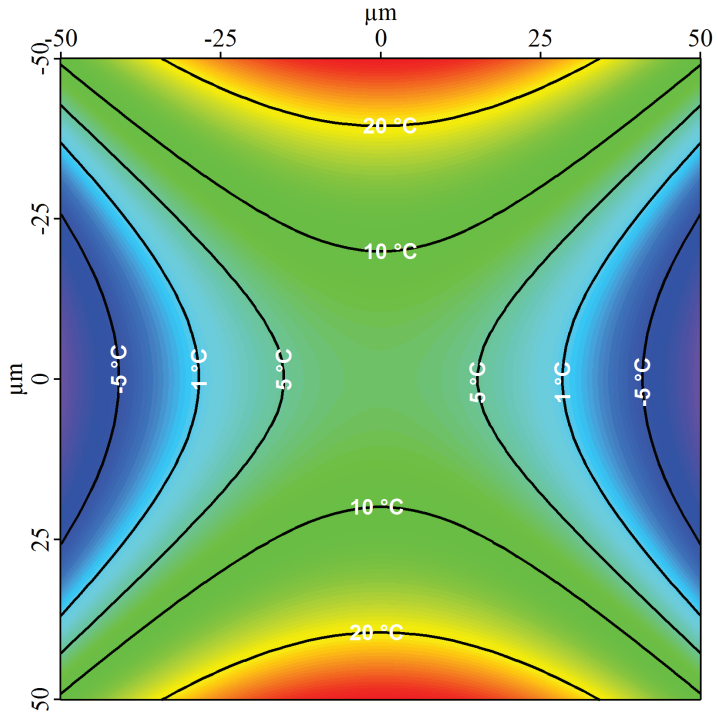

(a) Heating rate of 125 °C s^{-1}

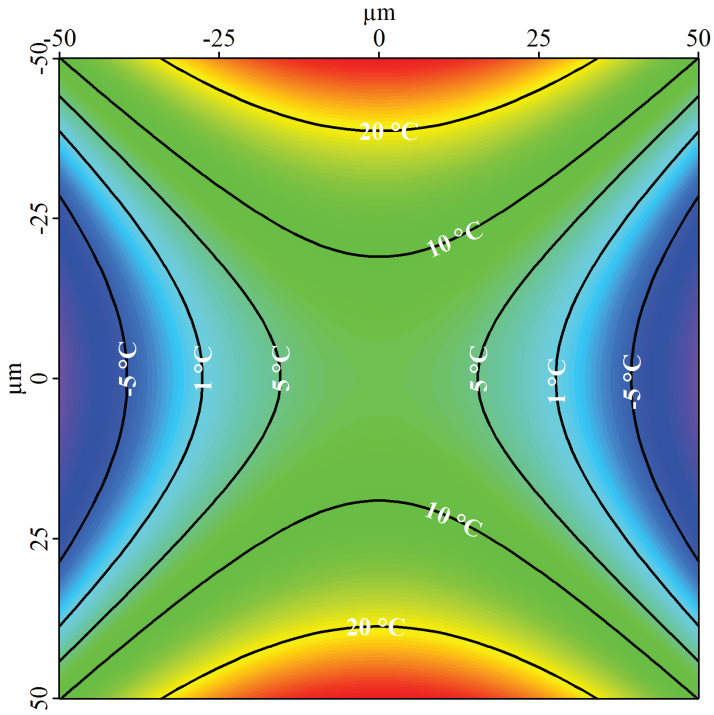

(b) Heating rate of 250 °C s^{-1}

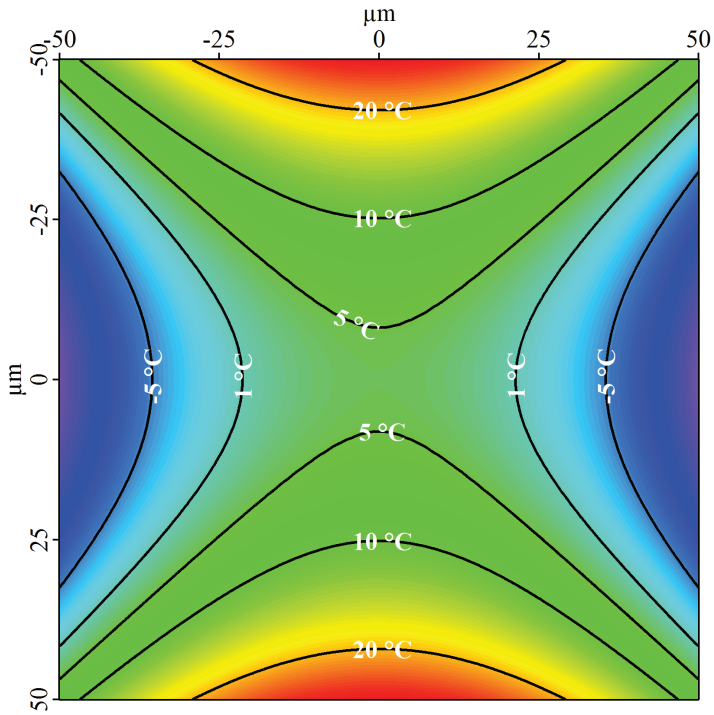

(c) Heating rate of 500 °C s^{-1}

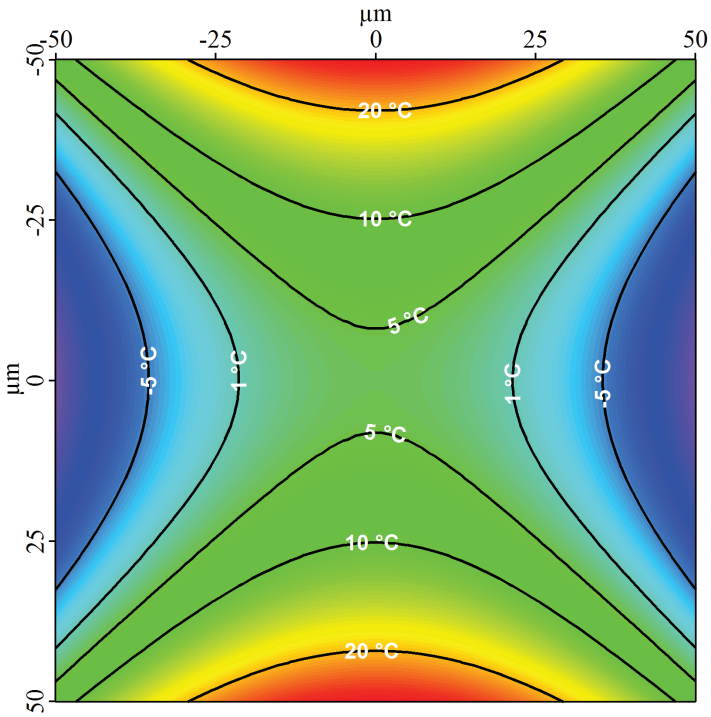

(d) Heating rate of 1000 °C s^{-1}

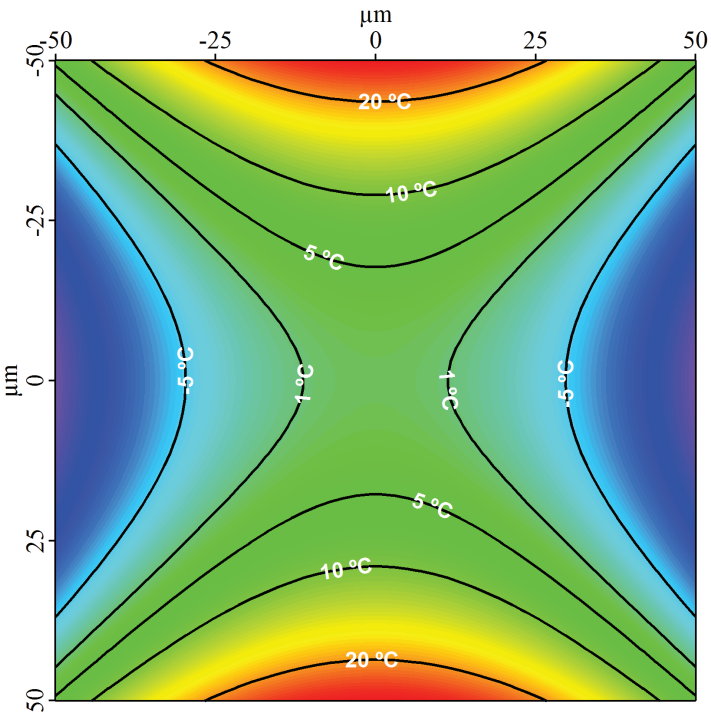

(e) Heating rate of 2000 °C s^{-1}

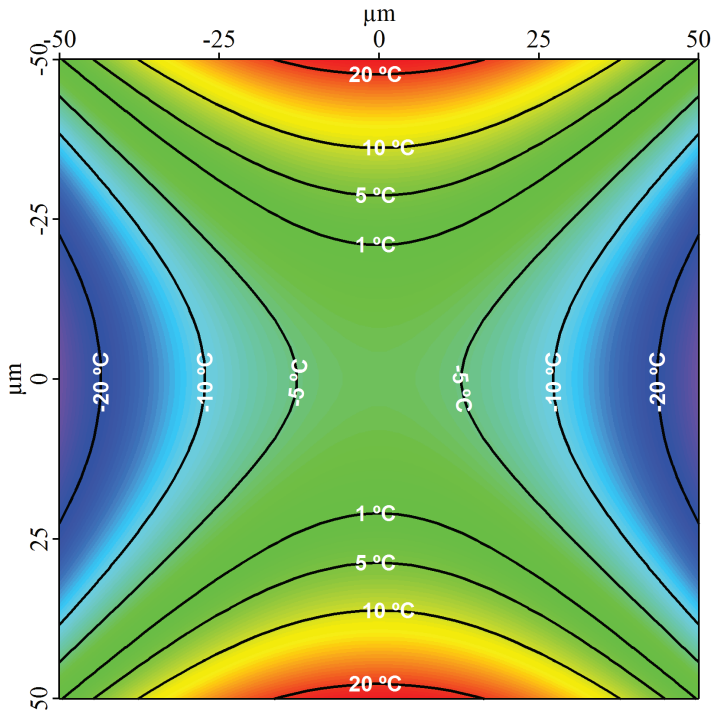

(f) Heating rate of 4000 °C s^{-1}

Figure A.1 – Thermal gradients on sensors XEN-39392